

# Theoretical Modeling and Computational Simulation of Electronic Properties of Nanomaterials

Guest Editors: Shaogang Hao, Zhirong Liu, Junqiang Lu,  
and Gang Zhou





---

# **Theoretical Modeling and Computational Simulation of Electronic Properties of Nanomaterials**

**Theoretical Modeling and Computational  
Simulation of Electronic Properties of  
Nanomaterials**

Guest Editors: Shaogang Hao, Zhirong Liu, Junqiang Lu,  
and Gang Zhou



---

Copyright © 2011 Hindawi Publishing Corporation. All rights reserved.

This is a special issue published in volume 2011 of “Journal of Nanomaterials.” All articles are open access articles distributed under the Creative Commons Attribution License, which permits unrestricted use, distribution, and reproduction in any medium, provided the original work is properly cited.

## Editorial Board

- Katerina Aifantis, Greece  
Nageh K. Allam, USA  
Margarida Amaral, Portugal  
Xuedong Bai, China  
L. Balan, France  
Enrico Bergamaschi, Italy  
Theodorian Borca-Tasciuc, USA  
C. Jeffrey Brinker, USA  
Christian Brosseau, France  
Xuebo Cao, China  
Sang-Hee Cho, Republic of Korea  
Shafiul Chowdhury, USA  
Cui ChunXiang, China  
Miguel A. Correa-Duarte, Spain  
Shadi A. Dayeh, USA  
Ali Eftekhari, USA  
Claude Estournes, France  
Alan Fuchs, USA  
Lian Gao, China  
Russell E. Gorga, USA  
Hongchen Chen Gu, China  
Mustafa O. Guler, Turkey  
John Zhanhu Guo, USA  
Smrati Gupta, Germany  
Michael Harris, USA  
Zhongkui Hong, USA  
Michael Z. Hu, USA  
David Hui, USA  
Y.-K. Jeong, Republic of Korea  
Sheng-Rui Jian, Taiwan  
Wanqin Jin, China  
Rakesh K. Joshi, India  
Zhenhui Kang, China
- Fathallah Karimzadeh, Iran  
Do Kyung Kim, Republic of Korea  
Kin Tak Lau, Australia  
Burtrand Lee, USA  
Benxia Li, China  
Jun Li, Singapore  
Shijun Liao, China  
Gong Ru Lin, Taiwan  
J.-Y. Liu, USA  
Jun Liu, USA  
Tianxi Liu, China  
Songwei Lu, USA  
Daniel Lu, China  
Jue Lu, USA  
Ed Ma, USA  
Gaurav Mago, USA  
Sanjay R. Mathur, Germany  
A. McCormick, USA  
Vikas Mittal, UAE  
Weihai Ni, Germany  
Sherine Obare, USA  
Edward Andrew Payzant, USA  
Kui-Qing Peng, China  
Anukorn Phuruangrat, Thailand  
Ugur Serincan, Turkey  
Huaiyu Shao, Japan  
Donglu Shi, USA  
Suprakas Sinha Ray, South Africa  
Vladimir Sivakov, Germany  
Marinella Striccoli, Italy  
Bohua Sun, South Africa  
Saikat Talapatra, USA  
Nairong Tao, China
- Titipun Thongtem, Thailand  
Somchai Thongtem, Thailand  
Valeri P. Tolstoy, Russia  
Tsung-Yen Tsai, Taiwan  
Takuya Tsuzuki, Australia  
Raquel Verdejo, Spain  
Mat U. Wahit, Malaysia  
Shiren Wang, USA  
Yong Wang, USA  
Cheng Wang, China  
Zhenbo Wang, China  
Jinquan Wei, China  
Ching Ping Wong, USA  
Xingcai Wu, China  
Guodong Xia, Hong Kong  
Zhi Li Xiao, USA  
Ping Xiao, UK  
Shuangxi Xing, China  
Yangchuan Xing, USA  
N. Xu, China  
Doron Yadlovker, Israel  
Ying-Kui Yang, China  
Khaled Youssef, USA  
William W. Yu, USA  
Kui Yu, Canada  
Haibo Zeng, China  
Tianyou Zhai, Japan  
Renyun Zhang, Sweden  
Yanbao Zhao, China  
Lianxi Zheng, Singapore  
Chunyi Zhi, Japan

# Contents

**Theoretical Modeling and Computational Simulation of Electronic Properties of Nanomaterials,**  
Shaogang Hao, Zhirong Liu, Junqiang Lu, and Gang Zhou  
Volume 2011, Article ID 408581, 2 pages

**Synthesis of Ag-Au Nanoparticles by Galvanic Replacement and Their Morphological Studies by HRTEM and Computational Modeling,** Manuel Ramos, Domingo A. Ferrer, Russell R. Chianelli, Victor Correa, Joseph Serrano-Matos, and Sergio Flores  
Volume 2011, Article ID 374096, 5 pages

**Intrinsic Spin-Orbit Coupling in Zigzag and Armchair Graphene Nanoribbons,** Ying Li, Erhu Zhang, Baihua Gong, and Shengli Zhang  
Volume 2011, Article ID 364897, 7 pages

**Pore Structure Control of Ordered Mesoporous Silica Film Using Mixed Surfactants,** Tae-Jung Ha, Hyeon-Gyoon Im, Seok-Jin Yoon, Ho Won Jang, and Hyung-Ho Park  
Volume 2011, Article ID 326472, 5 pages

**Modeling and Simulation of Special Shaped SOI Materials for the Nanodevices Implementation,** Cristian Ravariu and Florin Babarada  
Volume 2011, Article ID 792759, 11 pages

**Poole-Frenkel Conduction in Cu/Nano-SnO<sub>2</sub>/Cu Arrangement,** Hossein Mahmoudi Chenari, Hassan Sedghi, Mohammad Talebian, Mir Maqsoud Golzan, and Ali Hassanzadeh  
Volume 2011, Article ID 190391, 4 pages

**Three Possible Encapsulation Mechanics of TiO<sub>2</sub> Nanoparticles into Single-Walled Carbon Nanotubes,** Wisit Sukchom, Kittisak Chayantrakom, Pairote Satiracoo, and Duangkamon Baowan  
Volume 2011, Article ID 857864, 8 pages

## Editorial

# Theoretical Modeling and Computational Simulation of Electronic Properties of Nanomaterials

Shaogang Hao,<sup>1</sup> Zhirong Liu,<sup>2</sup> Junqiang Lu,<sup>3</sup> and Gang Zhou<sup>4</sup>

<sup>1</sup>The Ames Laboratory of USDOE and Department of Physics, Iowa State University, Ames, IA 50011, USA

<sup>2</sup>College of Chemistry and Molecular Engineering, Peking University, Beijing 100871, China

<sup>3</sup>Department of Physics, University of Puerto Rico, Mayaguez, PR 00681, USA

<sup>4</sup>Department of Physics, Tsinghua University, Beijing 100084, China

Correspondence should be addressed to Shaogang Hao, sghao@ameslab.gov

Received 20 June 2011; Accepted 20 June 2011

Copyright © 2011 Shaogang Hao et al. This is an open access article distributed under the Creative Commons Attribution License, which permits unrestricted use, distribution, and reproduction in any medium, provided the original work is properly cited.

Over the past two decades, the emergence of new techniques has made synthesis and construction of matters at nanoscale possible, leading to an extremely rapid rise of the field of nanomaterials science. For instance, today's electronics industry is the result of advances in nanomaterials research. As electronic devices get smaller, there are increasing challenges in silicon technology. Materials with new scaling properties need to be developed urgently. Indeed, nanomaterials science promises a wide range of novel applications of new perspectives.

Meanwhile, theoretical modeling and computational simulation have advanced as much as the experimental techniques in nanomaterials science. The development ranges from density functional algorithms to mesoscale methods, which enables the pursuit of the characteristic nature of nanomaterials as well as predict and design functional nanomaterials. On the other hand, recent development of parallel processor supercomputers has led to tremendous increase (by a factor of a million) in computational power. These developments together have been creating new opportunities for modeling and simulation of electronic properties of nanomaterials, as well as for designing novel nanoelectronic devices. In this special issue, six papers are selected to provide discovery of novel phenomena, fundamental understanding and prediction, and design of nanomaterials from zero-dimensional nanoparticles, to one-dimensional graphene ribbons and carbon nanotubes, to two-dimensional films.

The first paper of this special issue introduces a novel method to synthesize Ag-Au nanoparticles for the purpose of potential application as catalysis in chemical industries.

Size, shape, and some other basic properties of the resulting bimetallic Ag-Au nanoparticles have been characterized by measurements and computer simulations.

The second paper of this special issue studies the intrinsic spin-orbit coupling effect in the band structures of graphene nanoribbons. Graphene's fascinating properties mostly originate in its simply beautiful electronic structure. Due to the exceedingly small effective mass, graphene holds the promising potential of next generation semiconductor industry. Therefore, enormous attentions are paid to the band structure of graphene. Using tight-binding model and state-of-the-art *ab initio* simulations, it has been discovered that a band gap might be opened at the Dirac point in graphene nanoribbons due to the spin-orbit coupling. Moreover, the ribbon width and edge configuration are found to play an important role in modulating the spin-orbit coupling strength.

The third paper reports the fabrication of silica films with mesoporous. The size of the mesoporous is quite uniform. and the X-ray diffraction shows that the mesoporous pattern in the films is highly ordered. Such interesting structure could be applied as template for further synthesis of quantum devices.

The fourth paper proposes two designs of silicon-on-Insulator (SOI) structures by theoretical modeling. Performances of these SOI structures have been systematically studied in detail. It is interesting that when the film thickness shrinks to nano-/subnano-scale, the electrical behaviors become very distinct compared with classical cases, which could be used to design new SOI-based devices.

The fifth paper reports the synthesis of Cu/SnO<sub>2</sub>-nanoparticle/Cu sandwich structure and studies the electric performance of the products. Armed with theoretical modelings, the authors demonstrated that when the dielectric goes to the size of nanoscale, the conduction behavior is dominated by the Poole-Frenkel mechanism.

The last paper simulates the TiO<sub>2</sub>-nanoparticle encapsulated single-walled carbon nanotube (TiO<sub>2</sub>-NP@SWCNT) by using the Lennard-Jones potentials. Such novel “peapod” nanostructures have been holding a lot of attention in both theoretical and experimental aspects. TiO<sub>2</sub> is a well-known functional material which is widely used in chemical and environmental industries, due to its great catalytic performance. This paper discusses the mechanism of encapsulating TiO<sub>2</sub> nanoparticles into a one-dimensional container, carbon nanotubes. It is shown that TiO<sub>2</sub> particle needs to overcome a strong barrier to enter the nanotube from tube mouth.

*Shaogang Hao  
Zhirong Liu  
Junqiang Lu  
Gang Zhou*

## Research Article

# Synthesis of Ag-Au Nanoparticles by Galvanic Replacement and Their Morphological Studies by HRTEM and Computational Modeling

Manuel Ramos,<sup>1,2</sup> Domingo A. Ferrer,<sup>3</sup> Russell R. Chianelli,<sup>1</sup> Victor Correa,<sup>4</sup> Joseph Serrano-Matos,<sup>4</sup> and Sergio Flores<sup>2</sup>

<sup>1</sup> Materials Research and Technology Institute, UT-El Paso, 500W Univesity Ave., Burges Hall Rm. 303, El Paso, TX 79902, USA

<sup>2</sup> Departamento de Física y Matemáticas, Universidad Autónoma de Ciudad Juárez, Cd. Juárez, Chihuahua C.P. 32300, Mexico

<sup>3</sup> Microelectronics Research Center, University of Texas at Austin, Austin, TX 78758, USA

<sup>4</sup> Departamento de Ciencias y Tecnología, Universidad Metropolitana, San Juan, PR 00928, Puerto Rico

Correspondence should be addressed to Manuel Ramos, maramos1@miners.utep.edu

Received 13 October 2010; Revised 22 November 2010; Accepted 27 December 2010

Academic Editor: Shaogang Hao

Copyright © 2011 Manuel Ramos et al. This is an open access article distributed under the Creative Commons Attribution License, which permits unrestricted use, distribution, and reproduction in any medium, provided the original work is properly cited.

Bimetallic nanoparticles are important because they possess catalytic and electronic properties with potential applications in medicine, electronics, and chemical industries. A galvanic replacement reaction synthesis has been used in this research to form bimetallic nanoparticles. The complete description of the synthesis consists of using the chemical reduction of metallic silver nitrite ( $\text{AgNO}_3$ ) and gold-III chloride hydrate ( $\text{HAuCl}_4$ ) salt precursors. The nanoparticles display round shapes, as revealed by high-resolution transmission electron microscope (HRTEM). In order to better understand the colloidal structure, it was necessary to employ computational models which involved the simulations of HRTEM images.

## 1. Introduction

Synthesis and characterization of nanocrystals have been a research topic of high interest in recent decades due to their potential application in medical (cancer imaging), optical physics, catalysis, engineered materials, and electronics [1–6]. Achievement of specific particle morphology depends solely on right combination of precursors, as well as suitable selection of temperature and capping agents [7].

Presently, one can find several articles where full explanations are included in chemical synthesis techniques to attain specific particle morphologies, along with their potential applications [8]. Monometallic nanoparticles are assumed to have three basic shapes: decahedral, cubo-octahedral, and icosahedral. Nanoparticles geometry and facets are made out of (111) planes as observed in icosahedron; and is attributed to lowest surface energy  $\gamma_{(111)}$  of nucleation in (111)-plane; this implies a large internal core-strain values. Cubo-octahedron presents no internal core-strain and significant large surface energy constituted primarily by (111) and (100)

facets, whereas decahedron has moderate internal strain and smaller facets made of (111) and (100) planes. The following is concluded regarding monometallic nanoparticles:  $\gamma_{(111)} < \gamma_{(100)} < \gamma_{(110)}$  as indicated by Lee and Meisel [9].

Previous theoretical work indicates that the addition of a second metal, when synthesizing nanoparticles, can lead to a significant change on its physical-chemical properties, as reflected also on particle morphology (i.e., core-shell, spherical, and truncated-icosahedral). Very little is known about bimetallic nanoparticles in terms of its crystallographic structure, shape, and location of bimetallic precursors, which can attract attention when studying bimetallic systems.

In order to understand the difference between bimetallic nanoalloy and bulk systems, Yonezawa and Toshima proposed that some bimetallic nanoalloys (i.e., Au-Ag, Au-Pd) seem to exist due to miscibility gaps at certain compositions ratio (i.e., 20%, 30%, and 10%) provoking the formation of a nanoalloy [10]. Nanoalloy formation could be attributed to the differences in atomic radii and electron migration allowing atoms to accommodate, showing shell periodicity

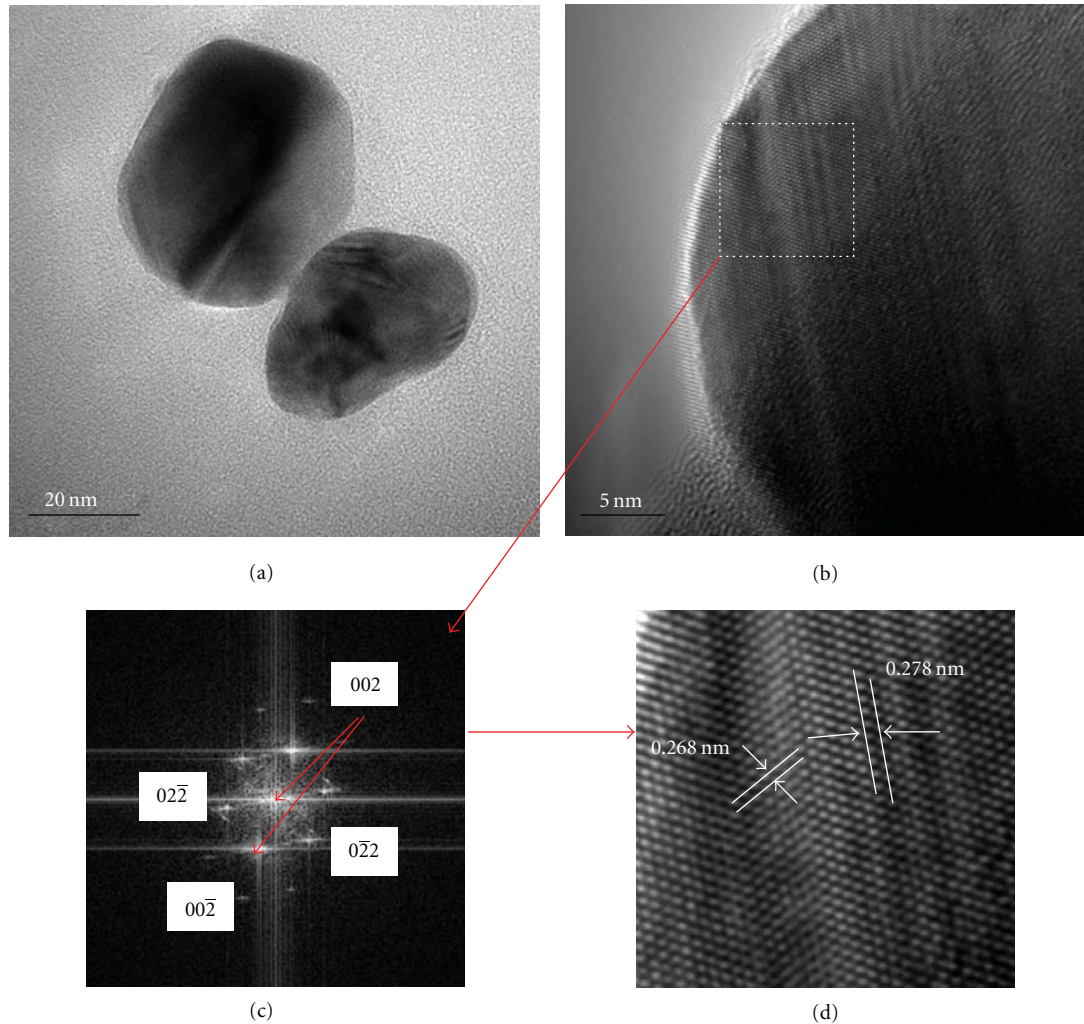


FIGURE 1: (a) 20 nm resolution HRTEM image of spherical shape Ag-Au nanoparticles. (b) 5 nm resolution HRTEM image showing lattice distances. (c) Select area diffraction with  $(02\bar{2})$ ,  $(0\bar{2}2)$ , and  $(00\bar{2})$  principal reflections. (d) Inverse Fast Fourier Transform of SAD presented in (c).

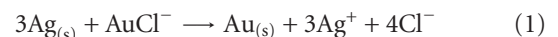
(i.e., onion array layers) as observed by conventional electron microscopy techniques [11].

We present a successful chemical synthesis from Au and Ag salt precursors for bimetallic spherical nanoparticles. Bimetallic particle formation is attributed to a galvanic replacement reaction and shape. Bimetallic composition was confirmed by high resolution transmission electron microscope (HRTEM) results, as well as computational simulations for reconstruction of HRTEM images.

## 2. Experimental

Two precursor solutions were used for chemical synthesis of bimetallic Ag-Au nanoparticles. The first solution was made dissolving 90 mg of silver nitrite ( $\text{AgNO}_3$ ) in 500 mL of distilled water; later a mixture was added. It was made with 1% sodium citrate dissolved in 10 mL of distilled water, which was brought and kept for 1 h to boiling temperature

100°C. Then a separate second solution that consisted of 240 mg of gold-III chloride hydrate ( $\text{HAuCl}_4$ ) dissolved in 500 mL of deionized water at 100°C with the addition of a mixture of 1% sodium citrate and 50 mL of distilled water. Finally, both precursor solutions were mixed together and subjected to vigorous stirring at constant temperature of 100°C for 1 h. The stoichiometric equation for particle formation of Ag-Au galvanic reaction is presented as follows:



and seems to be in agreement with [12].

## 3. Results and Discussion

Particle size, shape, and morphology were studied by HRTEM on an FEI Tecnai TF20 equipped with an STEM unit, high-angle annular dark-field (HAADF) detector, and X-Twin lenses. Sample preparation was done by dissolving

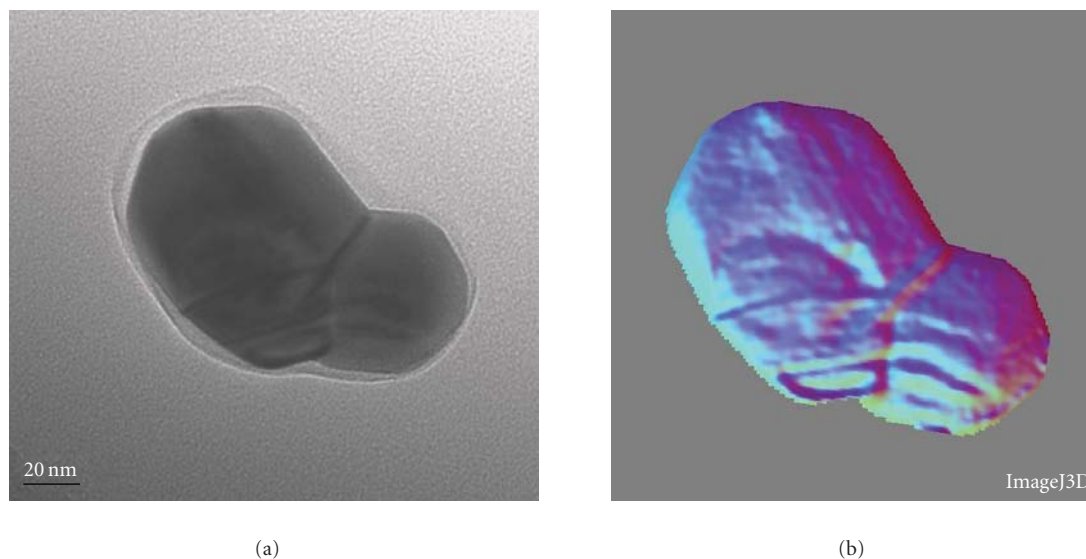


FIGURE 2: (a) HRTEM of elbow-like nanoparticle, formed by accommodation of three small Ag-Au nanoparticles. (b) 3D reconstruction image of (a) performed by ImageJ package.

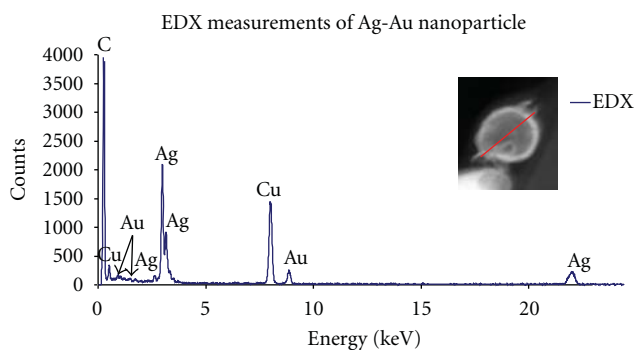


FIGURE 3: EDX results of Ag-Au nanoparticles, Cu and C signals are from TEM grid, inset dark field scanning transmission electron image.

0.5 milligrams in isopropanol placed in an ultrasonic bath for dispersion of nanoparticle clusters. One drop of the solution was used for HRTEM on lacey/carbon (EMS LC225-Cu) grids. Operational voltage was 200 kV in both dark field (DF) and bright field (BF) mode images, with Scherzer defocus condition at  $\Delta f_{\text{Sch}} = -1.2(C_s\lambda)^{1/2}$ . Energy-dispersive X-ray analysis, EDX was performed while TEM using a solid angle of 0.13 sr detector.

Atomic percentage of gold found was about 13% from EDX results, which was confirmed from calculated molar concentration on both precursor solutions; ratios of  $\text{AuCl}_4$  ions with respect to silver were roughly 10%, indicating that for each gold atom there are three silver neighbors present. The percentages were consistent, since lattice parameters in both metals are very similar, for Au-lattice  $\sim 0.4078$  nm and Ag-lattice  $\sim 0.4086$  nm for typical FCC bulk structures. Figure 1(a) presents two round spherical shapes Ag-Au

nanoparticles, Figure 1(b) corresponds to a section of Figure 1(a) at 5 nm of resolution, Figure 1(d) is presenting atomistic distances for [111] and [121] planar directions with atomistic distances of 0.268 nm and 0.278 nm for Au and Ag atoms, respectively; select area of diffraction indicate  $(02\bar{2})$ ,  $(0\bar{2}2)$ , and  $(00\bar{2})$  as principal planar reflections.

Grain boundary was observed for spherical truncated nanoparticles as presented in Figure 2(a). Grain boundary can be understood in terms of surface energy thermodynamics and attributed also to the ionic interaction between specimens as proposed by Elechiguerra et al. for nanorods formation [13]. A 3D reconstruction image is presented in Figure 2(b); the image was reconstructed using ImageJ package. Figure 3 presents EDX results; the two major peak signals correspond to C/Cu content on TEM diffraction grids; gold shows energy intensities at 2 keV and 2.6 keV, whereas for silver, intensities are observed at 3 keV and 3.4 keV. Using A ccelrys Materials Studio, a computational nanoparticle model was done. The model was subjected to TEM simulations using a full dynamical calculation by multislice method [14]. The TEM simulator is based on projected potential  $f(U) = \sum_{i=1}^n a_i e^{-ibU^2}$ , where  $U$  represents coordinates in reciprocal space  $(u, v, w)$ . Results from TEM simulations are presented in Figure 4 and seem to be consistent with experimental HRTEM presented on Figure 2(a).

#### 4. Conclusion

A successful synthesis to produce nanoparticles gold and silver precursor solutions is presented here. Bimetallic Ag-Au nanoparticles were formed due to a galvanic replacement reaction, which consists of the migration of ionic Ag and Au atoms from salt precursors at boiling temperature. Products

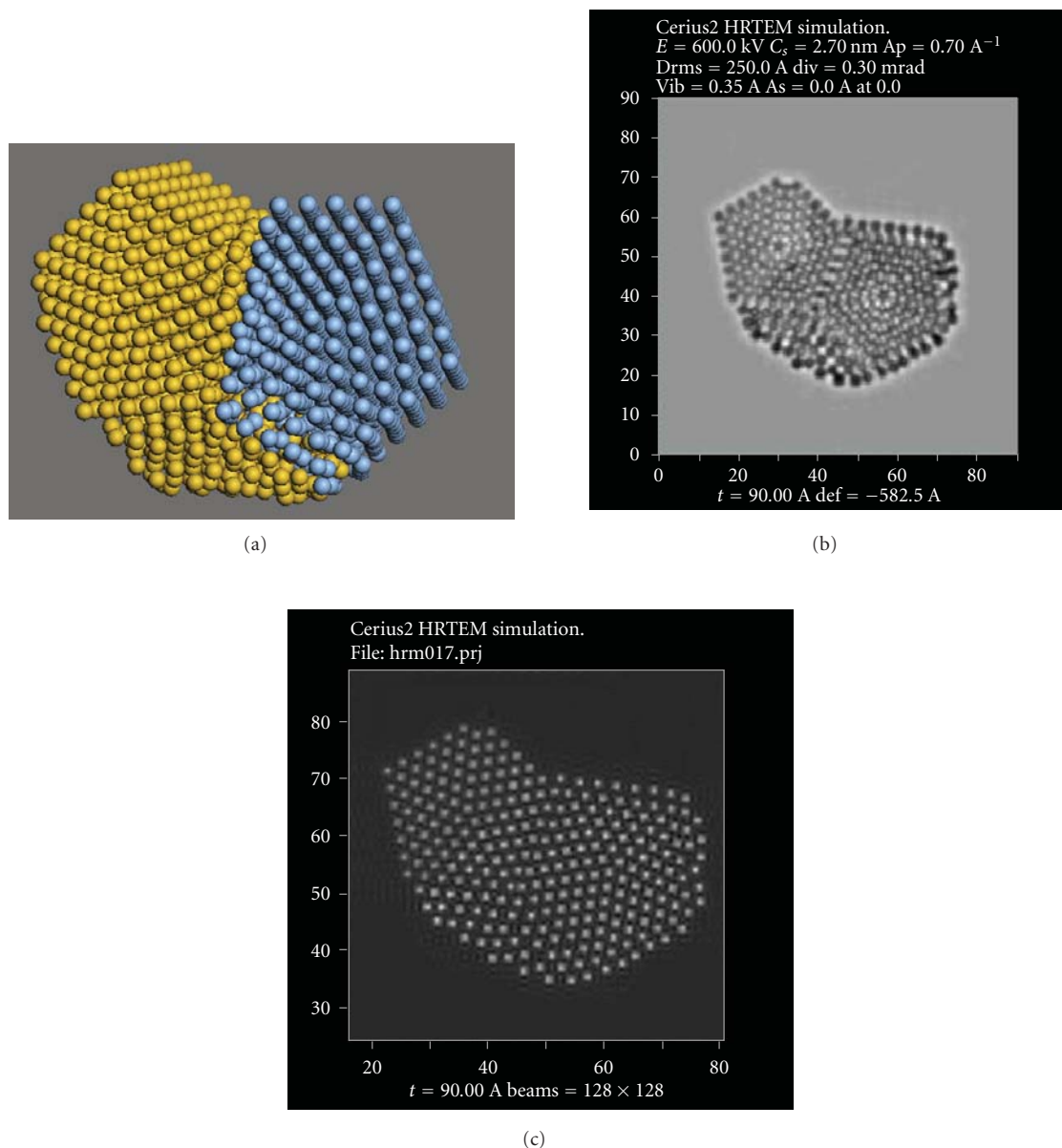


FIGURE 4: (a) Computer assisted Ag-Au nanoparticle (Ag-blue and Au-yellow) used to understand HRTEM image presented in 2. (b) TEM simulation of (a) (Ag-Au nanoparticles) for comparison with experimental HRTEM images.

were analyzed by HRTEM and EDX techniques. EDX results show energy intensity peaks at 2 keV and 2.6 keV for gold and 3 keV and 3.4 keV for silver. Particle shape was studied by computational modeling for specific elbow-like shape for three small Ag-Au nanoparticles. The model was subjected to TEM simulations using full dynamical projected potential. The authors will start testing synthesized Ag-Au nanoparticles as contrasting agents in cancer mapping for biotissue during magnetic resonance imaging (MRI) studies [15].

### Acknowledgments

The authors thank the Consejo Nacional de Ciencia y Tecnología, México for their economic support, the National

Nanotechnology Infrastructure Network (NNIN) Research Program of the Microelectronic Research Center of UT-Austin, and the Materials Research and Technology Institute of UT-El Paso for usage of research facilities.

### References

- [1] N. Toshima and T. Yonezawa, "Preparation of polymer-protected gold/platinum bimetallic clusters and their application to visible light-induced hydrogen evolution," *Makromolekulare Chemie, Macromolecular Symposia*, vol. 59, pp. 281–295, 1992.
- [2] D. Garcia-Gutierrez, C. Gutierrez-Wing, M. Miki-Yoshida, and M. Jose-Yacamán, "HAADF study of Au-Pt core-shell

- bimetallic nanoparticles,” *Applied Physics A*, vol. 79, no. 3, pp. 481–487, 2004.
- [3] J. Chen, B. Wiley, Z. Y. Li et al., “Gold nanocages: engineering their structure for biomedical applications,” *Advanced Materials*, vol. 17, no. 18, pp. 2255–2261, 2005.
- [4] G. A. Hussein and W. G. Pitt, “Micelles and nanoparticles for ultrasonic drug and gene delivery,” *Advanced Drug Delivery Reviews*, vol. 60, no. 10, pp. 1137–1152, 2008.
- [5] T. Paulmier, J. M. Bell, and P. M. Fredericks, “Plasma electrolytic deposition of titanium dioxide nanorods and nano-particles,” *Journal of Materials Processing Technology*, vol. 208, no. 1-3, pp. 117–123, 2008.
- [6] V. Vashchenko, A. Krivoshey, I. Knyazeva, A. Petrenko, and J. W. Goodby, “Palladium-catalyzed Suzuki cross-coupling reactions in a microemulsion,” *Tetrahedron Letters*, vol. 49, no. 9, pp. 1445–1449, 2008.
- [7] L. Rivas, S. Sanchez-Cortes, J. V. García-Ramos, and G. Morcillo, “Mixed silver/gold colloids: a study of their formation, morphology, and surface-enhanced Raman activity,” *Langmuir*, vol. 16, no. 25, pp. 9722–9728, 2000.
- [8] N. N. Kariuki, J. Luo, M. M. Maye et al., “Composition-controlled synthesis of bimetallic gold-silver nanoparticles,” *Langmuir*, vol. 20, no. 25, pp. 11240–11246, 2004.
- [9] P. C. Lee and D. Meisel, “Adsorption and surface-enhanced Raman of dyes on silver and gold sols,” *Journal of Physical Chemistry*, vol. 86, no. 17, pp. 3391–3395, 1982.
- [10] T. Yonezawa and N. Toshima, “Polymer- and micelle-protected gold/platinum bimetallic systems. Preparation, application to catalysis for visible-light-induced hydrogen evolution, and analysis of formation process with optical methods,” *Journal of Molecular Catalysis*, vol. 83, no. 1-2, pp. 167–181, 1993.
- [11] J. M. Montejano-Carrizales, J. L. Rodriguez-Lopez, C. Gutierrez-Wing, M. Miki-Yoshida, and M. Jose-Yacaman, “Crystallography and shape of nanoparticles and clusters: geometrical analysis, image, diffraction simulation and high resolution images,” in *Encyclopedia of Nanoscience and Nanotechnology*, H. S. Nalwa, Ed., vol. 2, pp. 237–282, American Scientific Publishers, Los Angeles, Calif, USA, 2004.
- [12] J. Chen, B. Wiley, Z. Y. Li et al., “Gold nanocages: engineering their structure for biomedical applications,” *Advanced Materials*, vol. 17, no. 18, pp. 2255–2261, 2005.
- [13] J. L. Elechiguerra, J. Reyes-Gasga, and M. J. Yacamán, “The role of twinning in shape evolution of anisotropic noble metal nanostructures,” *Journal of Materials Chemistry*, vol. 16, no. 40, pp. 3906–3919, 2006.
- [14] A. Gómez-Rodríguez, L. M. Beltrán-del-Río, and R. Herrera-Becerra, “SimulaTEM: multislice simulations for general objects,” *Ultramicroscopy*, vol. 110, no. 2, pp. 95–104, 2010.
- [15] P. K. Jain, I. H. ElSayed, and M. A. El-Sayed, “Au nanoparticles target cancer,” *Nano Today*, vol. 2, no. 1, pp. 18–29, 2007.

## Research Article

# Intrinsic Spin-Orbit Coupling in Zigzag and Armchair Graphene Nanoribbons

Ying Li,<sup>1</sup> Erhu Zhang,<sup>1</sup> Baihua Gong,<sup>1</sup> and Shengli Zhang<sup>1,2</sup>

<sup>1</sup>Department of Applied Physics, Xi'an Jiaotong University, Xi'an 710049, China

<sup>2</sup>MOE Key Laboratory for Nonequilibrium Synthesis and Modulation of Condensed Matter, Xi'an Jiaotong University, Xi'an 710049, China

Correspondence should be addressed to Shengli Zhang, zhangsl@mail.xjtu.edu.cn

Received 26 December 2010; Accepted 23 February 2011

Academic Editor: Shaogang Hao

Copyright © 2011 Ying Li et al. This is an open access article distributed under the Creative Commons Attribution License, which permits unrestricted use, distribution, and reproduction in any medium, provided the original work is properly cited.

Starting from a tight-binding model, we derive the energy gaps induced by intrinsic spin-orbit (ISO) coupling in the low-energy band structures of graphene nanoribbons. The armchair graphene nanoribbons may be either semiconducting or metallic, depending on their widths in the absence of ISO interactions. For the metallic ones, the gaps induced by ISO coupling decrease with increasing ribbon widths. For the ISO interactions, we find that zigzag graphene nanoribbons with odd chains still have no band gaps while those with even chains have gaps with a monotonic decreasing dependence on the widths. First-principles calculations have also been carried out, verifying the results of the tight-binding approximation. Our paper reveals that the ISO interaction of graphene nanoribbons is governed by their geometrical parameters.

## 1. Introduction

Graphene, first obtained in 2004 [1], has been explored for spintronics due to its unique and intriguing properties [2]. In spintronics, one of the main interactions that could affect the spin behavior is intrinsic spin-orbit (ISO) coupling. In the last few years, a volume of research has been performed on the ISO coupling in graphene [3–8] and shows that the ISO coupling can cause a gap in the band structure. Recently, it is reported that the geometric curvature [5, 9, 10] and impurity [11] can enhance the effective strength of the ISO by orders of magnitude.

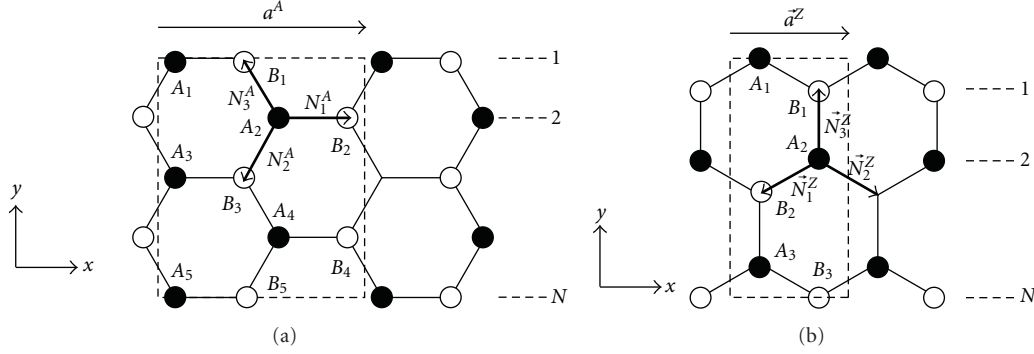
When graphene is patterned into a narrow ribbon, one obtains a graphene nanoribbon (GNR), whose carriers are confined to the one-dimensional (1D) system. There are two basic shapes of GNRs, called armchair GNRs (AGNRs) and zigzag GNRs (ZGNRs). Both results by tight-binding (TB) method [12–15] and first-principles calculations [16–19] show that spectra of GNRs depend strongly on the shapes of their edges. GNRs, offering a system to investigate confinement effects, could be key elements in future electronics and spin-transport applications. In the case of GNRs with ISO coupling, on one hand, based on TB model, Zarea et al.

[20–22] have studied the effects of ISO interactions on low-energy properties of AGNRs and ZGNRs. However, these works were based on the effective  $\pi$ -orbital TB approaches and used the model from graphene plane by imposing hard-wall boundary conditions. They did not study ISO from that of each atom. They also did not give the exact data of the gap induced by ISO coupling. On the other hand, based on first principles, few investigations of the ISO interaction on GNRs have so far been performed. Thus, the ISO coupling is still significant and challenging in GNR.

In this paper, we study the ISO effects on ZGNRs and AGNRs by the  $sp^3$  TB method from a graphene ribbon model. The first-principles calculations are also performed to verify the results. Our investigation reveals how the geometrical parameters, such as width and the edge shape, affect the strength of the ISO.

## 2. Tight-Binding Model

Two basic kinds of GNRs are shown in Figure 1. The AGNRs are classified by number of dimer lines while ZGNRs by number of chains. To simplify, we use  $N$ -AGNR and  $N$ -ZGNR to represent the AGNR with  $N$  dimer lines and

FIGURE 1: The geometry of (a)  $N$ -AGNR and (b)  $N$ -ZGNR.

the ZGNR with  $N$  chains, respectively. As seen in Figure 1, a GNR is described by a rectangular unit cell containing  $2N$  carbon atoms. The  $2N$  atoms can be classified to  $N$  subsystems. Each subsystem contains two atoms  $A$  and  $B$ . The unit vector  $\vec{a}^A$  ( $\vec{a}^Z$ ) denotes the translational axis of an (a) AGNR (ZGNR). The nearest-neighbor translation vectors of the atoms are

$$\begin{aligned}\vec{N}^A &= \{\vec{N}_1^A, \vec{N}_2^A, \vec{N}_3^A\} \\ &= \left\{ a \left( \frac{1}{\sqrt{3}}, 0 \right), a \left( -\frac{1}{2\sqrt{3}}, -\frac{1}{2} \right), a \left( -\frac{1}{2\sqrt{3}}, \frac{1}{2} \right) \right\}, \\ \vec{N}^Z &= \{\vec{N}_1^Z, \vec{N}_2^Z, \vec{N}_3^Z\} \\ &= \left\{ a \left( -\frac{1}{2}, -\frac{1}{2\sqrt{3}} \right), a \left( \frac{1}{2}, -\frac{1}{2\sqrt{3}} \right), a \left( 0, \frac{1}{\sqrt{3}} \right) \right\},\end{aligned}\quad (1)$$

where  $a = 2.46 \text{ \AA}$ . We employ the tight-binding method within a two-center Slater-Koster approximation for nearest-neighbor hopping, and orthogonality between Wannier functions centered on different atoms is assumed. This gives the elements of the Hamiltonian matrix [4]

$$\begin{aligned}h_{A,\mu;A,\mu'}(\vec{k}) &= h_{B,\mu;B,\mu'}(\vec{k}) = t_\mu \delta_{\mu,\mu'}, \\ h_{A,\mu;B,\mu'}(\vec{k}) &= h_{B,\mu';A,\mu}^*(\vec{k}) = \sum_{i=\text{nearest}} e^{i\vec{k}\cdot\vec{N}_i} t_{\mu,\mu'}(\vec{N}_i),\end{aligned}\quad (2)$$

where  $\mu$  ( $\mu'$ ) =  $s, p_x, p_y, p_z$ ,  $A$  and  $B$  represent the two distinct sites in the honeycomb lattice unit cell.  $t_\mu$  is the atomic energies of  $\mu$  orbital, and  $t_{\mu,\mu'}$  denotes the hopping energies between the nearest-neighbor sites. In Table 1, we reproduce for completeness the relationship between  $t_{\mu,\mu'}$  and the four independent Slater-Koster parameters. To simplify, we let  $\theta = (ss\sigma)$ ,  $\alpha = (sp\sigma)$ ,  $\beta = (pp\sigma)$ , and  $\eta = (pp\pi)$ . The wave vector  $k$  is parallel to  $x$ .

First, we consider the  $\pi$  electrons. The  $2 \times 2$  hamiltonian matrix  $H_{\pi mn}$  is introduced to describe the interaction of

TABLE 1: Two-center matrix elements for hopping between  $s$  and  $p$  orbital along a direction specified by the unit vector  $(n_x, n_y, n_z)$ , taken from [4].  $s = -8.868 \text{ eV}$ ,  $p = 0$ ,  $(ss\sigma) = -6.769 \text{ eV}$ ,  $(sp\sigma) = 5.580 \text{ eV}$ ,  $(pp\sigma) = 5.037 \text{ eV}$ , and  $(pp\pi) = -3.033 \text{ eV}$ .

$t_s$	$s$	$t_{p_x,p_x}$	$n_x^2(pp\sigma) + (1 - n_x^2)(pp\pi)$
$t_p$	$p$	$t_{p_y,p_y}$	$n_y^2(pp\sigma) + (1 - n_y^2)(pp\pi)$
$t_{s,s}$	$(ss\sigma)$	$t_{p_z,p_z}$	$n_z^2(pp\sigma) + (1 - n_z^2)(pp\pi)$
$t_{s,p_x}$	$n_x(sp\sigma)$	$t_{p_x,p_y}$	$n_x n_y (pp\sigma) - n_x n_y (pp\pi)$
$t_{s,p_y}$	$n_y(sp\sigma)$	$t_{p_x,p_z}$	$n_x n_z (pp\sigma) - n_x n_z (pp\pi)$
$t_{s,p_z}$	$n_z(sp\sigma)$	$t_{p_y,p_z}$	$n_y n_z (pp\sigma) - n_y n_z (pp\pi)$

$m$  and  $n$  subsystems. The  $2N \times 2N$  hamiltonian matrix for  $N$ -GNR can be written as follows:

$$H_\pi = \begin{pmatrix} H_{\pi 1,1} & H_{\pi 1,2} & 0 & \cdots & 0 & 0 & 0 \\ H_{\pi 2,1} & H_{\pi 2,2} & H_{\pi 2,3} & \cdots & 0 & 0 & 0 \\ \vdots & \vdots & \vdots & & \vdots & \vdots & \vdots \\ 0 & 0 & 0 & \cdots & H_{\mathcal{A},N-2} & H_{\mathcal{A},N-1} & H_{\mathcal{A},N} \\ 0 & 0 & 0 & \cdots & 0 & H_{\pi N,N-1} & H_{\pi N,N} \end{pmatrix}, \quad (3)$$

where  $\mathcal{A}$  denotes  $\pi N - 1$ .

We can diagonalize the above hamiltonian and gain the eigenvalues for GNRs. The results are the same with those of [12]. The energy spectra of AGNRs for different widths can be observed in Figure 2. The system is metallic for AGNRs with widths  $N = 3M - 1$ , where  $M$  is an integer, and insulating otherwise. For the metallic AGNRs, the top of valence band and the bottom of conduction band are degenerate at  $K^A = 0$  in the Brillouin zone (BZ). For the insulating ones, the gaps decrease with an increase in ribbon widths and tend to zero in very large  $N$ . The calculated band structures of ZGNRs are depicted in Figure 3 for four different ribbon widths. It is observed that for ZGNRs, the valence band and the conduction band are degenerate at  $K^Z = \pi/a$  and  $K^{Z'} = -\pi/a$  in the BZ.

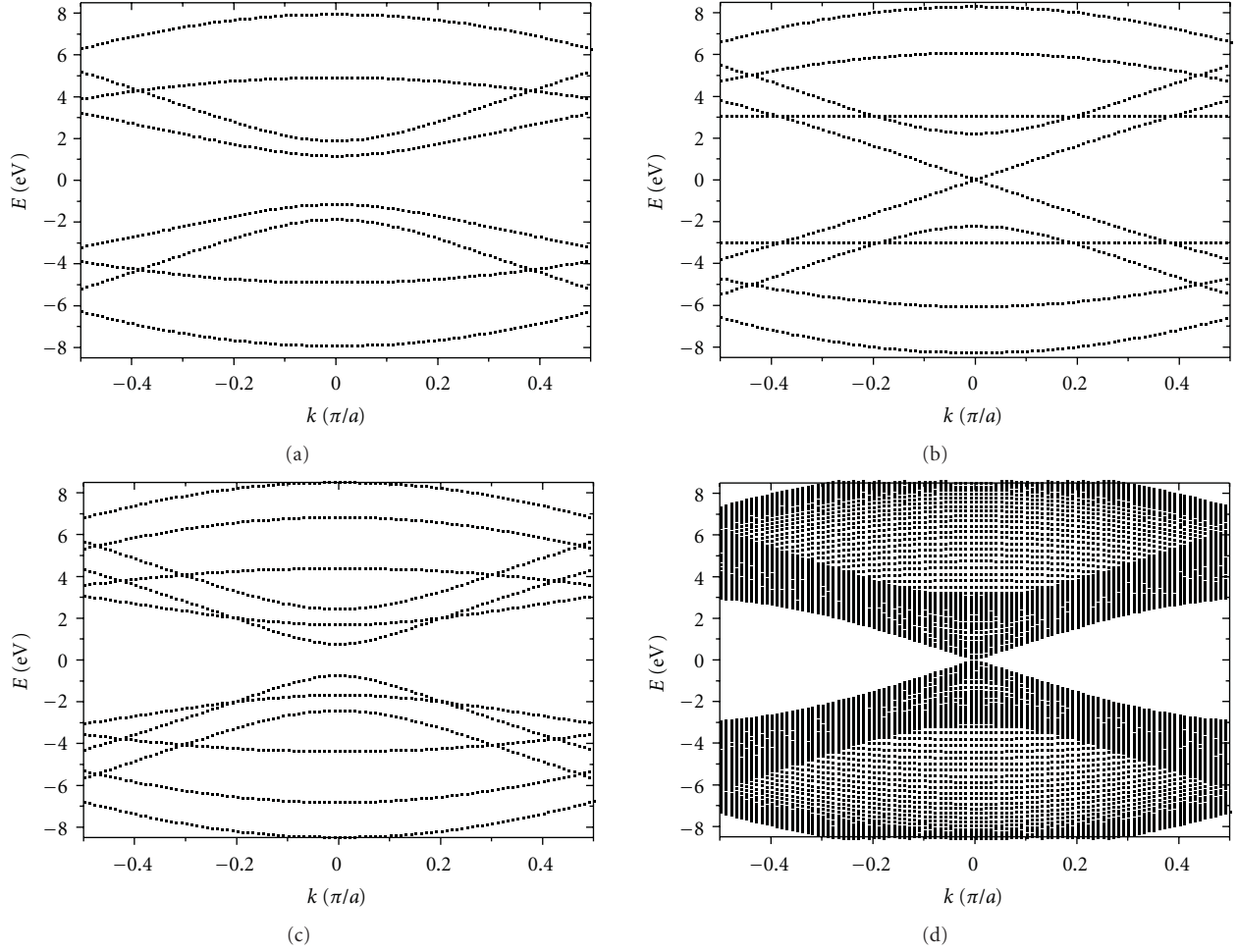


FIGURE 2: Calculated band structures of AGNRs with (a)  $N = 4$ , (b)  $N = 5$ , (c)  $N = 6$ , and (d)  $N = 60$ .

### 3. Intrinsic Spin-Orbit Coupling

$H_{SO}$  induces  $\sigma$ - $\pi$  coupling. So, we discuss the hamiltonian including both  $\pi$  and  $\sigma$  electrons. The hamiltonian for  $N$ -GNR is an  $8N \times 8N$  matrix:

$$\begin{aligned}
 & H_{\pi\sigma} \\
 & = \begin{pmatrix} H_{1,1} & H_{1,2} & 0 & \cdots & 0 & 0 & 0 \\ H_{2,1} & H_{2,2} & H_{2,3} & \cdots & 0 & 0 & 0 \\ \vdots & \vdots & \vdots & & \vdots & \vdots & \vdots \\ 0 & 0 & 0 & \cdots & H_{N-1,N-2} & H_{N-1,N-1} & H_{N-1,N} \\ 0 & 0 & 0 & \cdots & 0 & H_{N,N-1} & H_{N,N} \end{pmatrix}. \quad (4)
 \end{aligned}$$

We consider the ISO interaction as an additional term to  $H_{\pi\sigma}$ . The ISO interaction  $H_{SO}$  of the system comes from each atomic ISO hamiltonian  $h_{SO}$ .  $h_{SO}$  is in the form of  $h_{SO} = \xi \vec{L} \cdot \vec{S}$ , where  $\xi = 6$  meV denotes the ISO coupling constant.  $\vec{L}$  and  $\vec{S}$  represent the angular momentum operator and the spin

operator, respectively. The hamiltonian  $h_{SO}$  can be expressed as follows [3–5]:

$$h_{SO} = \begin{pmatrix} 0 & 0 & 0 & 0 & 0 & 0 & 0 & 0 \\ 0 & 0 & \frac{i\xi}{2} & 0 & 0 & 0 & 0 & \frac{\xi}{2} \\ 0 & -\frac{i\xi}{2} & 0 & 0 & 0 & 0 & 0 & \frac{i\xi}{2} \\ 0 & 0 & 0 & 0 & 0 & \frac{\xi}{2} & \frac{i\xi}{2} & 0 \\ 0 & 0 & 0 & 0 & 0 & 0 & 0 & 0 \\ 0 & 0 & 0 & \frac{\xi}{2} & 0 & 0 & -\frac{i\xi}{2} & 0 \\ 0 & 0 & 0 & -\frac{i\xi}{2} & 0 & \frac{i\xi}{2} & 0 & 0 \\ 0 & \frac{\xi}{2} & -\frac{i\xi}{2} & 0 & 0 & 0 & 0 & 0 \end{pmatrix}, \quad (5)$$

which acts on the basis states  $|s \uparrow\rangle$ ,  $|p_x \uparrow\rangle$ ,  $|p_y \uparrow\rangle$ ,  $|p_z \uparrow\rangle$ ,  $|s \downarrow\rangle$ ,  $|p_x \downarrow\rangle$ ,  $|p_y \downarrow\rangle$ , and  $|p_z \downarrow\rangle$ . Then, the total hamiltonian including ISO interaction is  $H = H_{\pi\sigma} + H_{SO}$ . Finally, we solve the total hamiltonian for GNRs and obtain the eigenvalues.

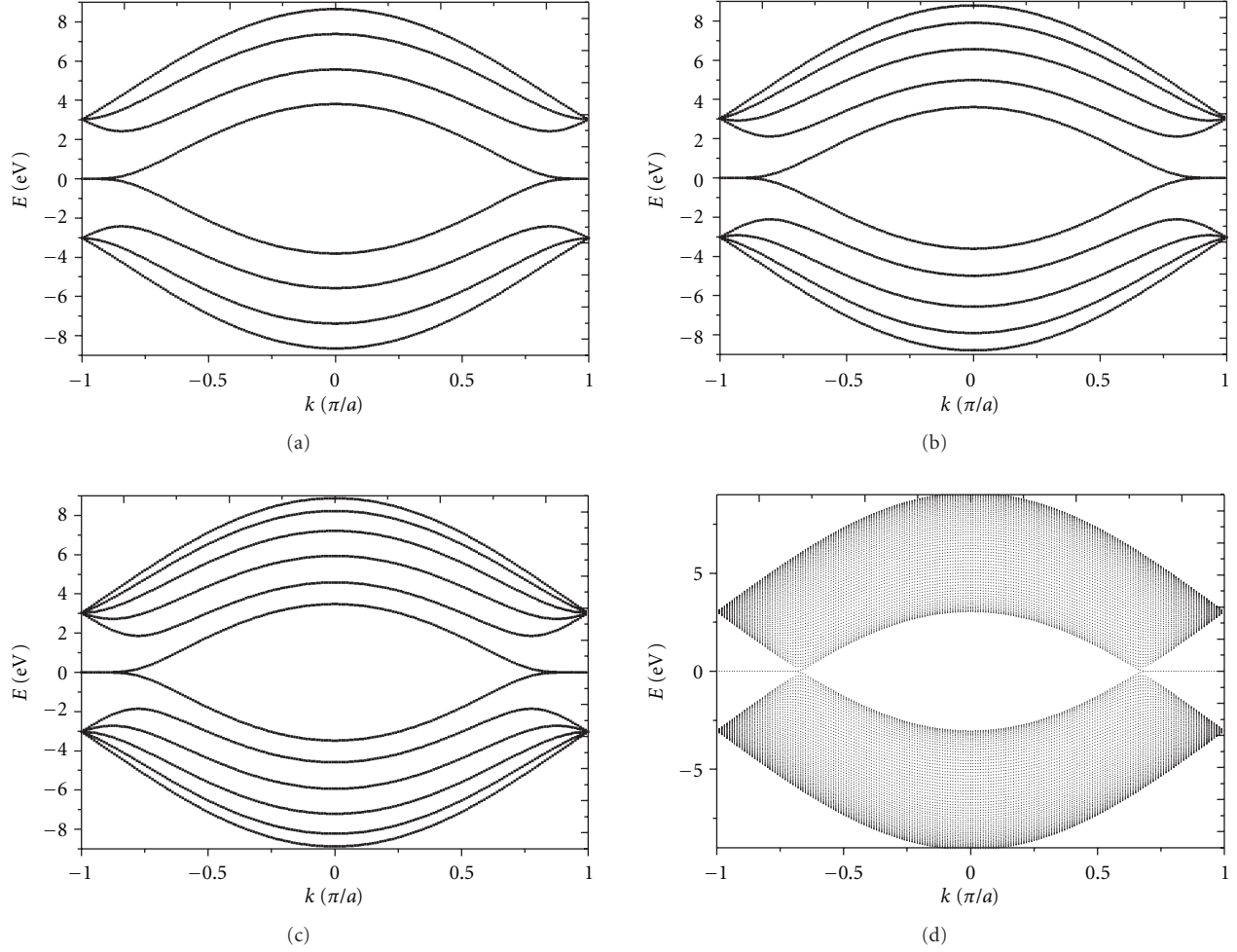


FIGURE 3: Calculated band structures of ZGNRs with (a)  $N = 4$ , (b)  $N = 5$ , (c)  $N = 6$ , and (d)  $N = 60$ .

Since it has been shown that the ISO coupling in graphene just causes a small gap [3–8], thus the spectra near the Fermi surface attract our interest. Hence, we focus on the metallic GNRs. If ISO interaction is taken into account, the band structures are lifted. In metallic AGNRs and the ZGNRs with even chains, a gap is opened in the spectra by ISO coupling. In contrast, for the ZGNRs with odd chains, conduction and valence edge bands are still degenerated at  $K^Z = \pi/a$ . The difference between the influence on odd ZGNRs and even ZGNRs is likely due to their configuration. The odd ZGNRs are in “zigzag/antizigzag” configuration while even ZGNRs are in “zigzag/zigzag” configuration. We display the energy spectrum near Fermi surface of 5-AGNR with ISO interaction near  $K^A$  point in Figure 4(a). The band gap caused at  $k = 0$  is  $1.7 \times 10^{-3}$  meV. The band structures of 5-ZGNR and 4-ZGNR with ISO interaction near  $K^Z$  point are presented in Figures 4(b) and 4(c). For 4-ZGNR, the highest valence band state and the lowest conduction band state are located at  $k = 0.9973 \pi/a$  rather than  $k = \pi/a$  point. There is a band gap of  $1 \times 10^{-5}$  meV induced by ISO. The ISO interaction is shown to have a stronger effect in 5-AGNR than in 4-ZGNR. It is possible because that the proportion of edge

atoms in unit cell atoms which is  $4/10$  for 5-AGNR is larger than  $2/8$  for 4-ZGNR. The relation between the gaps and the widths will be discussed in the next section to compare the results with the first-principles calculations data.

#### 4. First-Principles Calculations

In order to verify the results from TB model, we study the metallic GNRs by first-principles calculations. The relativistic *ab initio* electronic structure calculations for graphene nanoribbons have been performed using the Vienna *ab initio* simulation package (VASP) [23]. We choose the projector augmented wave (PAW) method [24] with a Perdew-Burke-Ernzerhof (PBE) generalized gradient exchange correlation potential (GGA) to describe the electron interactions [25]. A vacuum separation of  $10 \text{ \AA}$  is used to eliminate interactions between graphene layers. An energy cutoff of 950 eV and Monkhorst-Pack k-point meshes are employed to deal with the many atoms in a unit cell of the GNRs for various widths. The ISO interaction is calculated considering only the spherical part of the potential inside muffin tins surrounding the carbon nuclei. The edge carbon atoms of our GNRs are

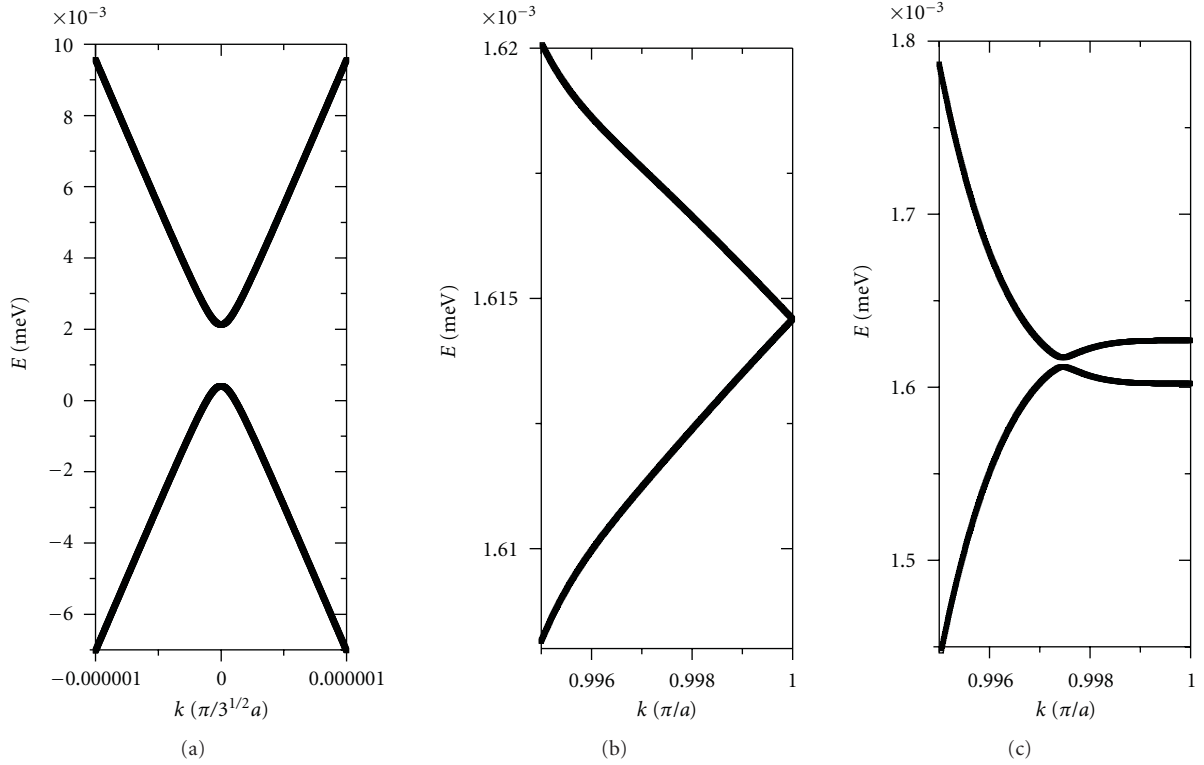


FIGURE 4: The band structures of the GNRs with ISO interaction for (a) 5-AGNR, (b) 5-ZGNR, and (c) 4-ZGNR. The band gaps are  $1.7 \times 10^{-3}$  meV, 0, and  $1 \times 10^{-5}$  meV, respectively.

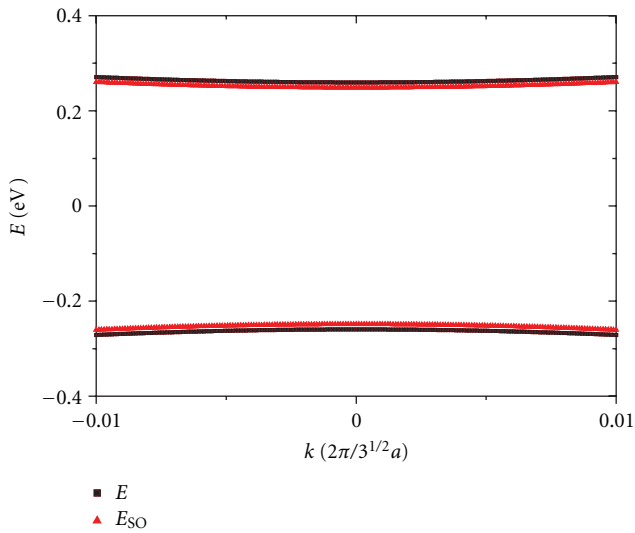


FIGURE 5: (Color online) Band structure of the 5-AGNR without (black squares) and with (red triangles) ISO coupling obtained by first-principles calculations.

passivated by hydrogen atoms. Due to the smallness of ISO-derived gaps in GNRs, we artificially increase the relativistic potential in VASP code in our calculations.

First, we study the band structures of AGNRs with different widths  $N = 3M-1$  in the range of  $N = 5$  to  $N = 35$ .

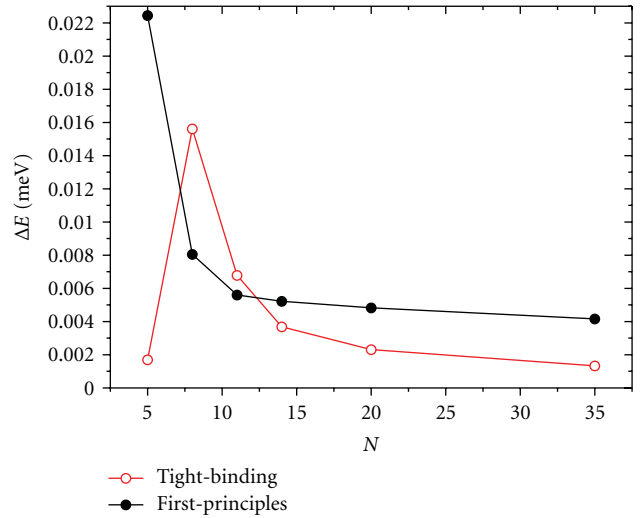


FIGURE 6: (Color online) The relationship between the gaps induced by ISO and N-AGNRs from tight-binding approximation (red circles) and from First-principles calculations (black diamonds; energies are multiplied by 50).

We have known that the AGNRs with  $N = 3M-1$  show the metallic behaviors in TB method without ISO interactions, and gaps are opened by the ISO coupling between the valence band and the conduction band. While for the first principles calculations, we find that there are always gaps in the band

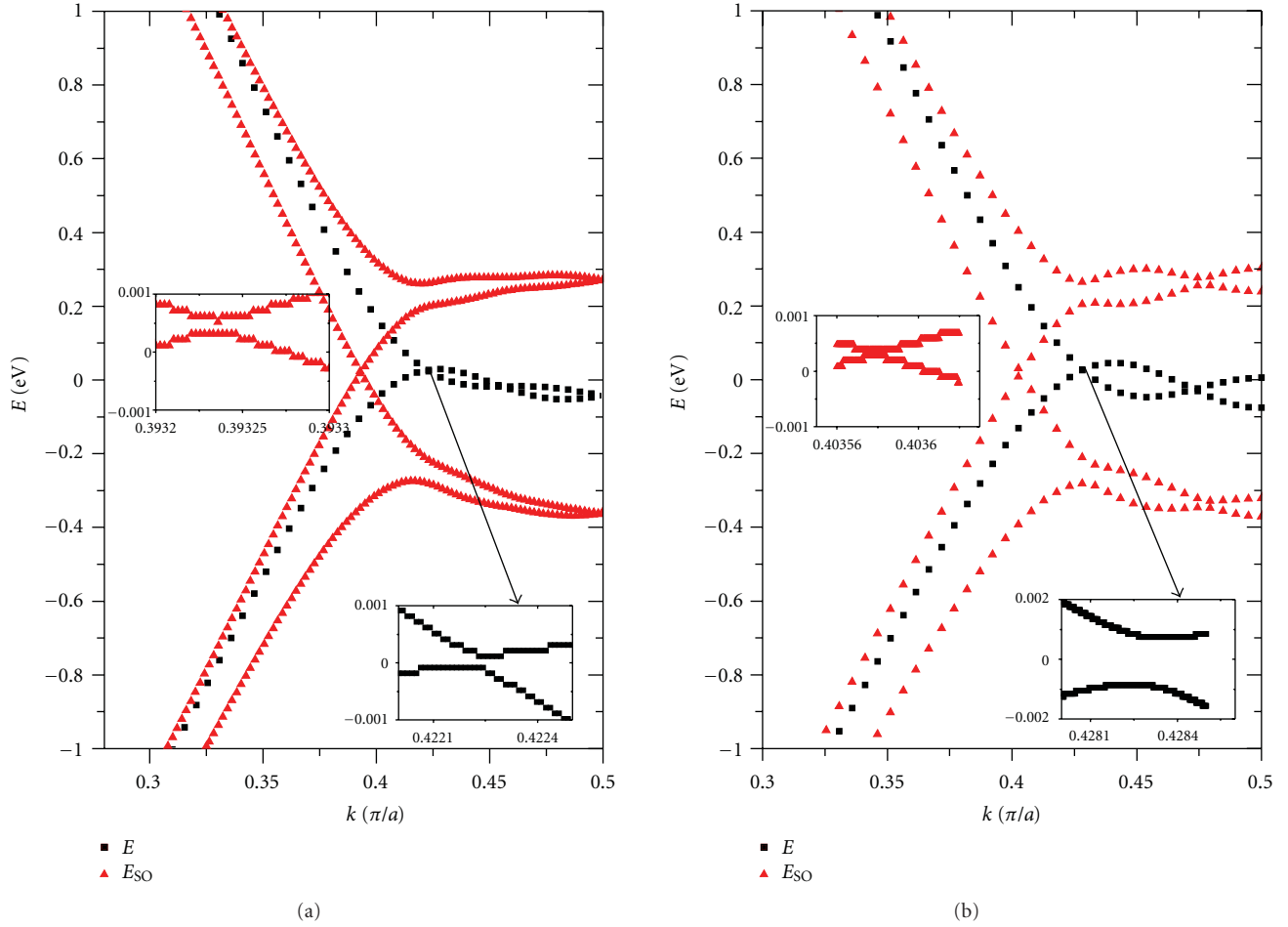


FIGURE 7: (Color online) Band structures of the (a) 5-ZGNR and (b) 4-ZGNR without (black squares) and with (red triangles) ISO coupling obtained by first-principles calculations. The insets are a zoom in of the band spectra close to the Fermi surface.

spectra, but the ISO coupling can reduce the gaps. The first-principles band structure near Fermi surface of 5-AGNR is shown in Figure 5. Without ISO interaction, the band gap is 0.5379 eV. When the ISO coupling is considered, the band gap becomes smaller. As Figure 6 depicts, the change of the gap  $\Delta E$  decreases when  $N$  increases from 8 to 35, which is in good agreement with the results of TB method except  $N = 5$ . In 5-AGNR, the gap change is smaller in TB method than that expected. In TB method, we do not consider the change of the carbon-carbon bond length on the edge. As the smallest width metallic AGNR, 5-AGNR, is affected most by the edge. So, the model may not exactly express the ISO interaction in 5-AGNR.

Next, we consider the ZGNRs with the widths for  $N = 3, 4, 5, 6$ . Without ISO coupling, although the bands are self-avoiding, the ZGNRs are metallic. In the presence of ISO interaction, the bands split, and a gap is opened. Figure 7 displays the band structures near Fermi surface of 5-ZGNR and 4-ZGNR in the presence and absence of the ISO interaction. Increasing the relativistic potential by 300 times, the band gap changes from  $1.9 \times 10^{-3}$  eV to  $1.0 \times 10^{-5}$  eV. Since the ISO-opened gap is the second power of

the potential expected from the perturbation theory, final results which are obtained through dividing the gaps gotten from VASP by 90000 are  $2.0 \times 10^{-6}$  meV and  $1.0 \times 10^{-7}$  meV, respectively. This method was verified of being effectual by the first-principles calculations in [4]. Both first-principles calculations and TB approximation demonstrate that with the increase of the widths for even chains, the gaps decrease rapidly.

## 5. Summary

In summary, we have investigated the ISO effects in ZGNRs and AGNRs within four orbital TB approximation and first-principles calculations. In TB method, for metallic AGNRs and the ZGNRs with even chains, a gap is opened in the spectra by ISO coupling while for the ZGNRs with odd chains, conduction and valence edge bands are still degenerated at  $K^Z = \pi/a$ . By first-principles calculations, the ISO coupling reduces the gaps for AGNRs with  $N = 3M-1$  and causes a gap in ZGNRs. The results show that the edge configuration and width affect the strength of the ISO coupling. The ISO interaction has a stronger effect

for AGNRs than for ZGNRs. Besides, the influence of ISO coupling is weaker on GNRs with larger width, which the edge affects less.

*Note Added.* Recently, a related preprint which addresses spin-orbit interactions in GNRs with more than 50 chains by four orbital TB method has been posted [26].

## Acknowledgments

The authors thank X. H. Zhang, Q. Wang, M. G. Xia, D. Q. Liu, N. Ma, and H. W. Chen for valuable discussions. This paper is supported by the Cultivation Fund of the Key Scientific and Technical Innovation Project, Chinese Ministry of Education (no. 708082) and NSFC with Grant 11074196. One of the authors (E. Zhang) is also supported by the Fundamental Research Funds for the Central Universities (no. xjj20100088).

## References

- [1] K. S. Novoselov, A. K. Geim, S. V. Morozov et al., “Electric field effect in atomically thin Carbon films,” *Science*, vol. 306, pp. 666–669, 2004.
- [2] A. H. Castro Neto, F. Guinea, N. M. R. Peres, K. S. Novoselov, and A. K. Geim, “The electronic properties of graphene,” *Reviews of Modern Physics*, vol. 81, no. 1, pp. 109–162, 2009.
- [3] C. L. Kane and E. J. Mele, “Quantum spin hall effect in graphene,” *Physical Review Letters*, vol. 95, no. 22, Article ID 226801, pp. 1–4, 2005.
- [4] H. Min, J. E. Hill, N. A. Sinitsyn, B. R. Sahu, L. Kleinman, and A. H. MacDonald, “Intrinsic and Rashba spin-orbit interactions in graphene sheets,” *Physical Review B*, vol. 74, no. 16, Article ID 165310, 5 pages, 2006.
- [5] D. Huertas-Hernando, F. Guinea, and A. Brataas, “Spin-orbit coupling in curved graphene, fullerenes, nanotubes, and nanotube caps,” *Physical Review B*, vol. 74, no. 15, Article ID 155426, 15 pages, 2006.
- [6] Y. Yao, F. Ye, X.-L. Qi, S.-C. Zhang, and Z. Fang, “Spin-orbit gap of graphene: first-principles calculations,” *Physical Review B*, vol. 75, no. 4, Article ID 041401, 4 pages, 2007.
- [7] O. Seïichiro, I. Yasuhito, K. Hiroshi, and J.-I. Inoue, “Intrinsic spin hall effect in graphene: numerical calculations in a multiorbital model,” *Physical Review B*, vol. 78, no. 12, Article ID 121403, 4 pages, 2008.
- [8] M. Gmitra, S. Konschuh, C. Ertler, C. Ambrosch-Draxl, and J. Fabian, “Band-structure topologies of graphene: spin-orbit coupling effects from first principles,” *Physical Review B*, vol. 80, no. 23, Article ID 235431, 5 pages, 2009.
- [9] A. De Martino, R. Egger, K. Hallberg, and C. A. Balseiro, “Spin-orbit coupling and electron spin resonance theory for carbon nanotubes,” *Physical Review Letters*, vol. 88, no. 20, Article ID 206402, pp. 1–4, 2002.
- [10] F. Kuemmeth, S. Ilani, D. C. Ralph, and P. L. McEuen, “Coupling of spin and orbital motion of electrons in carbon nanotubes,” *Nature*, vol. 452, no. 7186, pp. 448–452, 2008.
- [11] A. H. Castro Neto and F. Guinea, “Impurity-induced spin-orbit coupling in graphene,” *Physical Review Letters*, vol. 103, no. 2, Article ID 026804, 4 pages, 2009.
- [12] K. Nakada, M. Fujita, G. Dresselhaus, and M. S. Dresselhaus, “Edge state in graphene ribbons: nanometer size effect and edge shape dependence,” *Physical Review B*, vol. 54, no. 24, pp. 17954–17961, 1996.
- [13] L. Brey and H. A. Fertig, “Edge states and the quantized Hall effect in graphene,” *Physical Review B*, vol. 73, no. 19, Article ID 195408, 5 pages, 2006.
- [14] L. Brey and H. A. Fertig, “Electronic states of graphene nanoribbons studied with the Dirac equation,” *Physical Review B*, vol. 73, no. 23, Article ID 235411, 5 pages, 2006.
- [15] Y. Kobayashi, K. Fukui, T. Enoki et al., “Edge state on hydrogen-terminated graphite edges investigated by scanning tunneling microscopy,” *Physical Review B*, vol. 73, Article ID 125415, 8 pages, 2006.
- [16] Y. W. Son, M. L. Cohen, and S. G. Louie, “Energy gaps in Graphene nanoribbons,” *Physical Review Letters*, vol. 97, Article ID 216803, 4 pages, 2006.
- [17] S. Okada, “Energetics of nanoscale graphene ribbons: edge geometries and electronic structures,” *Physical Review B*, vol. 77, no. 4, Article ID 041408, 4 pages, 2008.
- [18] Y. W. Son, M. L. Cohen, and S. G. Louie, “Half-metallic graphene nanoribbons,” *Nature*, vol. 444, no. 7117, pp. 347–349, 2006.
- [19] L. Yang, C.-H. Park, Y.-W. Son, M. L. Cohen, and S. G. Louie, “Quasiparticle energies and band gaps in graphene nanoribbons,” *Physical Review Letters*, vol. 99, no. 18, Article ID 186801, 4 pages, 2007.
- [20] M. Zarea and N. Sandler, “Electron-electron and Spin-orbit interactions in armchair graphene ribbons,” *Physical Review Letters*, vol. 99, no. 25, Article ID 256804, 4 pages, 2007.
- [21] M. Zarea, C. Büsser, and N. Sandler, “Unscreened coulomb interactions and the quantum spin hall phase in neutral zigzag graphene ribbons,” *Physical Review Letters*, vol. 101, no. 19, Article ID 196804, 4 pages, 2008.
- [22] M. Zarea and N. Sandler, “Quantum spin hall phase in neutral zigzag graphene ribbons,” *Physica B*, vol. 404, no. 18, pp. 2694–2698, 2009.
- [23] G. Kresse and J. Furthmüller, “Efficient iterative schemes for ab initio total-energy calculations using a plane-wave basis set,” *Physical Review B*, vol. 54, no. 16, pp. 11169–11186, 1996.
- [24] P. E. Bläuel, “Projector augmented-wave method,” *Physical Review B*, vol. 50, pp. 17953–17979, 1994.
- [25] J. P. Perdew, K. Burke, and M. Ernzerhof, “Generalized gradient approximation made simple,” *Physical Review Letters*, vol. 77, no. 18, pp. 3865–3868, 1996.
- [26] M. P. Lopez-Sancho and M. C. Muñoz, “Intrinsic spin-orbit interactions in flat and curved graphene nanoribbons,” *Physical Review B*, vol. 83, no. 7, Article ID 075406, 9 pages, 2011.

## Research Article

# Pore Structure Control of Ordered Mesoporous Silica Film Using Mixed Surfactants

Tae-Jung Ha,<sup>1</sup> Hyeon-Gyoon Im,<sup>1</sup> Seok-Jin Yoon,<sup>2</sup> Ho Won Jang,<sup>2</sup> and Hyung-Ho Park<sup>1</sup>

<sup>1</sup> Department of Materials Science and Engineering, Yonsei University, 134 Sinchon-dong, Seodaemun-gu, Seoul 120-749, Republic of Korea

<sup>2</sup> Electronic Materials Research Center, Korea Institute of Science and Technology, Seoul 130-650, Republic of Korea

Correspondence should be addressed to Hyung-Ho Park, hhpark@yonsei.ac.kr

Received 23 December 2010; Revised 17 March 2011; Accepted 19 April 2011

Academic Editor: Shaogang Hao

Copyright © 2011 Tae-Jung Ha et al. This is an open access article distributed under the Creative Commons Attribution License, which permits unrestricted use, distribution, and reproduction in any medium, provided the original work is properly cited.

Materials with nanosized and well-arranged pores have been researched actively in order to be applied to new technology fields. Especially, mesoporous material containing various pore structures is expected to have different pore structure. To form a mixed pore structure, ordered mesoporous silica films were prepared with a mixture of surfactant; Brij-76 and P-123 block copolymer. In mixed surfactant system, mixed pore structure was observed in the region of P-123/(Brij-76 + P-123) with about 50.0 wt.% while a single pore structure was observed in regions which have large difference in ratio between Brij-76 and P-123 through the X-ray diffraction analysis. Regardless of surfactant ratio, porosity was retained almost the same. It is expected that ordered mesoporous silica film with mixed pore structure can be one of the new materials which has distinctive properties.

## 1. Introduction

Porous materials are classified into several kinds such as microporous, mesoporous, and macroporous by their pore size according to the IUPAC (International Union of Pure and Applied Chemistry) notation [1]. The microporous materials have pore diameter less than 2 nm, and the macroporous materials have pore diameter greater than 50 nm. The mesoporous materials contain pores with diameter between 2 and 50 nm. They have been still researched since 1970s, and research in this field has steadily grown [2]. They have low density, large surface area, insulating property, and higher elastic modulus than nonordered mesoporous materials. For these properties, it was expected that they can be used in various application fields such as sensor, electronic, membrane, gas storage, adsorbent, catalyst support, and so on [3–5]. Silica-based materials, with nanosized pores, were discovered in 1992 by the researchers of the Mobil Oil Corporation [6]. These materials were first obtained as powders by mixing organic surfactant with silica precursor. Mesoporous thin films have been obtained more recently using the evaporation-induced self-assembly (EISA) method, developed by Lu et al. in 1997 [7]. EISA method is a

way to form micelles using surfactant, and a driving force for the formation of micelle is to reduce contact area between hydrocarbon chain and hydrophilic solvent [8]. When the concentration of the solution is below the critical micelle concentration (cmc), surfactant molecules can move around in solution without making micelles [9]. With evaporation of solvent, above cmc, the concentration of solution increases, so surfactant molecules start making micelles. After that, micelles stack up and form an ordered structure, and then finally, ordered mesoporous silica film can be obtained through calcination to remove the organic surfactant. There are several variables of forming ordered mesoporous structure such as reactant concentration, synthesis temperature, pH of solution, and the nature of surfactant. However, the effects of mixed surfactants on ordered mesoporous silica are hardly known because there have been several researches related with single surfactant, but there have been only few researches with mixed surfactants [10–17]. Lan Chen et al. made their studies on the mixture of various surfactants and synthesized the bimodal structure in P123-P65-25R4 system. But new ordered pore structure was not discovered. Therefore, further research is needed about ordered the mesoporous silica film using mixed surfactant.

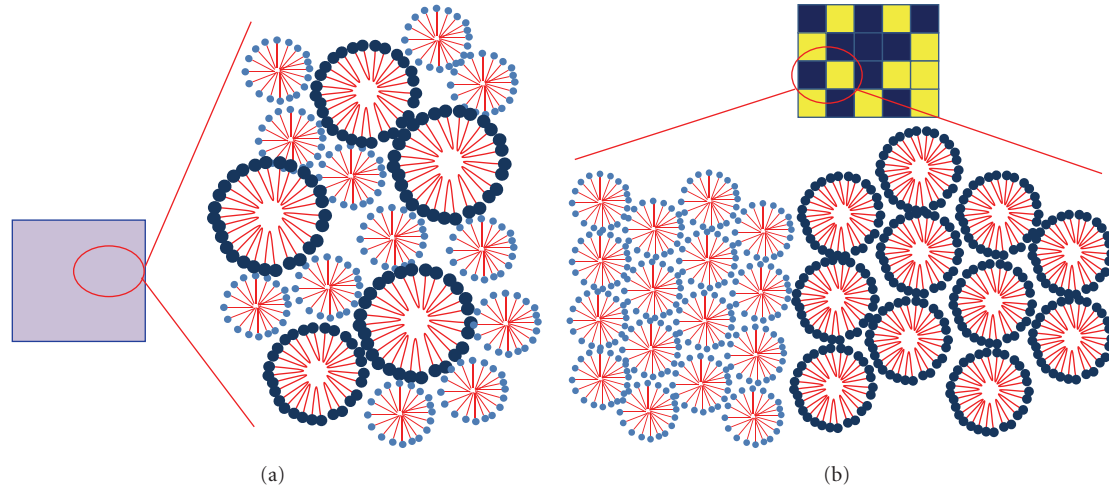


FIGURE 1: Possible states of the structure of the micelles; (a) nonseparated state and (b) separated state.

Understanding the correlation between structure and mixed surfactant can be deployed on a commercial scale.

Density of material influences on some of the other physical properties of material. Refractive index, for example, is a kind of property which is related with density of the material. Because mesoporous materials have pores, if we control the pore structures of the mesoporous material intentionally, we can get the material with various densities using mixed surfactants. Thus, we can have the material that has different refractive indices although it is composed entirely of the same chemical species. Through the control of the thickness of regions with different indices, we can modify transmission and reflection of light, and it could be applied to several fields such as high reflective glass and transparent thermal insulating materials. Also, processing steps can be reduced by using mixed surfactant system. There have been several reports about ordered mesoporous silica using surfactant Brij-76 or P-123. According to the researches, Brij-76 is known that it can make 2D hexagonal, BCC, and lamellar structure, and P-123 is known that it can make 2D hexagonal and BCC structure [18–20].

In this study, mesoporous silica film was obtained using two surfactants, Brij-76 and P-123, with various molar ratios. The pore structure variation according to the molar ratio of the surfactants was analyzed.

## 2. Experimental Procedure

Ordered mesoporous silica films were synthesized by the EISA method as follows. Firstly, EtOH (Duksan, 99.9%) was used as a solvent. The Brij-76 ( $C_{18}H_{37}(OCH_2CH_2)_{10}OH$ , Aldrich) and the P-123 block copolymer ( $H(OCH_2CH_2)_{10} \cdot (OCH_2CH_2CH_2)_{70}(OCH_2CH_2)_{10}OH$ , Aldrich) were dissolved in the solvent, and acidified  $H_2O$  was added. After stirring for 1 h, TEOS (Fluka, 98%) was sequentially added to the solution as silica precursor. The final molar ratio of TEOS:EtOH: $H_2O$ :HCl:mixed surfactants was 1:20:5:0.01:0.05, and the weight ratio of the mixed

surfactants (P-123/(Brij-76 + P-123)) was changed from 0 to 100 wt.% having 12.5 wt.% interval. After 30 min, a sol was spin-coated on silicon wafers at 3000 rpm for 30 sec at 23°C and a relative humidity of 30%. The used silicon wafer is (100)-oriented and its surface is hydrophilic caused by RCA-1 cleaning. To remove the block copolymer, ordered mesoporous silica films were calcined at 400°C for 2 h at a heating rate of 1°C/min in oxygen atmosphere.

To investigate the ordered pore structure, X-ray powder-diffraction (XRD) patterns were collected using Cu  $K\alpha$  radiation with wavelength of 1.5418 Å. The porosity of the film was measured by ellipsometry. The microstructural images of the mesoporous silica film were obtained using a transmission electron microscope (TEM, JEOL JEM-4010) at 400 kV.

## 3. Pore Structure Model

Two kinds of surfactants, Brij-76 and P-123, are different in several properties. Among them, especially, Brij-76 has lower molecular weight (M.W. of Brij-76 and P-123 are 710 and 5750, resp.), and the chain length of Brij-76 is shorter. As a result, it is expected that the micelle of Brij-76 is smaller than that of P-123, so they can make different pore structures above cmc. Therefore, pore structure synthesized using mixed surfactant which consists of Brij-76 and P-123 can be suggested as two models on the assumption that micelles are made by only same the kind of surfactant. They are nonseparated and separated states. Nonseparated state is a state which has a region with randomly mixed micelles, so it has disordered and isotropic pore structure as shown in Figure 1(a). Two kinds of micelles should be formed in similar rates in order to form nonseparated state. Therefore, each surfactant should have similar cmc in this case. Separated state is a state with the mixture of regions with homogeneously packed micelles, so it can be assembly of ordered pore structures as shown in Figure 1(b). Two kinds of surfactants should have very different cmc to form

separated state. We can control pore structures using the rate of the micelle formation in this case. If ordered mesoporous silica film is made by mixed surfactant which consisted of Brij-76 and P-123, it is expected a separated state model due to large difference of cmc in this report.

#### 4. Results and Discussion

Figure 2 shows XRD spectra of ordered mesoporous silica films according to the weight ratio of mixed surfactants (P-123/(Brij-76 + P-123)). Only one peak was detected when P-123/(Brij-76 + P-123) is from 0 to 25.0 and from 75.0 to 100 wt.%. It is the peak of the pore structure formed by Brij-76 and appeared at  $2.91^\circ$  in region of P-123/(Brij-76 + P-123) from 0 to 25.0 wt.% [18]. Also, the d-spacing which means a distance between pores is about 3 nm. In the region of P-123/(Brij-76 + P-123) from 75.0 to 100 wt.%, the peak is caused by the pore structure formed by P-123 and appeared at  $2.26^\circ$ , and d-spacing corresponds to about 3.9 nm [21]. That shows the micelle size of P-123 is bigger than that of Brij-76 because that the size of surfactant P-123 is bigger. In case of P-123/(Brij-76 + P-123) is 12.5, 25.0, 75.0, and 87.5 wt.%, there also was one peak of each, little bit shifted. That means the small amount of minor surfactant hinders making pore structure formed by major surfactant instead of making separated phase. At the point of 50.0 wt.% of P-123/(Brij-76 + P-123), two XRD peaks were observed. That means the ordered mesoporous silica film had mixed pore structure, and each surfactant was enough to make its own pore structure. It can be explained as that Brij-76 has lower cmc value (0.002 g/L at 298 K) than the cmc value of P-123 (0.045 g/L at 298 K), so micelles of Brij-76 were formed earlier than micelles of P-123 [22, 23]. In addition, seeing that the intensity of the XRD peak formed by Brij-76 is higher than that by P-123, pore structure formed by the micelles of Brij-76 was developed more ordered for the same reason. In case of 37.5 and 62.5 wt.% in P-123/(Brij-76 + P-123), two XRD peaks were detected, so there existed mixed pore structures in the region from 37.5 to 62.5 wt.%. Therefore, it was expected transition region existed that between 37.5 and 62.5 wt.%. As a result, it was considered that the mixed surfactant formed the separated state between two models.

Figure 3 shows full width at half maximum (FWHM) values of the specimens. In the region of P-123/(Brij-76 + P-123) from 0 to 37.5 wt.%, FWHM values slightly increased, so it indicated that XRD peaks became broad. In other words, it implies that ordering of the pores decreased. The reason is that the insufficient amount of surfactant cannot make micelles, and it influences on the formation of the structure of micelles and the development of the micelles of another kind of surfactant negatively [24, 25]. Therefore, the formation of the micelle structure was hindered by the minor surfactant of P-123. Similarly, in region of P-123/(Brij-76 + P-123) from 62.5 to 100 wt.%, hindrance of the minor surfactant of Brij-76 occurred, and ordering of the pores decreased as P-123/(Brij-76 + P-123) went down from 100 to 62.5 wt.%. However, in the region of P-123/(Brij-76 + P-123) from 37.5 to 62.5 wt.%, FWHM value rapidly

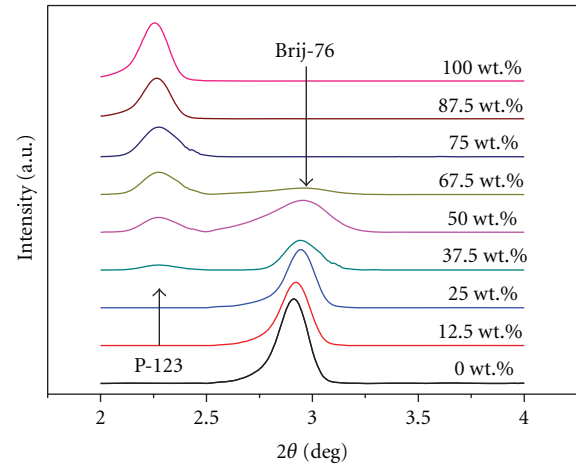


FIGURE 2: XRD patterns of mesoporous silica film along the weight ratio of mixed surfactant (P-123/(Brij-76 + P-123)).

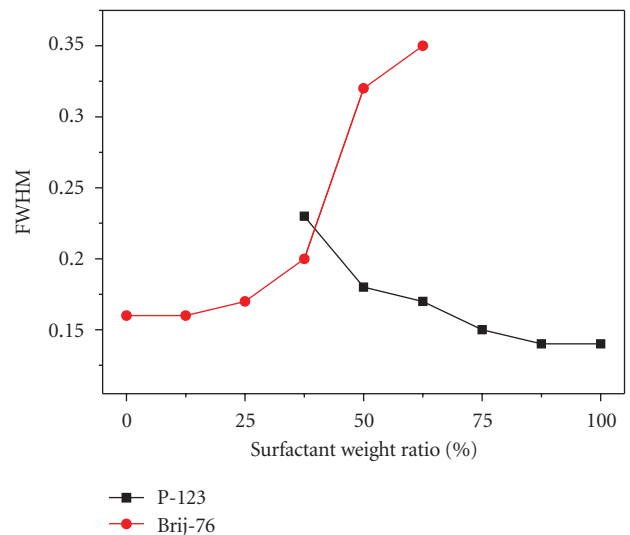


FIGURE 3: FWHM of mesoporous silica film along the mass ratio of mixed surfactants (P-123/(Brij-76 + P-123)).

increased, and XRD peaks became very broad. That means each kind of surfactant was enough to make two kinds of its own micelles, so two kinds of micelles formed each pore structure and hindered each other. That is, micelles hindered the formation of micelle structure, not surfactants. It was considered that the reason about the change of the FWHM value was based on the difference of hindrance between micelle and surfactant.

Figure 4 shows the porosity of ordered mesoporous silica film according to the weight ratio of mixed surfactant (P-123/(Brij-76 + P-123)). The porosity decreased in the region of P-123/(Brij-76 + P-123) from 0 to 50.0 wt.% and increased in the region of P-123/(Brij-76 + P-123) from 50.0 to 100 wt.% slightly. It indicates that the small amount of another kind of surfactant cannot contribute to porosity because the small number of surfactants cannot make micelles and only interrupt the pore structure. In case

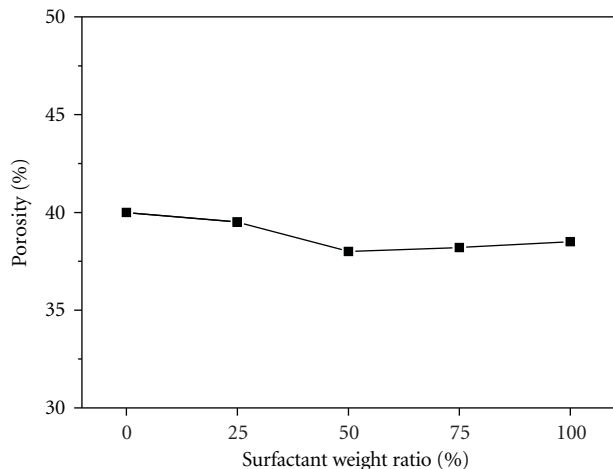


FIGURE 4: Porosity of mesoporous silica film along the weight ratio of mixed surfactants (P-123/(Brij-76 + P-123)).

of P-123/(Brij-76 + P-123) of 50.0 wt.%, the porosity is the lowest value. This is because two kinds of micelles formed each pore structure and hindered each other as mentioned above. It was also confirmed by XRD peaks in Figure 2. Thus, it implies that pore structure in case of P-123/(Brij-76 + P-123) of 50.0 wt.% is less ordered than in case of P-123/(Brij-76 + P-123) of 0 or 100 wt.%. However, taken as a whole, it was not considerable change of the porosity, so we could conclude that most of the added surfactant participated in the formation of pores, and the porosity depended on the total amount of surfactants regardless of the kind of surfactant.

To confirm a mixed pore structure obtained from XRD result of mesoporous silica film with 50 wt.% P-123/(Brij-76 + P-123) in Figure 2, the microstructure was observed through TEM measurement and given in Figure 5. Two different domains, highly ordered mesostructure and low ordered mesostructure, were observed in TEM image of the film. The inter pore distance of highly ordered mesostructure was about 3.3 nm, and that of low ordered mesostructure was about 4.7 nm. The highly ordered mesostructure corresponds to the domain formed by Brij-76, and the low ordered mesostructure corresponds to the domain formed by P-123 when comparing with XRD results. The inter pore distances in the TEM images were larger than those in XRD results. This enlargement in the TEM images could be caused by a diffused image of pores from a misorientation between a pore alignment direction and an electron beam incident direction. However, the inter pore distance ratios of two kinds of pore structure were similar, for example, 1.3 with XRD and 1.4 with TEM. Therefore, it could be concluded that the mesoporous silica film could have a mixed two different pore structures when using two different surfactants such as Brij-76 and P-123.

## 5. Conclusions

Ordered mesoporous silica films were synthesized using mixed surfactant, Brij-76 and P-123. Two kinds of mixed

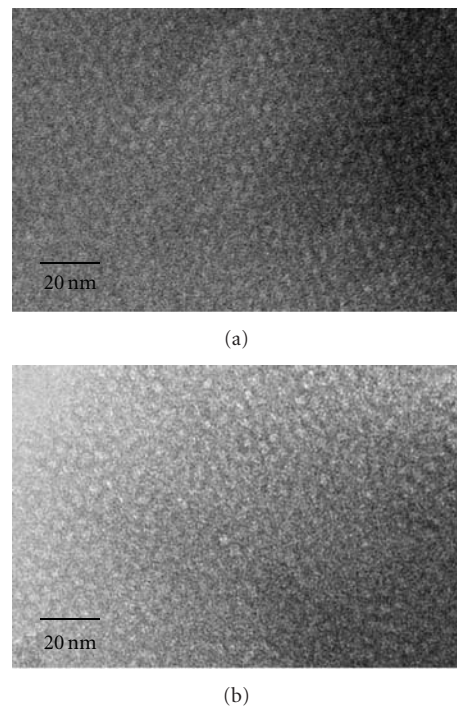


FIGURE 5: Microstructures of mesoporous silica film with the composition of 50 wt.% (P-123/(Brij-76 + P-123)); (a) the domain formed by Brij-76, and (b) the domain formed by P-123.

pore structures, nonseparated state and separated state, were expected to be formed. The mixture of two ordered pore structures is possible in case of the separated state, and surfactants which have very different cmc are needed. Results of XRD pattern showed the mixture of ordered pore structure in the region of P-123/(Brij-76 + P-123) from 37.5 to 62.5 wt.%. XRD peaks of ordered pore structure became broad due to hindrance by surfactant and/or micelle. The porosity depended on the total amount of surfactants regardless of the kind.

## Acknowledgments

This study was supported by a grant from the Fundamental R&D Program for Core Technology of Materials funded by the Ministry of Knowledge Economy, Republic of Korea. Experiments at PLS were supported in part by MEST and POSTECH.

## References

- [1] J. Rouquerol, D. Avnir, C. W. Fairbridge et al., "Recommendations for the characterization of porous solids (Technical Report)," *Pure and Applied Chemistry*, vol. 66, p. 1739, 1994.
- [2] V. Chiola, J. E. Ritsko, and C.D. Vanderpool, Process for producing low-bulk density silica, U.S. Patent 3556725, 1971.
- [3] S. Inagaki, S. Ogata, Y. Goto, and Y. Fukushima, "Mesoporous materials derived from layered silicates and the adsorption properties," *Studies in Surface Science and Catalysis*, vol. 117, pp. 65–76, 1998.

- [4] R. Ryoo, J. M. Kim, C. H. Ko, and C. H. Shin, "Disordered molecular sieve with branched mesoporous channel network," *Journal of Physical Chemistry*, vol. 100, no. 45, pp. 17718–17721, 1996.
- [5] S. E. Park, "Application of Mesoporous Molecular Sieves," *Chemistry World*, vol. 38, no. 11, pp. 30–39, 1998.
- [6] C. T. Kresge, M. E. Leonowicz, W. J. Roth, J. C. Vartuli, and J. S. Beck, "Ordered mesoporous molecular sieves synthesized by a liquid-crystal template mechanism," *Nature*, vol. 359, no. 6397, pp. 710–712, 1992.
- [7] Y. Lu, R. Ganguli, C. A. Drewien et al., "Continuous formation of supported cubic and hexagonal mesoporous films by sol-gel dip-coating," *Nature*, vol. 389, no. 6649, pp. 364–368, 1997.
- [8] R. Nagarajan, *Structure-Performance Relationships in Surfactants*, part 1.1, Marcel Dekker, New York, NY, USA, 2003.
- [9] S. P. Moulik, "Micelles: self-organized surfactant assemblies," *Current Science*, vol. 71, no. 5, pp. 368–376, 1996.
- [10] N. Igarashi, K. A. Koyano, Y. Tanaka, S. Nakata, K. Hashimoto, and T. Tatsumi, "Investigation of the factors influencing the structural stability of mesoporous silica molecular sieves," *Microporous and Mesoporous Materials*, vol. 59, no. 1, pp. 43–52, 2003.
- [11] J. S. Choi, D. J. Kim, S. H. Chang, and W. S. Ahn, "Catalytic applications of MCM-41 with different pore sizes in selected liquid phase reactions," *Applied Catalysis A*, vol. 254, no. 2, pp. 225–237, 2003.
- [12] R. L. Putnam, N. Nakagawa, K. M. McGrath et al., "Titanium dioxide—surfactant mesophases and Ti-TMS1," *Chemistry of Materials*, vol. 9, no. 12, pp. 2690–2693, 1997.
- [13] D. Zhao, J. Feng, Q. Huo et al., "Triblock copolymer syntheses of mesoporous silica with periodic 50 to 300 angstrom pores," *Science*, vol. 279, no. 5350, pp. 548–552, 1998.
- [14] J. R. Matos, M. Kruk, L. P. Mercuri et al., "Ordered mesoporous silica with large cage-like pores: structural identification and pore connectivity design by controlling the synthesis temperature and time," *Journal of the American Chemical Society*, vol. 125, no. 3, pp. 821–829, 2003.
- [15] A. Doyle and B. K. Hodnett, "Stability of MCM-48 in aqueous solution as a function of pH," *Microporous and Mesoporous Materials*, vol. 63, pp. 53–57, 2003.
- [16] L. Z. Wang, J. L. Shi, J. Yu, W. H. Zhang, and D. S. Yan, "Temperature control in the synthesis of cubic mesoporous silica materials," *Materials Letters*, vol. 45, no. 5, pp. 273–278, 2000.
- [17] L. Chen, J. Xu, W. H. Zhang, J. D. Holmes, and M. A. Morris, "Syntheses of complex mesoporous silicas using mixtures of nonionic block copolymer surfactants: understanding formation of different structures using solubility parameters," *Journal of Colloid and Interface Science*, vol. 353, no. 1, pp. 169–180, 2011.
- [18] S.-B. Jung, T.-J. Ha, J.-B. Seon, and H.-H. Park, "Phase behavior of ordered mesoporous silica film prepared by Brij-76 block copolymer," *Microporous and Mesoporous Materials*, vol. 111, no. 1-3, pp. 188–193, 2008.
- [19] M. Yan, S. Dourdain, and A. Gibaud, "Analysis of water condensation in P123 templated 2D hexagonal mesoporous silica films by X-ray reflectivity," *Thin Solid Films*, vol. 516, no. 22, pp. 7955–7961, 2008.
- [20] P. K. Kipkemboi, P. C. Kiprono, and P. Kndalut, "Preparation of mesoporous silica with amphiphilic poly(oxyethylene)/poly(oxybutylene) diblock and poly(oxyethylene)/poly(oxypropylene) triblock copolymers as templates," *Indian Journal of Chemistry—Section A*, vol. 48, no. 4, pp. 498–503, 2009.
- [21] T.-J. Ha, H.-H. Park, S.-Y. Jung, S.-J. Yoon, J.-S. Kim, and H.W. Jang, "Effect of porosity on the Seebeck coefficient of mesoporous TiO<sub>2</sub> thin films," *Thin Solid Films*, vol. 518, no. 24, pp. 7196–7198, 2010.
- [22] S. K. Hait and S. P. Moulik, "Determination of critical micelle concentration (CMC) of nonionic surfactants by donor-acceptor interaction with iodine and correlation of CMC with hydrophile-lipophile balance and other parameters of the surfactants," *Journal of Surfactants and Detergents*, vol. 4, no. 3, pp. 303–309, 2001.
- [23] Y. L. Su and H. Z. Liu, "Temperature-dependent solubilization of PEO-PPO-PEO block copolymers and their application for extraction trace organics from aqueous solutions," *Korean Journal of Chemical Engineering*, vol. 20, no. 2, pp. 343–346, 2003.
- [24] F. Y. Wei, Z. W. Liu, J. Lu, and Z. T. Liu, "Synthesis of mesoporous MCM-48 using fumed silica and mixed surfactants," *Microporous and Mesoporous Materials*, vol. 131, no. 1–3, pp. 224–229, 2010.
- [25] C. Liu, S. Wang, Z. Rong, X. Wang, G. Gu, and W. Sun, "Synthesis of structurally stable MCM-48 using mixed surfactants as co-template and adsorption of vitamin B12 on the mesoporous MCM-48," *Journal of Non-Crystalline Solids*, vol. 356, no. 25–27, pp. 1246–1251, 2010.

## Research Article

# Modeling and Simulation of Special Shaped SOI Materials for the Nanodevices Implementation

**Cristian Ravariu and Florin Babarada**

*Faculty of Electronics, "Politehnica" University of Bucharest, Splaiul Independentei 313, 060042 Bucharest, Romania*

Correspondence should be addressed to Cristian Ravariu, cr682003@yahoo.com

Received 30 December 2010; Accepted 4 May 2011

Academic Editor: Shaogang Hao

Copyright © 2011 C. Ravariu and F. Babarada. This is an open access article distributed under the Creative Commons Attribution License, which permits unrestricted use, distribution, and reproduction in any medium, provided the original work is properly cited.

In the industrial chain of the nanomaterials for electronic devices, a main stage is represented by the wafer characterization. This paper is starting from a standard SOI wafer with 200 nm film thickness and is proposing two directions for the SOI materials miniaturization, indexing the static characteristics by simulation. The first SOI nanomaterial is a sub-10 nm Si-film with a rectangular shape. The influence of the buried interface fixed charges has to be approached by the distribution theory. The second proposal studies the influence of the vacuum cavity in a "U" shaped SOI nanofilm. In all cases, with rectangular or "U" shape film, the simulations reveal transfer characteristics with a maximum and output characteristics with a minimum for sub-10 nm thickness of the SOI film.

## 1. Introduction

The modeling of the classical devices [1] or novel nanodevices [2] improves the design and explains some phenomena experimentally encountered [3].

In the SOI structures, two oxide-semiconductor interfaces exist with specific associated charges. Conventional models ignore the charges situated at the buried oxide-substrate interface, being focused just on the front and back channels conduction in the silicon film. All these fixed charges, expressed in electrons per  $\text{cm}^2$ , are physically spread into a small volume that becomes significant in ultra-thin films. This paper presents a suitable model for the flat-band voltage, based on the  $\delta$ -distribution strings, which include this bottom interface. Hence, the model accuracy increases in the SOI nanofilms materials, accordingly with our theory and numerical simulations. The electrons confinement effect is continuing to be studied in "U" shape SOI films. Whether the conduction channel occurs at the film bottom, the upper part of the SOI film was removed, monitoring the static characteristics of some SOI-MOSFETs.

This paper proposes two directions for the electrical characterization of the nano-SOI (silicon on insulator) materials, by simulation of the electrical characteristics of some

devices. The first class of the studied SOI transistors has a rectangular film shape. In this case, the effect of the buried interface fixed charges is modeled with the distribution theory [4, 5].

The classical HTA SIMOX (high temperature annealing separation by implanted oxygen), technology offers SOI wafers with 200 nm Si-film on 400 nm BOX with fixed charges in the range  $Q_{\text{ox}} = 10^{10} \div 10^{12} \text{ e/cm}^2$ , [6]. This charge is located in a shallow oxide slice. An SOI device has the interfaces:  $I_1$ -Si-film/BOX,  $I_2$ -BOX/Substrate, and eventually the upper interface  $I_0$ -gate oxide/Si-film; see Figure 1. The classical model strongly insists on the electric charges from  $I_0$  and  $I_1$  interfaces, [7]. In fact, all these fixed charges are physically spread into a small volume. In ultra-thin oxide structures, this kind of charge must be modeled as a bulk charge density [8].

This paper emphasizes that the effect of a fixed charges about  $10^{12} \text{ e/cm}^2$ , at the bottom interface  $I_2$  could be neglected in a classical SOI-MOSFET with 200 nm Si/400 nm BOX sizes, while it is the main charge in a nano-SOI-MOSFET with  $10 \text{ nm} \times 10 \text{ nm} \times 10 \text{ nm}$  Si/ $10 \text{ nm} \times 10 \text{ nm} \times 10 \text{ nm}$  BOX.

Transforming  $10^{12} \text{ e/cm}^2$  in  $10^{-2} \text{ e/nm}^2 = 1$  electron per  $10 \text{ nm} \times 10 \text{ nm}$  that means that the back interface

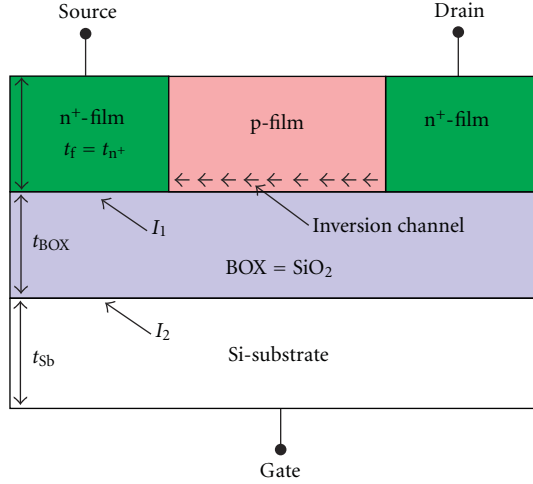


FIGURE 1: The current flow in a cross-section of a rectangular SOI-MOSFET, with SOI film thickness less than 200 nm.

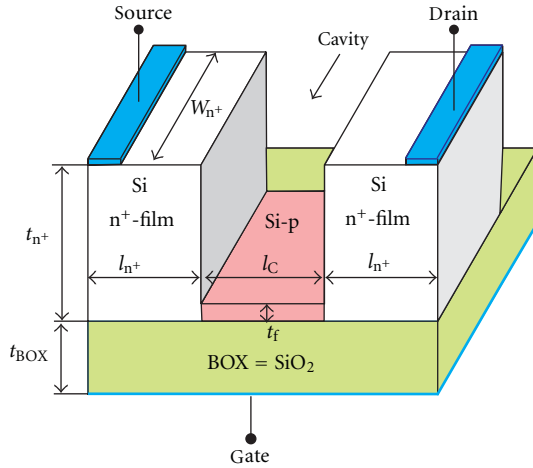


FIGURE 2: The conceptual architecture of the nanotransistor with a cavity, with SOI film thickness less than 10 nm.

$I_2$  (Si/BOX) is charged with one indivisible elementary charge. A model with a discontinuous function escapes from the integration operation. Just the Dirac distribution can correctly describe it as a bulk charge density.

Beside to the strong effect of the buried interface charge on the current through a SOI nanotransistor, the current confinement is modulated by the shape of the SOI material, in sub-10 nm Si-film devices, [9]. The influence of the vacuum cavity on the static characteristics, in a “U” shape nanotransistor, was the second direction of study for this paper; see Figure 2.

The notations from Figures 1 and 2 are  $t_{n^+}$ : the Si- $n^+$  region thickness,  $t_f$ : the Si-p film thickness,  $t_{\text{BOX}}$ : the buried oxide (BOX) thickness,  $t_{\text{Sb}}$ : the Si-substrate thickness,  $l_{n^+}$ : the Si- $n^+$  region length,  $l_c$ : the cavity length, and  $W_{n^+}$ : the Si- $n^+$  region width.

The joint of both subjects will be finally motivated by similar output characteristics with minimum and transfer

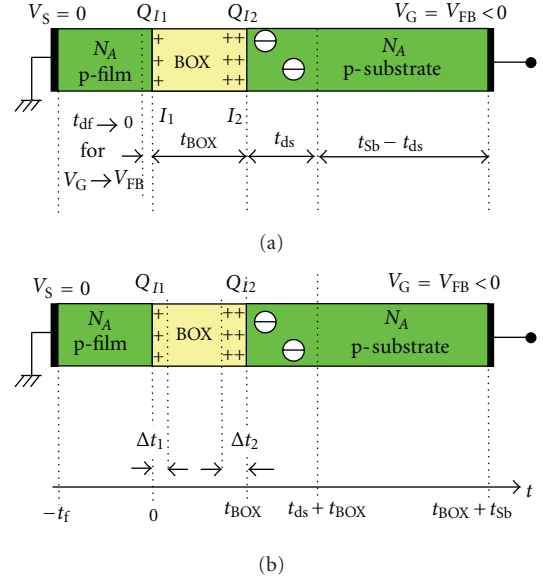


FIGURE 3: A segment of SOI structure with localization of interface charges (a) with  $Q_{I1}$ ,  $Q_{I2}$  as sheet charge density and (b) with  $Q_{I1}$ ,  $Q_{I2}$  scattered onto the  $\Delta t_1$ ,  $\Delta t_2$  thicknesses.

characteristics with maximum, both for rectangular shape sub-10 nm or “U” shaped SOI films.

## 2. The Analytical Model with Distributions

Firstly, the characterization of the back interface of a nano-SOI-MOSFET, using the pseudo-MOS transistor technique [10], will be presented. This is a dedicated transistor for the in situ electrical characterization, working like an upside down SOI-MOSFET controlled by the back gate, [11]. All unprocessed SOI wafers contain a pseudo-MOS transistor with two metals in contact with the semiconductor layer, as source and drain. The substrate acts like the gate contact in a classical SOI-MOSFET, Figure 1. One key parameter that contains information about the back interface charge is the flat band voltage,  $V_{\text{FB}}$ , [12]. This parameter is extracted from the measured  $I_D$ - $V_{\text{GS}}$  curves or directly from simulations with its definition.

In order to be focused just on the fixed interface charge density, others effects like interface traps, mobile ionic charge and metal semiconductor work function are neglected in the analytical model and in simulations.

The SOI structure associated with the pseudo-MOS transistor is modeled. Identical doping concentrations in film and substrate,  $N_A$ , are considered to avoid the film-substrate work function in the flat-band voltage expression.

The source and drain are grounded, while the gate is biased at  $V_{\text{FB}}$  voltage, Figure 3(a). By Poisson’s equation integration, the flat-band voltage  $V_{\text{FBC}}$  is computed by the classical method [13]

$$V_{\text{FBC}} = -\frac{Q_{I1}}{\epsilon_{\text{ox}}} \cdot t_{\text{BOX}} - \frac{(Q_{I1} + Q_{I2})^2}{2\epsilon_{\text{Si}}qN_A}, \quad (1)$$

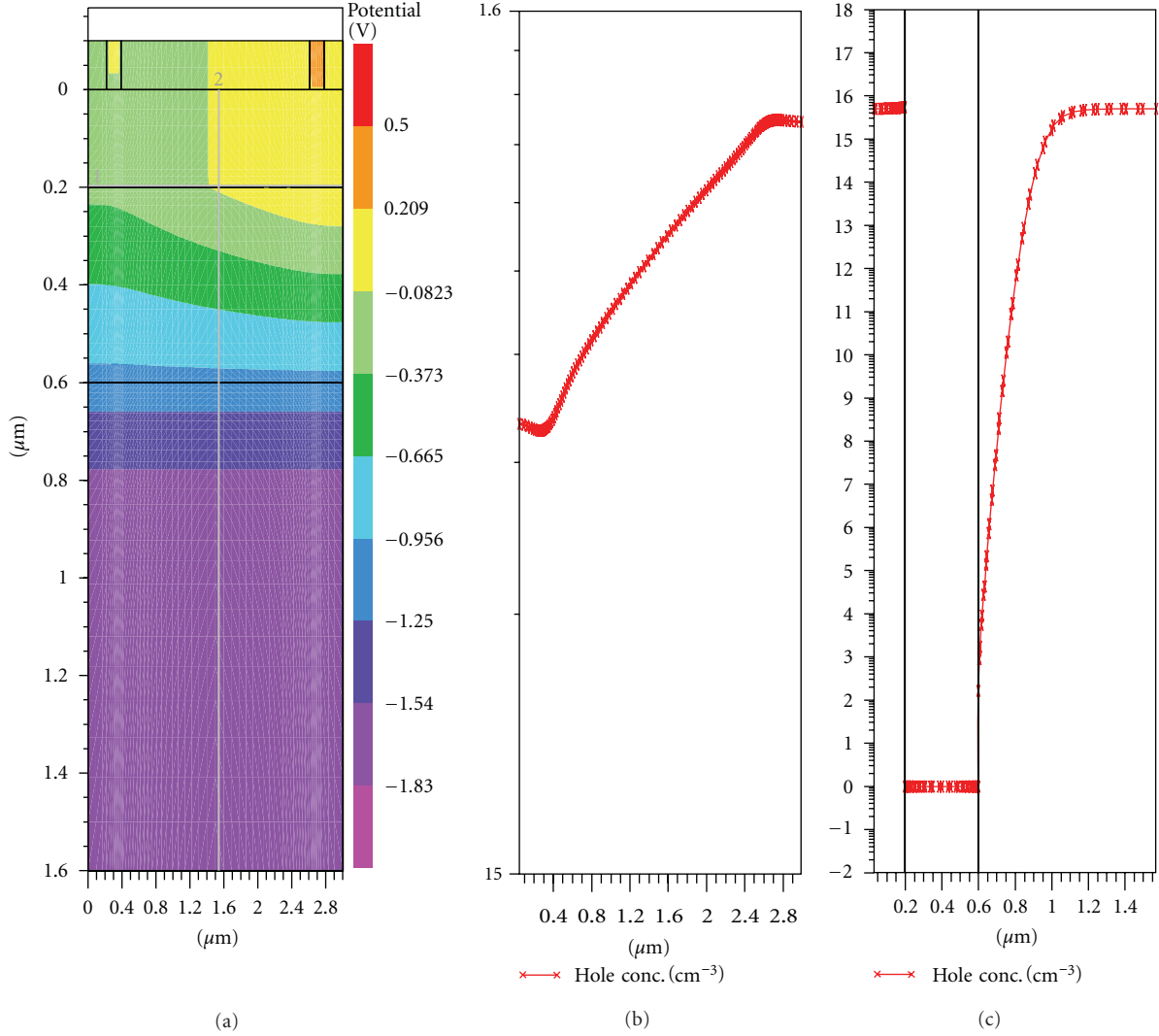


FIGURE 4: (a) The potential distribution in the 200 nm SOI structure; (b) the holes concentration across the structure; (c) the holes concentration along the structure.

where  $t_{\text{BOX}}$  is the buried oxide thickness,  $\epsilon_{\text{Si}}$ ,  $\epsilon_{\text{ox}}$ , respectively, are the dielectric permittivity of silicon and oxide,  $V_{\text{FBC}}$  is the classical flat-band voltage given by the condition of the potential zeroing in the entire SOI film. The depleted film thickness  $t_{\text{df}} \rightarrow 0$  for  $V_{\text{G}} \rightarrow V_{\text{FB}}$ ,  $Q_{I1}$ ,  $Q_{I2}$  are, respectively, the sheet charge densities from the upper and buried interface and the last term,  $V_{\text{FB-Sb}}$  models the substrate depletion on distance  $t_{\text{ds}}$  in Figures 3(a) and 3(b) presents the interface charges scattered into small volumes, as a real situation, both in micro- or nano-SOI structures. Hence, a relationship between surface charge density  $Q_I$  and the bulk electric charge density  $q_V$  for whatever  $I_1$  or  $I_2$  interface is

$$Q_I = \lim_{\Delta t \rightarrow 0} \int_0^{\Delta t} q_V \cdot dt = \lim_{\Delta t \rightarrow 0} q_V \cdot \Delta t, \quad (2)$$

where  $\Delta t$  is interpreted as a spreading coefficient. The surface charge  $Q_I$  was spread into an infinitesimal volume:  $\Delta t \cdot S$ , with

$\Delta t \rightarrow 0$  and  $q_V = ct$ ,  $S$  being the area. If  $q_V$  is modeled with a function like this

$$q_V = \begin{cases} q_S, \text{ expressed in } \text{e}/\text{cm}^3, & \text{for } t = 0, \\ 0, & \text{for } t \in \mathfrak{R} - \{0\}, \end{cases} \quad (3)$$

where  $q_S$  is a real number associated with  $Q_I/\Delta t$ . Then,  $Q_I$  becomes zero, accordingly with (2), escaping from the integration operation. In order to obtain  $Q_I$  finite in (2),  $q_V$  must tend to  $\infty$ , considering  $\Delta t \rightarrow 0$ . But this is a  $\delta$  distribution. On the horizontal axis  $Ot$ , along the SOI structure from Figure 2(a), the bulk charge density can be written with the Dirac distribution

$$q_V(t) = Q_{I1} \cdot \delta_0(t) + Q_{I2} \cdot \delta_{t_{\text{BOX}}}(t). \quad (4)$$

The electric field distribution is expressed as a Heaviside distribution after the first integration. The potential imposes a second integration that is difficult in distribution terms.

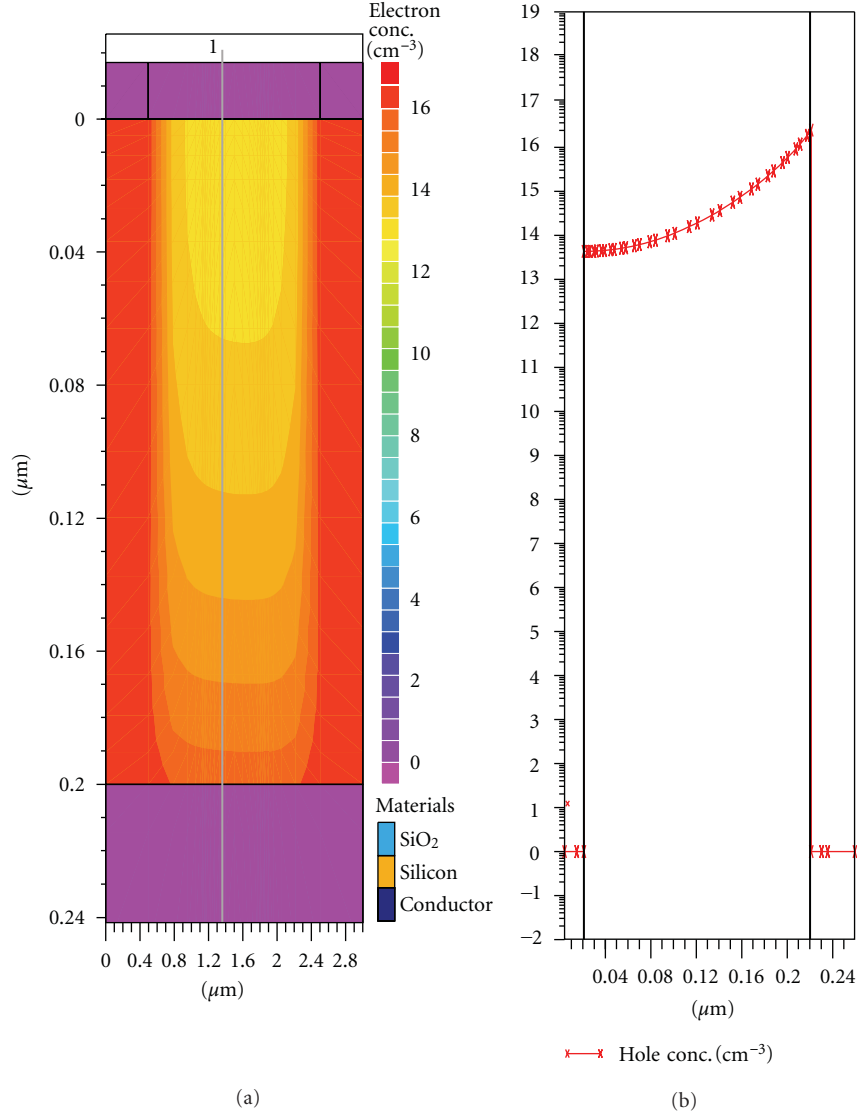


FIGURE 5: Detail in film for the electron concentration risen for a positive gate voltage.

Due to this reason, is preferred a model based on  $\delta$ -generator strings. The functional analysis demonstrated that Dirac distribution is the limit of the following string of regulates distribution, pulse-type [14]

$$D_{ti}(t) = \begin{cases} \frac{1}{\Delta t_i}, & \text{for } t \in [t_i, t_i + \Delta t_i], \\ 0, & \text{for } t \notin [t_i, t_i + \Delta t_i], \end{cases} \quad (5)$$

where  $t_i$  is the spatial coordinate for  $Q_{Ii}$ ,  $i = 1$  or  $2$  and  $\Delta t_i \rightarrow 0$  ( $\forall i$ ) represent the spreading coefficients for  $Q_{I1}$ ,  $Q_{I2}$ ; see Figure 2(b). Now, the bulk electric charge distribution can be written with  $\delta$ -generators string

$$q_V(t) = Q_{I1} \cdot D_0(t) + Q_{I2} \cdot D_{t_{\text{BOX}}}(t). \quad (6)$$

The string  $D_{ti}(t)$  has the advantage of being an integrable function. The integral  $\int_{-\infty}^{\infty} D_{ti}(t) dt$  gives 1 like  $\delta$  distribution. The convergence toward  $\delta$ -distribution is successfully fulfilled for  $\Delta t_i \rightarrow 0$ . In the old SOI technologies,  $\Delta t_i = 20 \text{ nm} =$

$2 \cdot 10^{-8} \text{ m}$  [15], but in the ultimate stage of nanotechnologies,  $\Delta t_i$  could reach the atomic sizes— $\Delta t_i \approx 0.3 \text{ nm} = 3 \cdot 10^{-10} \text{ m}$ , closer to zero, [16]. Hence, our model is more accurate for nanodevices. After two integration operations of the Poisson's equation, the following potential drops result:

$$\text{For } t \in (-t_f, 0) \rightarrow \Phi_{\text{film}} = 0,$$

$$\text{For } t \in (0, \Delta t_1) \rightarrow \Phi_{\Delta t_1} = -\frac{Q_{I1}}{2\epsilon_{\text{ox}}} \cdot \Delta t_1,$$

$$\text{For } t \in (\Delta t_1, t_{\text{BOX}} - \Delta t_2)$$

$$\rightarrow \Phi_{\text{BOX}} = -\frac{Q_{I1}}{\epsilon_{\text{ox}}} \cdot (t_{\text{BOX}} - \Delta t_1 - \Delta t_2), \quad (7)$$

$$\text{For } t \in (t_{\text{BOX}} - \Delta t_2, t_{\text{BOX}})$$

$$\rightarrow \Phi_{\Delta t_2} = -\frac{Q_{I1}}{\epsilon_{\text{ox}}} \cdot \Delta t_2 - \frac{Q_{I2}}{2\epsilon_{\text{ox}}} \cdot \Delta t_2.$$

Adding the previous voltages,  $\Phi_{\text{film}}$ ,  $\Phi_{\text{BOX}}$ ,  $\Phi_{\Delta t_1}$ ,  $\Phi_{\Delta t_2}$ —the potentials drops, respectively, over film, neutral oxide, and  $\Delta t_1$  and  $\Delta t_2$  regions from the buried oxide, with the potential drop over the depleted substrate,  $V_{\text{FB-Sb}}$ , the complete flat-band voltage expression with distribution terms,  $V_{\text{FBC}}$ , is

$$V_{\text{FBD}} = -\frac{Q_{I1}}{\epsilon_{\text{ox}}} \cdot \left( t_{\text{BOX}} - \frac{\Delta t_1}{2} \right) - \frac{Q_{I2}}{2\epsilon_{\text{ox}}} \cdot \Delta t_2 - \frac{(Q_{I1} + Q_{I2})^2}{2\epsilon_{\text{Si}} \cdot qN_A}. \quad (8)$$

If the spreading coefficients are approximated with zero ( $\Delta t_{1,2} = 0$ ), the new model (8) becomes the conventional model (1). The validity of the new model (8) will be discussed in the next paragraph, in comparison with classical model (1).

### 3. The Simulation Results for the SOI Structure with 200 nm Thickness

In this paragraph, the previous models (1) and (8) are tested using Atlas simulations of a pseudo-MOS transistor integrated on a SOI wafer with 200 nm Si-p-film and 400 nm buried oxide. The constructive data were [17]:  $t_{n+} = 0.2 \mu\text{m}$ ,  $t_{\text{BOX}} = 0.4 \mu\text{m}$ ,  $t_{\text{sb}} = 1 \mu\text{m}$ , the doping concentrations in film and substrate is  $N_A = 2 \times 10^{15} \text{cm}^{-3}$ .

The applied voltages were  $V_D = 0 \text{V} \dots + 4 \text{V}$ ,  $V_S = 0 \text{V}$  and  $V_G = 0 \text{V} \dots - 3 \text{V}$  in order to estimate the simulated flat-band voltage that must be applied on gate.

Figure 4(a) presents the potential distribution and the holes concentration in an intermediate situation at  $V_G = -1.8 \text{V}$ , through the structure with 200 nm Si-film thickness. A negative gate bias induces a holes crowding in the p-type film. Near drain, where  $V_{\text{GD}}$  is higher than  $V_{\text{GS}}$ , the holes reached  $p = 8 \times 10^{15} \text{cm}^{-3}$  and near source  $p = 4 \times 10^{15} \text{cm}^{-3} > 2 \times 10^{15} \text{cm}^{-3} = N_A$ , Figure 4(b). From the longitudinal holes distribution can be observed the holes concentration decreasing in the substrate; see Figure 4(c). This simulation proves the substrate depletion effect.

Figure 5 presents the electron concentration in the same structure with 200 nm film thickness. A positive gate bias induces an electron inversion channel in p-type film (e.g.,  $n|_{y=0.2\mu\text{m}} = 10^{16} \text{cm}^{-3} > 5 \cdot 10^{15} \text{cm}^{-3} = N_{\text{A-film}}$ ); see Figure 5.

Atlas takes into account the interface electric charge by the statements

$$\begin{aligned} \text{Interface } y_{\min} = 0.1 \quad y_{\max} = 0.5, \quad \text{QF} = 5e10, \\ \text{Interface } y_{\min} = 0.5 \quad y_{\max} = 0.8, \quad \text{QF} = 1e12. \end{aligned} \quad (9)$$

The metal semiconductor work function was zero for the source, drain, and gate contacts, defined as “neutral”. The simulated flat-band voltage value,  $V_{\text{FBS}}$  was searched accordingly with the theoretical definition. For  $V_S = 0 \text{V}$ , the  $V_G$  voltage was searched so that the potential in the film bottom becomes zero.

Figure 6 presents the potential distribution between source and gate, after Atlas running. Initially, the potential distribution was extracted for  $V_{\text{GS}} = 0 \text{V}$  in order to observe

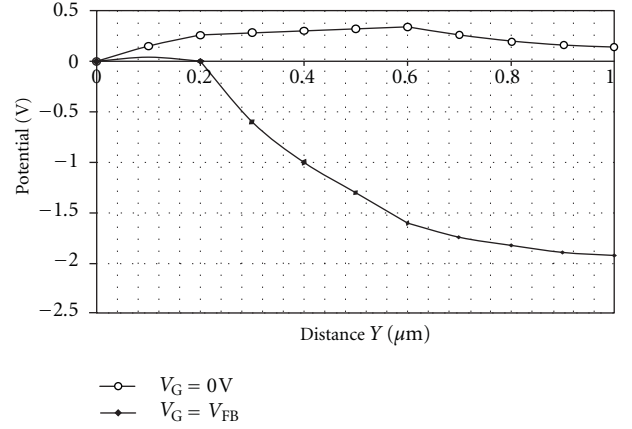


FIGURE 6: The potential distribution in the 200 nm structure between source and gate.

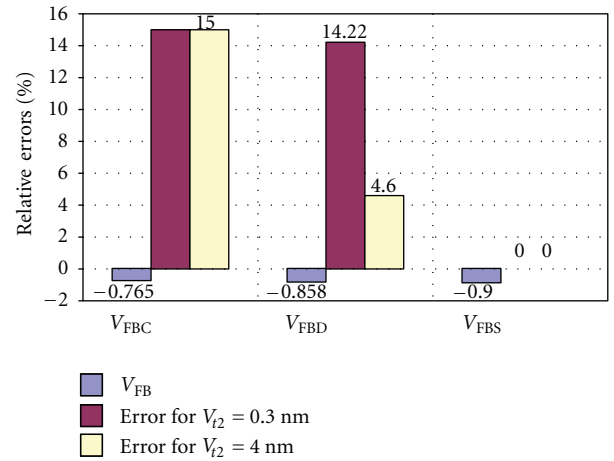


FIGURE 7: The flat-band voltages:  $V_{\text{FBS}} = -1.95 \text{V}$ ,  $V_{\text{FBC}} = -1.77 \text{V}$ , and  $V_{\text{FBD}} = -1.93 \text{V}$ , besides to the relative errors for  $V_{\text{FBC}}$ ,  $V_{\text{FBD}}$  in respect with  $V_{\text{FBS}}$ .

the potential bending in the absence of some external electrical voltages due to the interface charges densities  $Q_{I1}$  and  $Q_{I2}$ . In this case, the potential at the film bottom reaches  $+0.28 \text{V}$  at  $x = 0.2 \mu\text{m}$ ; see Figure 6. Then, the gate voltage was increased so that the potential at the coordinate  $x = 0.2 \mu\text{m}$  decreases to  $0 \text{V}$ . This occurs for  $V_{\text{GS}} = -1.95 \text{V}$  in Figure 6 consequently;  $V_{\text{FBS}} = -1.95 \text{V}$ .

On the other hand, the classical model (1) provides a fix value  $V_{\text{FBC}} = -1.77 \text{V}$  and the new model (8) based on the distribution generation strings gives  $V_{\text{FBD}} = -1.93 \text{V}$ , fitting the spreading coefficients to  $\Delta t_1 = 0.5 \text{nm}$  and  $\Delta t_2 = 7 \text{nm}$ .

All these results are briefly shown in Figure 7, where the old model (1) gives 9.3% error, while the new model (8) can adjust the error to 1.03%.

A comparison of the simulated parameter  $V_{\text{FBS}}$  with a measured flat-band voltage,  $V_{\text{FBM}}$ , is possible, monitoring the transfer characteristics of the pseudo-MOS transistor made on the SOI wafer with 200 nm Si-p-film and 400 nm buried oxide, [17]. In order to extract the flat-band voltage,

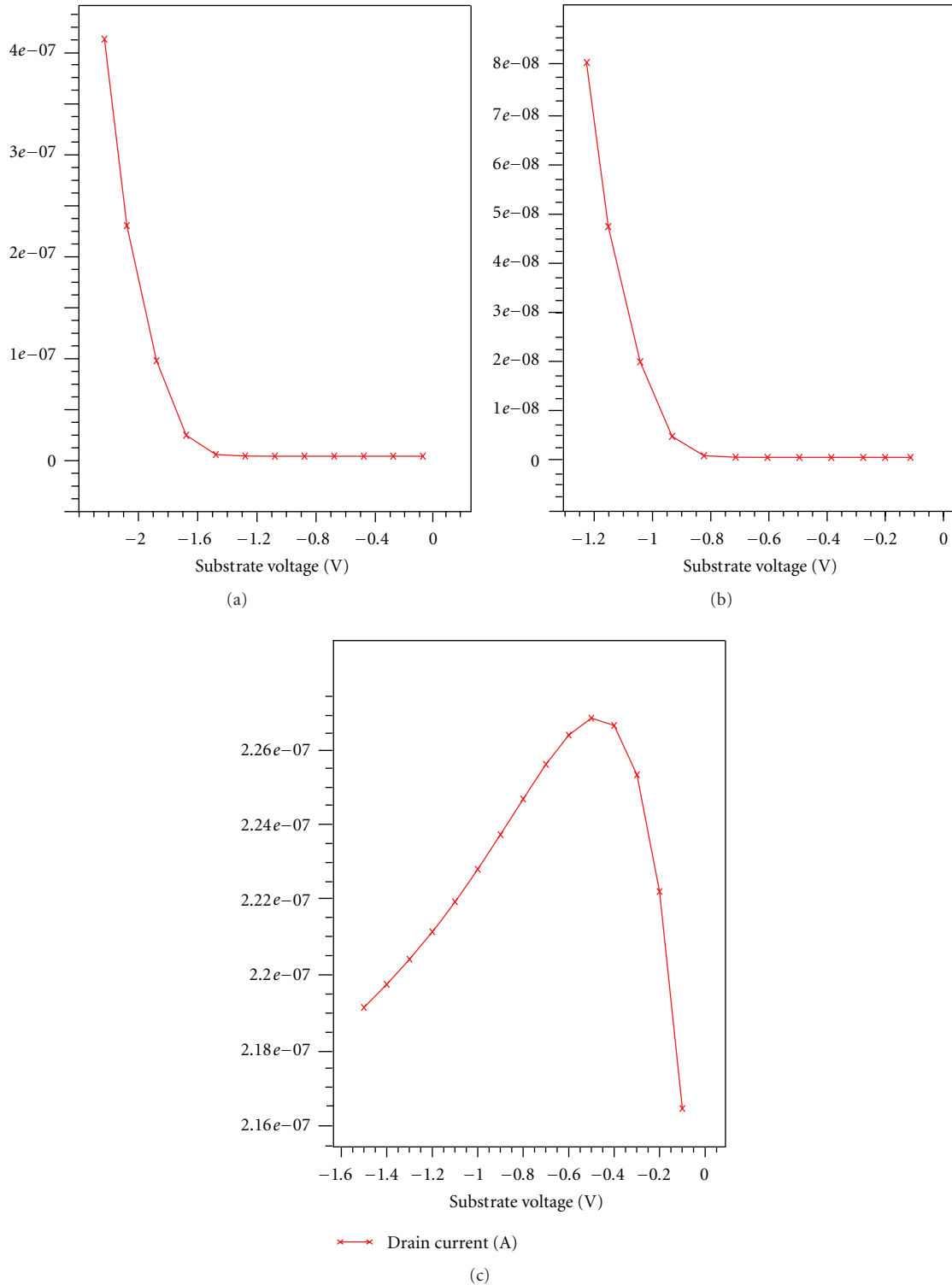


FIGURE 8: The  $I_D$ - $V_{GS}$  characteristics for (a) 50 nm (b) 10 nm and (c) 2 nm thickness of the semiconductor SOI film.

the source was grounded, while the drain was maintained at +0.3 V, and the gate voltage was varied from -5 V up to +5 V in order to induce the flat-band conditions in the device. From the transfer characteristics, the measured flat-band voltage results:  $V_{FBM} = -2.16$  V for p-type film and +4.25 V

for n-type film, [17, 18]. In our case, the closest values to the experimental parameter,  $V_{FBM} = -2.16$  V, are the simulated and distribution model:  $V_{FBS} = -1.95$  V and  $V_{FBD} = -1.93$  V. Obviously, the classical model (1),  $V_{FBC} = -1.77$  V, loses the accuracy, neglecting the buried oxide interface. However, the

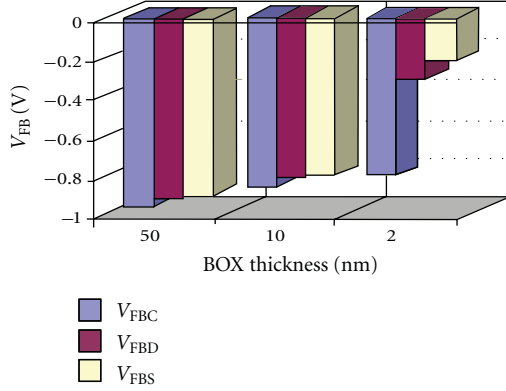


FIGURE 9: The flat-band voltages:  $V_{FBS}$ ,  $V_{FBC}$ , and  $V_{FBD}$ , besides to the relative errors for  $V_{FBC}$ ,  $V_{FBD}$  in respect to  $V_{FBS}$ , for  $t_f = 50$ , 10, and 2 nm.

discrepancy among experiments, simulations, and analytical values is still small at 200 nm film thickness and is predictable to become consistent for sub-20 nm films.

#### 4. Simulation Results for Sub-10 nm Rectangular SOI Structures with Interface Charges

The investigation of the nano-SOI-MOSFETs is continuing with the downscale of the film thicknesses: for Si-film from 200 nm to 50 nm, 10 nm, and 2 nm and for BOX layer from 400 nm to 50 nm, 10 nm, and 4 nm. The doping concentrations are  $N_A = 5 \times 10^{15} \text{ cm}^{-3}$  both in film and substrate. The interface electric charge densities are  $Q_{I1} = 5 \times 10^{15} \text{ e/cm}^2$  and  $Q_{I2} = 10^{12} \text{ e/cm}^2$ .

The simulated transfer characteristics show the evolution of the  $I_D$ - $V_{GS}$  curves from: (a) 50 nm, (b) 10 nm, (c) 2 nm thickness of the semiconductor SOI film; see Figure 8. The typical characteristic shape of a standard SOI-MOSFET is fulfilled till 10 nm. From these curves, the simulated flat-band voltage can be extracted, as the voltage that opens the accumulation channel and produces the current increases:  $V_{FBS} = -0.9 \text{ V}$  for 50 nm structure and  $V_{FBS} = -0.8 \text{ V}$  for 10 nm structure. Under this value, an  $I_D$ - $V_{GS}$  curve with a maximum occurs, probably due to the electrons confinement effect. The simulated flat-band voltage cannot be still extracted from the  $I_D$ - $V_{GS}$  curve.

In order to check these assessments, the output characteristics are also investigated, to observe the typical effect of transistor. Figure 8 comparatively presents the  $I_D$ - $V_{DS}$  curves for different semiconductor SOI thickness: 10 nm and 2 nm. The typical shape with saturation occurs till 10 nm film thickness. For sub-10 nm the characteristics takes atypical shape with minimum, Figure 8 for  $t_f = 2 \text{ nm}$ .

A comparison among the simulated, classical, and distribution flat-band voltage for  $t_f = 50 \text{ nm}$ , 10 nm, and 2 nm is available in Figure 9, besides to the error versus the  $V_{FBS}$ . This analysis proofs that the model (8) with distributions is closer to the simulations than the classical model (1), which provides higher errors at lower thicknesses.

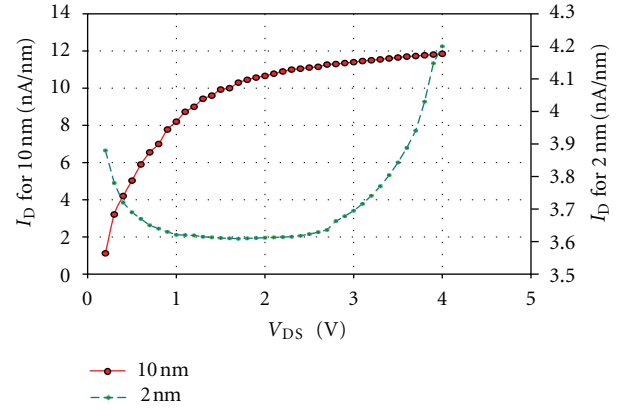


FIGURE 10: The  $I_D$ - $V_{DS}$  characteristics at  $V_{GS} = 3 \text{ V}$  and rectangular shape of the SOI film with 10 nm and 2 nm thickness.

Figure 10 comparatively presents the output characteristics when the drain-source voltage was increased from 0 V up to +5 V, at a constant  $V_{GS}$ , for two nanosizes of the SOI film.

Besides to the model with distribution accuracy, the prior simulations of the statics characteristics highlights classical shape of characteristics for  $t_f > 10 \text{ nm}$  and atypical shape for  $t_f < 10 \text{ nm}$ .

Another direction of the SOI nanotransistors investigation is related to a special shape of the SOI film. Taking into account that the current occurs only at the Si-film bottom, results that the 90% from the upper Si-film region does not participate to conduction. Hence, this Si-film region was removed in next simulations, obtaining a SOI nanotransistor with a cavity or “U” shaped.

#### 5. Simulation Results for Sub-10 nm Special Shaped SOI Nanotransistor without Interface Charges

In the simulations, the constructive data were those described in the paragraph 4. The aim of this paragraph is to highlight only the special shape effect of the semiconductor on the static characteristics.

The main physical effects included as “nanoeffects” were band to band tunnelling, Fowler-Nordheim tunnelling, Fermi distribution, including in the MODEL statement the following parameters: BBT, FNORD, and FERMI. Figure 11 presents the total current vectors in a structure with  $t_{n+} = 7 \text{ nm}$ ,  $t_f = 1 \text{ nm}$ , and  $t_{BOX} = 10 \text{ nm}$ , at  $V_{DS} = 4 \text{ V}$ ,  $V_{GS} = 3 \text{ V}$ , besides to the electrons concentration in the channel region. The vectors through the vacuum (emphasised by dotted line), proved the tunnel effect.

In Figure 12 family of curves  $I_D$ - $V_{GS}$  for  $y_{film} = 200 \text{ nm}$ , 10 nm, 1 nm, and 0.3 nm are presented. These curves have a maximum for  $y_{film} \leq 1 \text{ nm}$ , like SET transistor [19] or atypical nanodevices [20].

Figure 13 shows the curves  $I_D$ - $V_{DS}$  at  $V_{GS} = 3 \text{ V}$ . The shape of the  $I_D$ - $V_{DS}$  curves with a minimum proves the tunnel effect, [21].

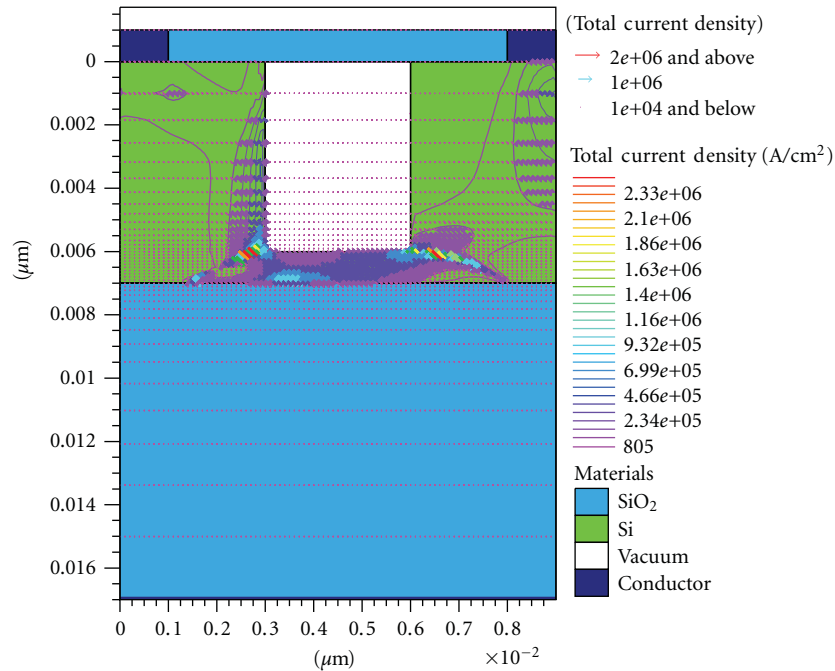


FIGURE 11: Total current vectors in the 1 nm transistor.

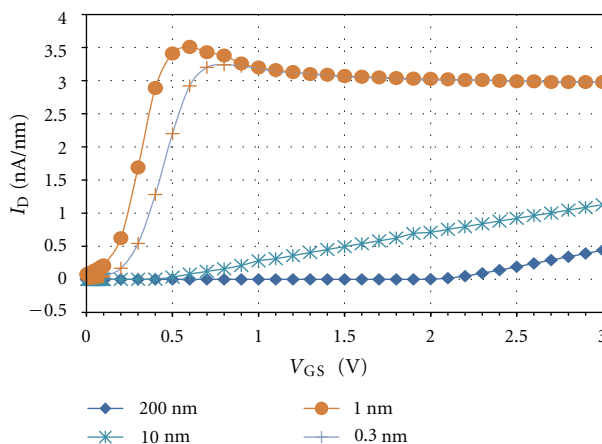
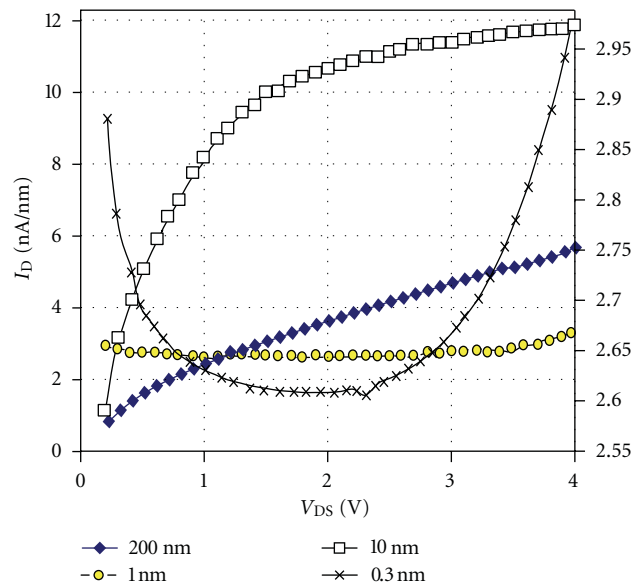
FIGURE 12: The  $I_D$ - $V_{GS}$  transfer characteristics.FIGURE 13: The  $I_D$ - $V_{DS}$  output characteristics.

Figure 14 presents the global potential distribution (left) and a detail of the electron concentration (right) for the 0.3 nm structure with cavity, biased at a high drain voltage in this last case:  $V_S = 0$  V,  $V_G = 3$  V, and  $V_D = 4$  V.

In this case, the saturation occurred, and an unbalanced electron distribution can be seen in the film  $1.1 \cdot 10^{16} \text{ cm}^{-3}$  in the source region,  $7 \cdot 10^{15} \text{ cm}^{-3}$  in the channel near the source,  $2 \cdot 10^{15} \text{ cm}^{-3}$  in the channel near the drain, and decrease up to  $1.4 \cdot 10^{15} \text{ cm}^{-3}$  in the drain, region at the film bottom; see Figure 14.

## 6. Possible Set Implementation

The single electron devices (SEDs) tend to become the main rivals for the sub-50 nm classical CMOS devices

[22]. Advantages of SED's are low-power dissipation, ultra-high-density of integration, a natural technology evolution inspired from miniaturized CMOS processes, and hence reasonable costs.

The simulations suggest the SET (single electron transistor) like behavior of the SOI nanotransistor with cavity for sub 1 nm film thickness. The electrons must be transferred from source to drain one by one [23].

As in the case of SOI-MOSFETs, a positive gate bias induces an electron inversion channel in the p-type film.

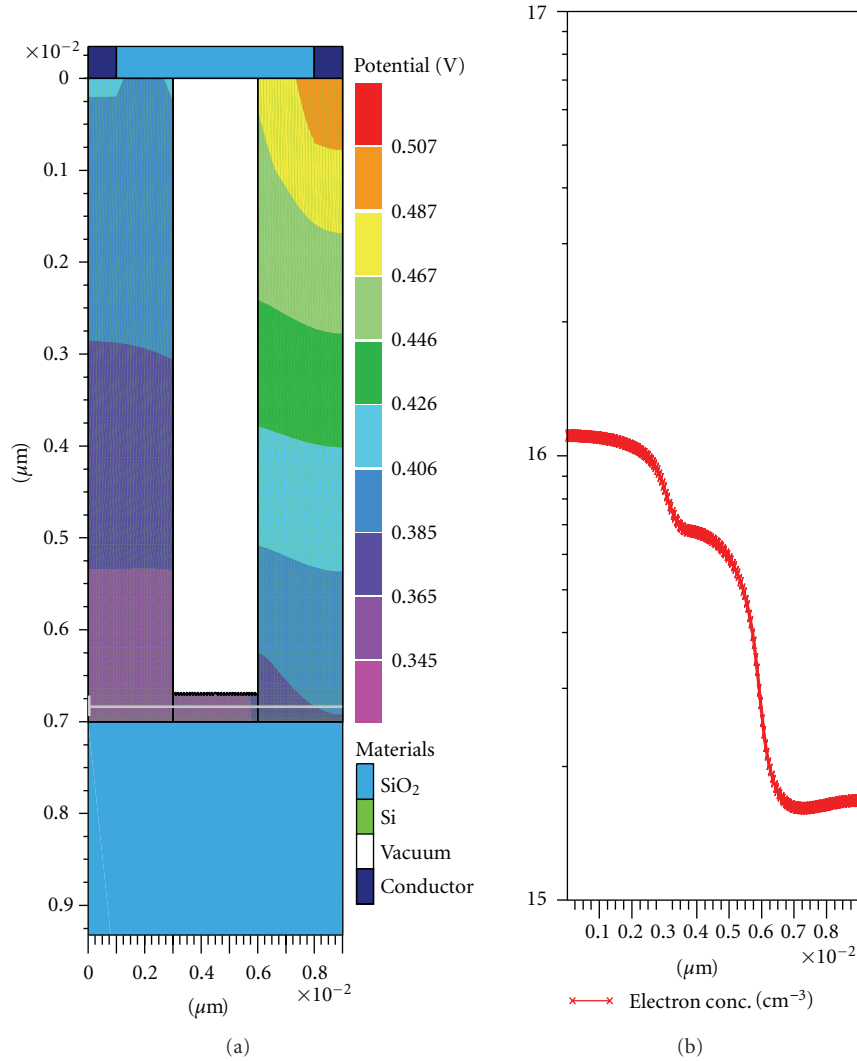


FIGURE 14: The potential and the electron concentration in the 0.3 nm structure.

The DC analysis used the following voltages:  $V_G = 3 \text{ V}$ ,  $V_D = 0.1 \text{ V}$ ,  $V_S = 0 \text{ V}$ . The nanoeffects were simulated taking into account the Fowler-Nordheim tunneling and the Fermi distribution, using in the MODEL statement the following parameters: FNORD, FERMI: models conmob srh auger fermi fldmob fnord print, meaning: constant mobility, Shockley-Read-Hall and Auger recombination model and mobility attenuation with lateral field. For electron concentration study in the inversion channel, the drain voltage was maintained at 0.1V and the gate voltage was increased from 0V to +3V with a 0.05V step. Despite of the very thin p film, a high electron concentration occurs in the channel at  $V_{GS} = +3 \text{ V}$ , as is shown in Figure 15. With  $V_{DS}$  increasing, the current arise as a superposition, when the source-drain vacuum is tunneled.

However, the device is in strong inversion at this gate voltage, because  $n_{\text{channel}} = 2 \times 10^{20} \text{ cm}^{-3} > 5 \times 10^{15} \text{ cm}^{-3} = N_{A-\text{film}}$ . The electron concentration in the 0.3 nm p-type SOI film is:  $n_{\text{channel}} = 2 \times 10^{20} \text{ cm}^{-3} = 0.2 \text{ nm}^{-3} \approx 1$  electron

per channel volume,  $V$ , Figure 16. The channel volume is  $V = 0.3 \text{ nm} \times 3 \text{ nm} \times 6 \text{ nm} = 5.4 \text{ nm}^3$ . Then, the electrons transport, from source to drain, is one by one. Therefore, the SET principle is satisfied.

## 7. Conclusions

This paper presented a nanotransistor with silicon on insulator structure in different situations. When the film thickness varied between 200 nm to 10 nm the electrical characteristics preserve the classical shape. When the film thickness varied from 1 nm to 0.3 nm and a cavity occurs above the film, the device presents atypical electrical characteristics  $I_D-V_{GS}$ , having a maximum like the SET transistor. The shape of the  $I_D-V_{DS}$  curves with a minimum proves the presence of the tunnel effect. The electron transport in the p-film is one by one, proving the Single Electron Technology for our proposed SOI nanotransistor.

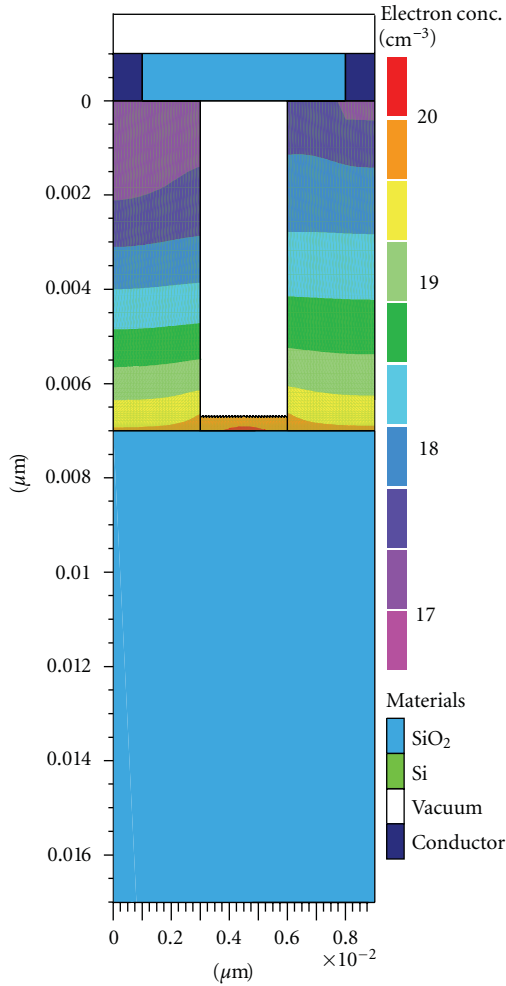


FIGURE 15: The electron concentrations in 0.3 nm SET: global.

Also, the new model with distribution presented in this paper, improves the flat-band voltage modeling of the SOI nanostructures, introducing new fitting parameters:  $\Delta t_{1,2}$ —the spreading coefficients. However, neither the presence or absence of the interface charge  $Q_{I1,2}$  is defining for the atypical shape of the transfer characteristics, because the curves with maximum arose both in rectangular SOI film with  $Q_{I2}$  both in “U” shape SOI film without  $Q_{I2}$ ; the only conditions was to exist a ultra-thin SOI film under 2 nm.

The simulations revealed that the SOI nanotransistor with a thinner film in the channel body represents a solution for the SET’s implementation, with possible applications in industry like digital ULSI, invertors with SET, memories with SEM-single electron memory, and communications cells [24].

These simulations and the model with the distribution represent an important chapter in the devices design—a key stage during the industrial manufacturing.

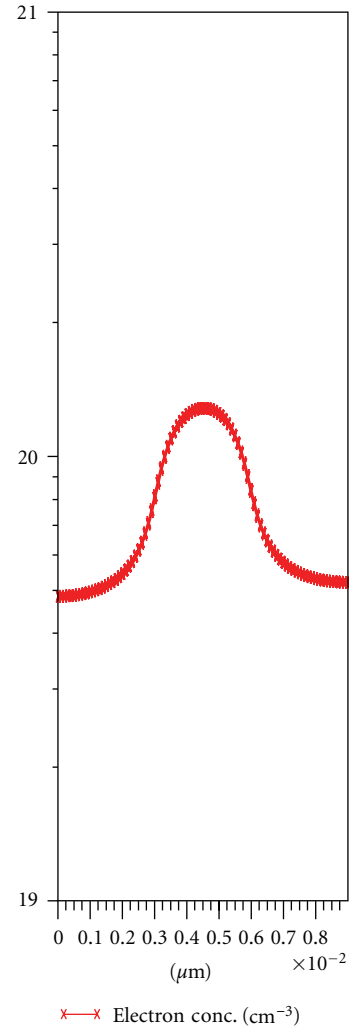


FIGURE 16: The electron concentrations in the 1 nm transistor—a detail in a cross-section.

## Acknowledgment

The work has been cofunded by the Sectorial Operational Program Human Resources Development of the Romanian Ministry of Labor, Family, and Social Protection through the Financial Agreement nos. POSDRU/89/1.5/S/62557 and PNII-62063-12095.

## References

- [1] H. Murray, P. Martin, and S. Bardy, “Taylor expansion of surface potential in MOSFET: application to Pao-Sah integral,” *Active and Passive Electronic Components*, vol. 2010, Article ID 268431, 11 pages, 2010.
- [2] S. A. Mahmoud, S. M. Al-Shomar, and A. A. Akl, “Electrical characteristics and nanocrystalline formation of sprayed iridium oxide thin films,” *Advances in Condensed Matter Physics*, vol. 2010, Article ID 518209, 6 pages, 2010.
- [3] J. Pretet, S. Monfray, S. Cristoloveanu, and T. Skotnicki, “Silicon-on-nothing MOSFETs: performance, short-channel

- effects, and backgate coupling,” *IEEE Transactions on Electron Devices*, vol. 51, no. 2, pp. 240–245, 2004.
- [4] D. N. Vizireanu, “Quantized sine signals estimation algorithm for portable DSP based instrumentation,” *International Journal of Electronics, Taylor & Francis*, vol. 96, no. 11, pp. 1175–1181, 2009.
- [5] N. Quijano and K. M. Passino, “The ideal free distribution: theory and engineering application,” *IEEE Transactions on Systems, Man and Cybernetics, Part B*, vol. 37, no. 1, pp. 154–165, 2007.
- [6] A. A. J. Al-Douri, M. F. A. Alias, A. A. Alnajjar, and M. N. Makadsi, “Electrical and optical properties of  $\text{Ge}_x\text{Si}_{1-x}:\text{H}$  thin films prepared by thermal evaporation method,” *Advances in Condensed Matter Physics*, vol. 2010, Article ID 428739, 8 pages, 2010.
- [7] J. Benson, N. V. D’Halleweyn, W. Redman-White et al., “A physically based relation between extracted threshold voltage and surface potential flat-band voltage for MOSFET compact modeling,” *IEEE Transactions on Electron Devices*, vol. 48, no. 5, pp. 1019–1021, 2001.
- [8] C. Ravariu, A. Rusu, F. Babarada, and F. Ravariu, “Discrepancies of the flat-band voltage models revealed by simulations in sub-50 nm SOI films,” in *Proceedings of the 15th IASTED International Conference on Applied Simulation and Modelling (ASM ’06)*, pp. 141–144, Rhodes, Greece, June 2006.
- [9] C. Ravariu, A. Rusu, M. D. Profirescu, and F. Ravariu, “A nano-transistor with a cavity,” in *Proceedings of the 8th IEEE International Conference on Nanotechnology*, vol. 1, chapter 4, pp. 111–114, Anaheim, Calif, USA, 2005.
- [10] S. Sato, K. Komiya, N. Bresson, Y. Omura, and S. Cristoloveanu, “Possible influence of the Schottky contacts on the characteristics of ultrathin SOI pseudo-MOS transistors,” *IEEE Transactions on Electron Devices*, vol. 52, no. 8, p. 1807, 2005.
- [11] C. Ravariu, A. Rusu, F. Ravariu, D. Dobrescu, and L. Dobrescu, “Alternative methods of parameters extraction based on the pseudo-MOS technique,” in *Proceedings of the 24th IEEE International Conference on Microelectronics (MIEL ’04)*, pp. 249–252, Nis, Serbia, 2004.
- [12] C. Ravariu, A. Rusu, F. Udrea, and F. Ravariu, “Simulation results of some diamond on insulator nano-MISFETs,” *Diamond and Related Materials*, vol. 15, no. 2, pp. 777–782, 2006.
- [13] C. Ravariu, F. Babarada, A. Rusu, and F. Ravariu, “More accurate models of the interfaces oxide ultra-thin SOI films,” *AIP Conference Proceedings*, vol. 893, pp. 3–4, 2007, ISI electronic Journal, under the American Institute of Physics AIP auspices.
- [14] O. Stanasila, *Special Mathematics*, ALL Publishing, Bucharest, Romania, 2001.
- [15] G. A. Brown, H. H. Hosack, K. Joyner, and W. A. Krull, “Integrity of gate oxides formed on SIMOX wafers,” in *Proceedings of the IEEE International SOI Conference*, p. 73, October 1994.
- [16] “CEA-Leti makes a R&D 20 nm fully depleted SOI process,” *EUROSOI Newsletter*, vol. XXVI, October 2010.
- [17] C. Ravariu, A. Rusu, and F. Ravariu, “Parameters extraction from some experimental static characteristics of a pseudo-MOS transistor,” *Scientific Bulletin Journal Series C*, vol. 70, no. 1, pp. 29–34, 2008.
- [18] D. N. Vizireanu, “A simple and precise real-time four point single sinusoid signals instantaneous frequency estimation method for portable DSP based instrumentation,” *Measurement*, vol. 44, no. 2, pp. 500–502, 2011.
- [19] S. Mahapatra, A. M. Ionescu, and B. Banerjee, “A quasi-analytical SET model for few electron circuit simulation,” *IEEE Electron Device Letters*, vol. 23, no. 6, pp. 366–368, 2002.
- [20] S. M. Rezaul Hasan, “Transition frequencies and negative resistance of inductively terminated CMOS buffer cell and application in MMW LC VCO,” *Active and Passive Electronic Components*, vol. 2010, Article ID 542406, 11 pages, 2010.
- [21] C. Ravariu, A. Rusu, A. Bondarciuc et al., “Modeling and simulation of a nanostructure for a single electron technology implementation,” in *Proceedings of the 5th International Mediterranean Modelling Multiconference*, pp. 312–315, Braticco, Italy, September 2008.
- [22] C. J. Singh, K. C. Kumar, S. Gope, J. Basu, S. Sarkar, and S. Kumar, “Single electron device based automatic tea vending machine,” in *Proceedings of the IET-UK International Conference on Information and Communication Technology in Electrical Sciences (ICTES ’07)*, pp. 891–896, Chennai, Tamilnadu, India, December 2007.
- [23] H. Inokawa, Y. Takahashi, K. Degawa, T. Aoki, and T. Higuchi, “A single-electron-transistor logic gate family and its application—part II: design and simulation of a 7-3 parallel counter with linear summation and multiple-valued latch functions,” in *Proceedings of the 34th International Symposium on Multiple-Values Logic (ISMVL ’04)*, pp. 269–274, 2004.
- [24] R. M. Udrea and D. N. Vizireanu, “Quantized multiple sinusoids signal estimation algorithm,” *Journal of Instrumentation*, vol. 3, article P02008, pp. 1–7, 2008.

## Research Article

# Poole-Frenkel Conduction in Cu/Nano-SnO<sub>2</sub>/Cu Arrangement

Hossein Mahmoudi Chenari,<sup>1</sup> Hassan Sedghi,<sup>2</sup> Mohammad Talebian,<sup>2</sup>  
Mir Maqsoud Golzan,<sup>2</sup> and Ali Hassanzadeh<sup>3</sup>

<sup>1</sup> Department of Physics, Faculty of Science, Maraghe University, Maraghe, Iran

<sup>2</sup> Department of Physics, Faculty of Science, Urmia University, Urmia, Iran

<sup>3</sup> Department of Chemistry, Faculty of Science, Urmia University, Urmia, Iran

Correspondence should be addressed to Hossein Mahmoudi Chenari, hmahmodiph@yahoo.com

Received 31 December 2010; Revised 6 May 2011; Accepted 23 May 2011

Academic Editor: Shaogang Hao

Copyright © 2011 Hossein Mahmoudi Chenari et al. This is an open access article distributed under the Creative Commons Attribution License, which permits unrestricted use, distribution, and reproduction in any medium, provided the original work is properly cited.

It is well known that metal/Tin-dioxide/metal sandwich structures exhibit a field-assisted lowering of the potential barrier between donor-like center and the conduction band edge, known as the Poole-Frenkel effect. This behavior is indicated by a linear dependence of  $\log J$  on  $V^{1/2}$ , where  $J$  is the current density, and  $V$  is the applied voltage. In this study, the electrical properties of Cu/nano-SnO<sub>2</sub>/Cu sandwich structures were investigated through current-voltage measurements at room temperature. Also, an attempt to explore the governing current flow mechanism was tried. Our results indicate that noticeable feature appearing clearly in the current-voltage characterization is the Poole-Frenkel and space-charge-limited conduction mechanisms.

## 1. Introduction

Nanocrystalline materials with average grain size of less than 50 nm have attracted considerable scientific interest because of their unusual physical and chemical properties [1]. The microstructure of nanocrystalline materials depends upon the method of preparation. Tin dioxide (SnO<sub>2</sub>), a wide band gap (3.6 eV) n-type semiconductor, is one of the most important materials for gas sensors [2]. It is well known for its application in gas sensors and dye-based solar cells [3]. Because of their relatively low operating temperature and as oxidizing gases, SnO<sub>2</sub> nanoparticles have been extremely studied [4]. As a transparent conducting oxide (TCO), it has been widely used as optoelectronic devices such as flat panel displays and thin film solar energy cells [5]. As an n-type semiconductor, tin dioxide has been actively explored as the functional component in detecting combustible gases such as CO, H<sub>2</sub>, and CH<sub>4</sub> [6]. Most of these studies concentrated on devices, which were fabricated with polycrystalline films as the sensing units [7]. Nanostructures of SnO<sub>2</sub> could also be employed to detect various gases [8, 9].

In some of these applications, the mechanism of electronic conduction strongly affects the device characteristics. Therefore, one needs to understand conduction mechanism.

The type of electronic conduction mechanism depends on several factors, in particular, the nature of the metallic contact to the semiconductor (either ohmic or blocking), the level of voltage applied across the sample, surface roughness, and grain size and its temperature. Metal-semiconductor (MS) structures (or Schottky diodes) have been studied extensively because of the very importance and critical components in integrated circuit technology. Moreover, it is a very attractive tool for the characterization of semiconductor materials [10–13].

In the present work, We examine the mechanisms, which control carrier transport in Cu/nano-SnO<sub>2</sub>/Cu sandwich structures. These include the study of gate voltage dependence of device leakage current.

## 2. Experimental Details

SnO<sub>2</sub> nanoparticles were synthesized by a simple sol-gel method which its details reported elsewhere [14]. SnO<sub>2</sub> nanopowder Pellets were made by applying a uniaxial pressure of 312.92 atmospheres on the powder sample. Polarization measurements were performed on the Cu/nano-SnO<sub>2</sub>/Cu sequence system using a computer-controlled AUTOLAB potentiostat and galvanostat.

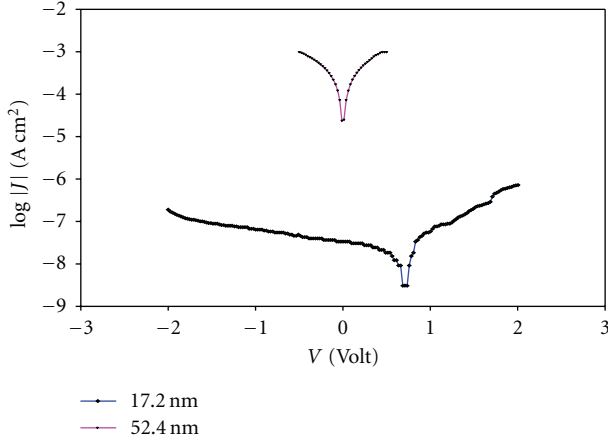


FIGURE 1:  $\log|J|$  versus  $V$  characteristic of nano-SnO<sub>2</sub> with different grain sizes.

### 3. Results and Discussion

**3.1. Polarization Study.** A typical forward bias semilogarithmic  $\log|J|$  versus  $V$  characteristic of Cu/nano-SnO<sub>2</sub>/Cu sandwich structures is shown in Figure 1. The leakage current can be affected by the surface roughness and grain size. The smaller grain size produces more grain boundaries and causes more leakage current [15]. Hence, it is suggested that the decrease of the leakage current of specimens can be attributed to the reduction of the surface roughness. The  $\log|J|$ - $V$  characteristics show also no double blocking behavior (see Figure 1). We assume that the copper electrode as a back contact does not block the current in reverse direction, which is especially the case for very low barriers. So the current transport through the Cu contact dominates the  $\log|J|$ - $V$  characteristic for positive voltages. Schottky emission, Poole-Frenkel, space-charge-limited conduction (SCLC), and so forth, are the possible conduction mechanisms in the studied junctions [16]. The governing conduction mechanism in Cu/nano-SnO<sub>2</sub>/Cu Schottky diodes at hand can be figured out from the power of  $\log|J|$ - $V$  curve. Power of the curve greater than 2 ( $m > 2$ ) indicates SCLC mechanism whereas being equal to 1 ( $m = 1$ ) imply ohmic character. When the power lies between 1 and 2 imposing either Schottky or Poole-Frenkel conduction mechanism. The linear sections of the curve could be interpreted in terms of either the Schottky emission or Poole-Frenkel emission. For the Schottky emission, the current density  $J$  is expressed as follows [17]:

$$J = A^* T^2 \exp\left(\frac{-\varphi}{kT}\right) \exp\left(\frac{e\beta_s V^{1/2}}{kTd^{1/2}}\right), \quad (1)$$

where  $A^*$  is the effective Richardson constant,  $\varphi$  is the Schottky barrier height at the electrode contact, and  $\beta_s$  is the Schottky field lowering constant. For Poole-Frenkel emission, the current density is given by

$$J = J_{pf0} \exp\left(\frac{\beta_{pf} V^{1/2} q}{kTd^{1/2}}\right), \quad (2)$$

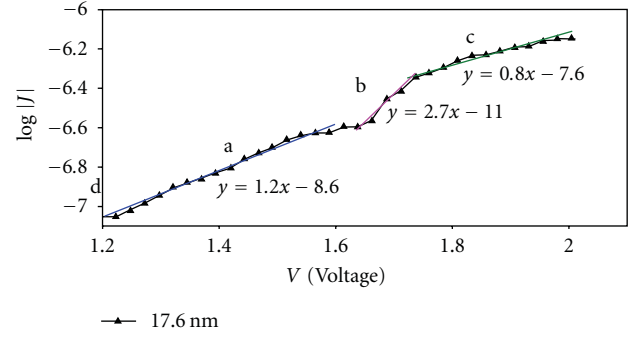


FIGURE 2: Forward bias  $\log|J|$ - $V$  plot of the Cu/nano-SnO<sub>2</sub>/Cu arrangement with a grain size of 17.6 nm.

where  $\beta_{pf}$  is the Poole-Frenkel coefficient. The theoretical values of these coefficients are given by

$$2\beta_s = \beta_{pf} = \left(\frac{e}{\pi\epsilon\epsilon_0}\right)^{1/2}. \quad (3)$$

For Schottky diodes, thermionic emission (TE) model suggests the following  $J$ - $V$  relationship:

$$J = J_0 \exp\left(\frac{eV}{n\kappa T}\right), \quad (4)$$

where  $V$ ,  $\kappa$ ,  $T$ ,  $n$  and  $J_0$  are the applied voltage, Boltzman constant, temperature, ideality factor, and saturation current density, respectively. The saturation current density is given by

$$J_0 = A^* T^2 \exp\left(-\frac{e\varphi_b}{\kappa T}\right), \quad (5)$$

where  $A^*$ ,  $\varphi_b$ , and  $e$  are the Richardson constant, barrier height, and electron charge, respectively. The parameters  $J_0$  and  $\varphi_b$  for SnO<sub>2</sub> nanoparticles with a grain size of 17.6 nm were calculated  $8.6472 \times 10^{-4}$  A and 0.6015 eV, and for SnO<sub>2</sub> nanoparticles with a grain size of 52.4 nm were obtained 0.0312 A and 0.5073 eV, respectively, using the above equations.

As shown in Figure 2, three linear regions are eventual in the  $\log|J|$ - $V$  characteristic of the Cu/nano-SnO<sub>2</sub>/Cu sandwich structure. One of them is in the lower-voltage region ( $1.2 < V < 1.6$ ), where the power is equal to 1.2, imposing either Schottky or Poole-Frenkel conduction mechanism. In the second region, with increasing voltage, more electrons injected from electrode into the film and current density originates from the SCLC mechanism, where the power is equal to 2.7. Abrupt increment of the current density is characteristic of the SCLC mechanism due to the trapped carriers. As the applied voltage is increased further, strong injection of electrons takes place and causes an increase in the density of filled trapping sites and leading to an increase of film conduction. An abrupt increase in leakage current appeared which follows a trap-filled limited law. For this conduction, the increasing slope indicates that the  $I$ - $V$  correlations are determined by another distributed trap type [18].

In the higher voltage region (Section 3), less slope is observable and the “quasisaturation” of the current may be

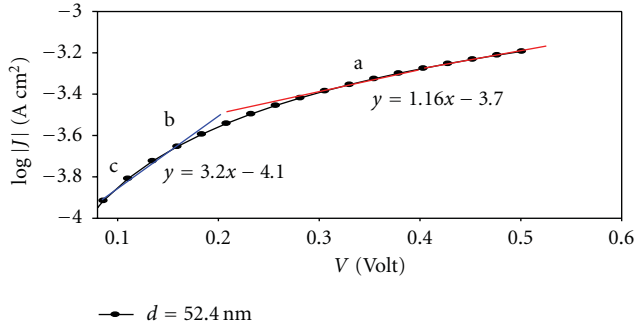


FIGURE 3: Forward bias  $\log |J|$ - $V$  plot of the Cu/nano-SnO<sub>2</sub>/Cu arrangement with a grain size of 52.4 nm.

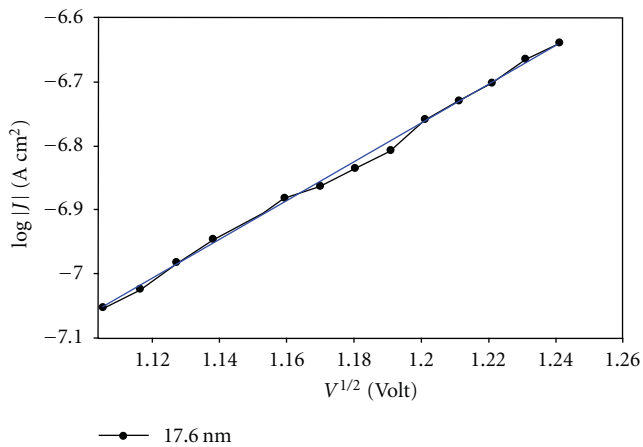


FIGURE 4: Log  $J$ - $V^{1/2}$  plot of the Cu/nano-SnO<sub>2</sub>/Cu arrangement with a grain size of 17.6 nm.

caused by the charge trapping. Consequently, an internal electric field is created, which is opposed to the external electric field, limiting the carriers flow. As can be seen in the Figure 3, similar analysis is carried out for nanostructure SnO<sub>2</sub> with a grain size of 52.4 nm.

The other possibility for the nonlinear  $J$ - $V$  characteristics is bulk-limited Poole-Frenkel emission. Figure 4 shows the plot of  $\ln |J|$  versus  $V^{1/2}$  for Cu/nano-SnO<sub>2</sub>/Cu arrangement with a grain size of 17.6 nm, which clearly yields a linear section of the curve, could be interpreted in terms of either Schottky emission or Pool-Frenkel emission. Corresponding experimental value of  $\beta$  calculated from the slope of the linear region of Figure 4 was found to be  $3.63 \times 10^{-5} \text{ eV m}^{1/2} \text{ V}^{-1/2}$ . The experimental value of  $\beta$  for SnO<sub>2</sub> nanoparticles with a grain size of 52.4 nm, derived from the slope of the linear section of Figure 5, was found to be  $3.42 \times 10^{-5} \text{ eV m}^{1/2} \text{ V}^{-1/2}$ . Theoretical values of  $\beta_s$  and  $\beta_{pf}$  were found to be  $1.88 \times 10^{-5} \text{ eV m}^{1/2} \text{ V}^{-1/2}$  and  $3.76 \times 10^{-5} \text{ eV m}^{1/2} \text{ V}^{-1/2}$ , respectively. Experimental value for  $\beta$  in the both nanoparticle is nearly agreement with the theoretically calculated value of  $\beta_{pf}$ . Hence, we can conclude that the conduction mechanism in our nanocrystalline film is controlled by the Poole-Frenkel effect and the Schottky effect is probably masked by the Poole-Frenkel emission from some

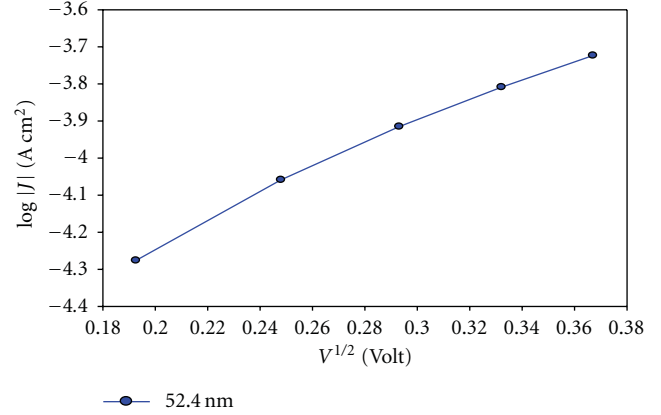


FIGURE 5: Log  $J$ - $V^{1/2}$  plot of the Cu/nano-SnO<sub>2</sub>/Cu arrangement with a grain size of 52.4 nm.

shallow traps at grain boundaries. The adsorbed oxygen atoms at the grain boundary produce defect states which trap carriers and create a potential barrier. By applying an applied field, the barrier height is diminished and electrons can flow from interfacial states, thus it can be reason of the existence of the Poole-Frenkel mechanism [19].

#### 4. Conclusion

The tetragonal tin dioxide nanoparticles were obtained by using sol-gel technique with thermal treatments. Possible mechanism for leakage current conduction in the Cu/nano-SnO<sub>2</sub>/Cu sequence system showed characteristics of typical Schottky-barrier devices. The Poole-Frenkel effect has been observed in nanotin oxide thick film. This effect depends on the electron transport phenomenon through grain boundaries. Nanostructured SnO<sub>2</sub> films with a large number of grain boundaries contain a considerable number of trap states.

#### References

- [1] H. Gleiter, "Nanocrystalline materials," *Progress in Materials Science*, vol. 33, no. 4, pp. 223–315, 1989.
- [2] M. R. Yang, S. Y. Chu, and R. C. Chang, "Synthesis and study of the SnO<sub>2</sub> nanowires growth," *Sensors and Actuators, B*, vol. 122, no. 1, pp. 269–273, 2007.
- [3] S. Ferrere, A. Zaban, and B. A. Gregg, "Dye sensitization of nanocrystalline tin oxide by perylene derivatives," *Journal of Physical Chemistry B*, vol. 101, no. 23, pp. 4490–4493, 1997.
- [4] A. R. Babar, S. S. Shinde, A. V. Moholkar, and K. Y. Rajpure, "Electrical and dielectric properties of co-precipitated nanocrystalline tin oxide," *Journal of Alloys and Compounds*, vol. 505, no. 2, pp. 743–749, 2010.
- [5] N. Amin, T. Isaka, A. Yamada, and M. Konagai, "Highly efficient 1  $\mu\text{m}$  thick CdTe solar cells with textured TCOs," *Solar Energy Materials and Solar Cells*, vol. 67, no. 1–4, pp. 195–201, 2001.
- [6] J. Kappler, A. Tomescu, N. Barsan, and V. Weimar, "CO consumption of Pd doped SnO<sub>2</sub> based sensors," *Thin Solid Films*, vol. 391, no. 2, pp. 186–191, 2001.

- [7] R. Scott, S. Yang, D. Williams, and G. Ozin, "Electronically addressable SnO<sub>2</sub> inverted opal gas sensors fabricated on interdigitated gold microelectrodes," *Chemical Communications*, no. 6, pp. 688–689, 2003.
- [8] A. Kolmakov, Y. Zhang, G. Cheng, and M. Moskovits, "Detection of CO and O<sub>2</sub> using tin oxide nanowire sensors," *Advanced Materials*, vol. 15, no. 12, pp. 997–1000, 2003.
- [9] A. Maiti, J. A. Rodriguez, M. Law, P. Kung, J. R. McKinney, and P. Yang, "SnO<sub>2</sub> nanoribbons as NO<sub>2</sub> sensors: insights from first principles calculations," *Nano Letters*, vol. 3, no. 8, pp. 1025–1028, 2003.
- [10] M. A. Cowley and M. S. Sze, "Surface states and barrier height of metal-semiconductor systems," *Journal of Applied Physics*, vol. 36, no. 10, pp. 3212–3220, 1965.
- [11] M. O. Nielsen, "Influence of semiconductor barrier tunneling on the current-voltage characteristics of tunnel metal-oxide-semiconductor diodes," *Journal of Applied Physics*, vol. 54, no. 10, pp. 5880–5886, 1983.
- [12] C. H. Card and H. E. Rhoderick, "Studies of tunnel MOS diodes I. Interface effects in silicon Schottky diodes," *Journal of Physics D*, vol. 4, no. 10, pp. 1589–1601, 1971.
- [13] A. Tataroglu and X. S. Altundal, "Characterization of current-voltage (I-V) and capacitance-voltage-frequency (C-V-f) features of Al/SiO<sub>2</sub>/p-Si (MIS) Schottky diodes," *Microelectronic Engineering*, vol. 83, no. 3, pp. 582–588, 2006.
- [14] A. Hassanzadeh, B. Moazzez, H. Haghgooie, M. Nasser, M. M. Golzan, and H. Sedghi, "Synthesis of SnO<sub>2</sub> nanopowders by a sol-gel process using propanol-isopropanol mixture," *The Central European Journal of Chemistry*, vol. 6, no. 4, pp. 651–656, 2008.
- [15] M. S. Tsai, S. C. Sun, and T. Y. Tseng, "Effect of oxygen to argon ratio on properties of (Ba,Sr)TiO<sub>3</sub> thin films prepared by radio-frequency magnetron sputtering," *Journal of Applied Physics*, vol. 82, no. 7, p. 3428, 1997.
- [16] M. S. Sze and K. K. Ng, *Physics of Semiconductor Devices*, John Wiley & Sons, Hoboken, NJ, USA, 2007.
- [17] A. Wilson and R. A. Collins, "Electrical characteristics of planar phthalocyanine thin film gas sensors," *Sensors and Actuators*, vol. 12, no. 4, pp. 389–403, 1987.
- [18] L. Zhang, J. Zhai, W. Mo, and X. Yao, "The dielectric and leakage current behavior of CoFe<sub>2</sub>O<sub>4</sub>-BaTiO<sub>3</sub> composite films prepared by combining method of sol-gel and electrophoretic deposition," *Solid State Sciences*, vol. 12, no. 4, pp. 509–514, 2010.
- [19] A. N. Banerjee, R. Maity, S. Kundoo, and K. K. Chattopadhyay, "Poole-Frenkel effect in nanocrystalline SnO<sub>2</sub>:F thin films prepared by a sol-gel dip-coating technique," *Physica Status Solidi A*, vol. 201, no. 5, pp. 983–989, 2004.

## Research Article

# Three Possible Encapsulation Mechanics of TiO<sub>2</sub> Nanoparticles into Single-Walled Carbon Nanotubes

Wisit Sukchom,<sup>1,2</sup> Kittisak Chayantrakom,<sup>1,2</sup>  
Pairote Satiracoo,<sup>1,2</sup> and Duangkamon Baowan<sup>1,2</sup>

<sup>1</sup>Department of Mathematics, Faculty of Science, Mahidol University, Rama 6 Road Bangkok 10400, Thailand

<sup>2</sup>Centre of Excellence in Mathematics, CHE, Si Ayutthaya Road Bangkok 10400, Thailand

Correspondence should be addressed to Duangkamon Baowan, scdbw@mahidol.ac.th

Received 7 February 2011; Accepted 3 May 2011

Academic Editor: Shaogang Hao

Copyright © 2011 Wisit Sukchom et al. This is an open access article distributed under the Creative Commons Attribution License, which permits unrestricted use, distribution, and reproduction in any medium, provided the original work is properly cited.

Titanium dioxide nanoparticle (TiO<sub>2</sub>-NP) is widely used in manufactured nanomaterials such as sunscreens, cosmetics, drugs, and some food products. It can be encapsulated in a single-walled carbon nanotube (SWNT) depending on their physical and chemical interactions. On applying the Lennard-Jones potential function and the continuous approximation, we determine three encapsulation mechanisms for spherical shape TiO<sub>2</sub>-NP entering a tube: (i) head-on at the tube open end, (ii) around the edge of the tube open end, and (iii) through a defect opening on the tube wall. The total potential energy of the system is obtained as an exact expression by performing double surface integrals. We find that the TiO<sub>2</sub>-NP is most (least) likely to be encapsulated into a SWNT by head-on configuration (around the edge of the tube open end). This encapsulation procedure is a potential application for targeted drug delivery. For convenience, throughout this analysis all configurations are assumed to be in vacuum and the TiO<sub>2</sub>-NP is initially at rest.

## 1. Introduction

The unique chemical, physical, and electronic properties of single-walled carbon nanotubes (SWNTs) provide the most promising avenue of research into the fabrication of nanoscale one-dimensional systems [1, 2]. Self-assembled molecules in the SWNT's hollow core are expected to exhibit new features differing from those of the bulk materials [3, 4]. "Peapods," SWNTs filled with fullerenes [5, 6], are already exciting interest with future developments hopefully leading to composite materials fulfilling particular electronic or mechanical functions. However, the formation mechanisms regarding nanopeapods are currently uncertain. Suggestions about their unique behaviour have focused on the van der Waals interaction and the large surface area to volume of nanoparticles.

Titanium dioxide (TiO<sub>2</sub>, titania) has been the subject of a number of studies in the fields of water and air purification, photocatalytic sterilisation of food and the environmental industry. The activity of TiO<sub>2</sub> against a wide variety of organisms, bacteria, algae, virus, and cancer cells, has been

reported. As a photocatalyst, the production of superoxide (O<sub>2</sub><sup>•-</sup>) and hydroxyl radicals (•OH) due to absorption of light with a wavelength less than 385 nm (ultraviolet A, UV-A) occurs. This is due to the generation of electron-hole pairs which migrate to the surface in combination with a competition of trapping and recombination events in the body of lattice [7, 8]. Most studies suggest that hydroxyl radicals, which are able to oxidise organic substances and disrupt bacteria and virus, are the main cause of the bactericidal effect during photocatalysis [9, 10]. TiO<sub>2</sub> has been well studied because of its low price and abundance, its stability and nontoxicity, as well as its high oxidative power. The major drawback of TiO<sub>2</sub> is that its band gap occurs in the near-UV of the electromagnetic spectrum.

Combining TiO<sub>2</sub> with carbon nanotube as hybrid materials offers many important potential applications. We comment that there are other types of nanoparticles, such as gold and magnetic Fe<sub>3</sub>O<sub>4</sub>, that can be used to study these three encapsulation mechanics, here the TiO<sub>2</sub> molecule is employed as an example, and once an analytic expression is obtained it can be adapted to the other systems. In this paper,

utilising a simple model based on algebraic calculations using the Lennard-Jones potential as the force field, we investigate the feasibility of encapsulating  $\text{TiO}_2$  in SWNT. The potential energy, force distribution, encapsulation energy, and consequent results for the assumed spherical  $\text{TiO}_2$  particles are presented. Further, we employ the continuous approach where the atoms at discrete locations on the molecules are smeared over surfaces of a spherical nanoparticle and a cylindrical SWNT, as a result some electronic properties, metallic and semiconducting, of nanotubes are neglected, and only the radius of the tube is taken into account. In this paper, we consider only the potential energy of the system where the electrostatic potential between two molecules will be included in authors' future work.

The paper is organised as follows; the potential function and the continuous approximation of  $\text{TiO}_2$ -SWNT systems are described in Section 2. In Section 3, we determine the three encapsulation mechanisms and their numerical results. Finally, conclusions are presented in Section 4. Using this model, we believe that many novel nanoscaled applications of these two particles will become apparent, possibly impacting on therapeutic research and the construction of nanoscale drug delivery systems.

## 2. Potential Energy and Force Distribution

The continuous approach has been utilised by many applicants to determine the interaction energy between two carbon nanostructures [11–17]. We have assumed that the carbon atoms on the nanotube and the titanium and oxygen on the  $\text{TiO}_2$  are uniformly distributed over the surfaces of the two molecules, so that the continuous approximation can be used. It is in a form of double surface integrals, averaged over the surfaces of each entity, and we may deduce

$$U = \eta_1 \eta_2 \iint \Phi(\rho) dS_1 dS_2, \quad (1)$$

where  $\eta_1$  and  $\eta_2$  are the mean atomic surface densities of  $\text{TiO}_2$  and carbon nanotube, respectively, and  $dS_1$  and  $dS_2$  are two surface elements.  $\Phi(\rho)$  is a potential function between two atoms on each molecule, and  $\rho$  is a distance between two surface elements. In this study, the well-known Lennard-Jones potential function [18] is employed which is given by

$$\Phi(\rho) = -\frac{A}{\rho^6} + \frac{B}{\rho^{12}}, \quad (2)$$

where  $A$  and  $B$  are the attractive and repulsive constants, respectively. The resultant axial force in the  $z$ -direction is calculated by differentiating the potential energy with respect to  $Z$ , so that the force is obtained by

$$F_Z = -\frac{\partial U}{\partial Z}, \quad (3)$$

where  $Z$  is the distance from the tube open end to the centre of the  $\text{TiO}_2$  molecule.

The suction energy or the encapsulation energy ( $W$ ) is defined as the total energy or work done generated by van

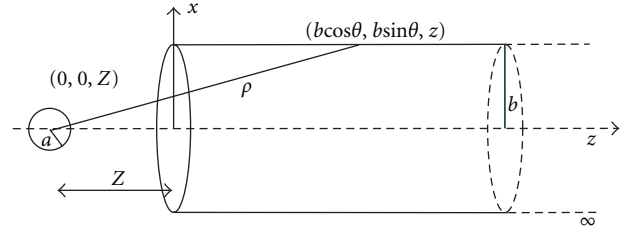


FIGURE 1:  $\text{TiO}_2$  encapsulated into a carbon nanotube head-on at the tube open end.

der Waals interaction acquired by a particular molecule as a consequence of being sucked into the nanotube [11], and it can be written as

$$W = \int_{-\infty}^{\infty} F(Z) dZ = - \int_{-\infty}^{\infty} \frac{dU}{dZ} dZ = U(-\infty) - U(\infty), \quad (4)$$

which is transformed into kinetic energy. We note that the particle begins to enter into the tube when the suction energy is equal to zero.

## 3. Three Possible Encapsulation Mechanics

**3.1. Encapsulation of  $\text{TiO}_2$  Head-On at the Tube Open End.** In this model, a  $\text{TiO}_2$  molecule is assumed to be a sphere. Firstly, the energy and the force distribution for the  $\text{TiO}_2$  molecule encapsulated into a single-walled carbon nanotube by entering the tube head-on at the tube open end are determined. After that, the maximum interaction energy can be determined by optimising the value of nanotube radius using the suction energy. This system is shown in Figure 1.

With reference to a rectangular Cartesian coordinate system  $(x, y, z)$  with origin located at the tube end, a typical point on the surface of the tube has the coordinates  $(b \cos \theta, b \sin \theta, z)$  where  $b$  is the radius of the semi-infinite tube. Similarly, with reference to the same rectangular Cartesian coordinate system  $(x, y, z)$ , the centre of the  $\text{TiO}_2$  molecule has coordinates  $(0, 0, Z)$  where  $Z$  is the distance from the tube end to the centre of the  $\text{TiO}_2$  molecule in the  $z$ -direction which can be either positive or negative. The radius of the spherical  $\text{TiO}_2$  molecule is denoted by  $a$ . Thus the distance  $\rho$  between the centre of the  $\text{TiO}_2$  and a typical point on the tube is given by

$$\rho^2 = b^2 + (z - Z)^2. \quad (5)$$

Firstly, we determine the interaction energy between a point and a spherical  $\text{TiO}_2$  which is given by

$$U^*(\rho) = \frac{\pi a \eta_1}{\rho} \left[ \frac{A}{2} \left( \frac{1}{(\rho + a)^4} - \frac{1}{(\rho - a)^4} \right) - \frac{B}{5} \left( \frac{1}{(\rho + a)^{10}} - \frac{1}{(\rho - a)^{10}} \right) \right], \quad (6)$$

where  $\eta_1$  denotes the mean surface density of  $\text{TiO}_2$  molecule. We note that the derivation for the above equation can be found in [11].

Using the Lennard-Jones potential function and the continuous approximation for a cylindrical carbon nanotube, the total potential energy can be obtained and it can be written as

$$U = \pi ab\eta_1\eta_2 \times \int_{-\pi}^{\pi} \int_0^{\infty} \frac{1}{\rho} \left[ \frac{A}{2} \left( \frac{1}{(\rho+a)^4} - \frac{1}{(\rho-a)^4} \right) - \frac{B}{5} \left( \frac{1}{(\rho+a)^{10}} - \frac{1}{(\rho-a)^{10}} \right) \right] dzd\theta, \quad (7)$$

where  $\eta_2$  represents the mean atomic surface density of carbon nanotube. The mean atomic surface density of TiO<sub>2</sub> is calculated from a single unit cell of the anatase structure, which is the most common mineral form of TiO<sub>2</sub> whereas the others are rutile and brookite. It is a tetragonal configuration with two TiO<sub>2</sub> units per a primitive cell and we may deduce  $\eta_1 = 0.07498 \text{ \AA}^{-2}$  [19]. In the case of a carbon nanotube, it can be thought as a graphene sheet rolled up to form a cylinder, therefore we can simplify the mean atomic surface density of the tube from the graphene sheet, and we may deduce  $\eta_2 = 0.3812 \text{ \AA}^{-2}$ . Moreover, (7) can be rewritten as

$$U = 4\pi a^2 b \eta_1 \eta_2 \times \int_{-\pi}^{\pi} \int_0^{\infty} \left[ -A \left( \frac{1}{(\rho^2 - a^2)^3} + \frac{2a^2}{(\rho^2 - a^2)^4} \right) + \frac{B}{5} \left( \frac{5}{(\rho^2 - a^2)^6} + \frac{80a^2}{(\rho^2 - a^2)^7} + \frac{336a^4}{(\rho^2 - a^2)^8} + \frac{512a^6}{(\rho^2 - a^2)^9} + \frac{256a^8}{(\rho^2 - a^2)^{10}} \right) \right] dzd\theta. \quad (8)$$

There is one form of the integral which needs to be evaluated, and it is defined by

$$G_n = \int_{-\pi}^{\pi} \int_0^{\infty} \frac{1}{(\rho^2 - a^2)^n} dzd\theta. \quad (9)$$

The derivation for  $G_n$  can be found in Baowan et al. [16], where we may deduce

$$G_n = \frac{2\pi}{(b^2 - a^2)^{n-1/2}} \int_{-\tan^{-1}[Z/(b^2 - a^2)]}^{\pi/2} \cos^{2(n-1)} \psi d\psi \quad (10)$$

and

$$\int \cos^{2(n-1)} \psi d\psi = \frac{1}{2^{2(n-1)}} \left[ \binom{2(n-1)}{(n-1)} \psi + \sum_{k=0}^{n-2} \binom{2(n-1)}{k} \frac{\sin[(2n-2k-2)\psi]}{(n-k-1)} \right], \quad (11)$$

TABLE 1: Lennard-Jones constants used in this model.

Interaction	$\epsilon$ (meV)	$\sigma$ (Å)	$A$ (eV $\times$ Å <sup>6</sup> )	$B$ (eV $\times$ Å <sup>12</sup> )
C-Ti	3.14	3.7588	35.38	9979.40
C-O	4.14	3.2531	19.61	23241.81
Graphene-Graphene	3.83	2.39	15.2	24100

where  $\binom{n}{m}$  is the binomial coefficient. By evaluating (11) at  $\psi = \pi/2$  and  $\psi = -\tan^{-1}[Z/(b^2 - a^2)]$  an analytical expression for  $G_n$  may be obtained.

For the interaction between the TiO<sub>2</sub> molecule and the carbon nanotube, there are two different interactions which are C-Ti and C-O interactions. By their atomic proportion, the total potential energy can be determined as

$$U^{\text{Tot}} = \frac{1}{3} U(A_{\text{C-Ti}}, B_{\text{C-Ti}}) + \frac{2}{3} U(A_{\text{C-O}}, B_{\text{C-O}}). \quad (12)$$

The Lennard-Jones constants  $A$  and  $B$  for this system are given in Table 1 while the constants for C, Ti, and O are taken from the work of Mayo et al. [20] and the constants for graphene are taken from the work of Girifalco et al. [21].

The potential energy of the system depends on the distances in the  $z$ -directions. We illustrate graphically an example of the potential energy versus the distance  $Z$  for encapsulating a TiO<sub>2</sub> molecule with radius  $a = 10 \text{ \AA}$  into carbon nanotubes with radii  $b = 12.7$  and  $13.5 \text{ \AA}$ . In fact, the TiO<sub>2</sub> molecule will enter into the tube if the energy level inside the tube is lower than that outside the tube. From Figure 2(a), it is clearly seen that the TiO<sub>2</sub> will be encapsulated into the tube with radius  $13.5 \text{ \AA}$ . However, this phenomenon will not occur for the tube with radius  $12.7 \text{ \AA}$ . In the sense of force distribution as shown in Figure 2(b), the TiO<sub>2</sub> will enter into the tube if the force is positive which is in agreement with the result from energy behaviour.

The relation between the suction energy and the radius of nanotube  $b$  is shown in Figure 3 with three different values of TiO<sub>2</sub> radii  $a$ . For the case of  $a = 10 \text{ \AA}$ , the suction energy is zero when  $b = b_0 = 12.7875 \text{ \AA}$  which is the tube radius at which the TiO<sub>2</sub> molecule begins to enter into the tube and the encapsulation process occurs when  $b > b_0$ . The maximum suction energy is  $3.4187 \text{ eV}$ , it occurs when the tube radius  $b = 13.3039 \text{ \AA}$  which gives the radius difference as  $b - a = 3.3039 \text{ \AA}$ . These values are similar to those in the work of Baowan et al. [17].

Further, we observe similar behaviours for the cases of  $a = 12$  and  $a = 14 \text{ \AA}$  as illustrated in Figure 3. The maximum suction occurs at  $b = 15.2994$  and  $17.3024 \text{ \AA}$  for  $a = 12$  and  $14 \text{ \AA}$ , respectively, with corresponding to  $b - a = 3.2994$  and  $3.3024 \text{ \AA}$ . Therefore, we may conclude that the maximum suction energy is insensitive to the variation of their radii, and it depends on the different of their radii. However, the change of the TiO<sub>2</sub> length has an effect on the third and fourth decimal places of this value,  $b - a$ .

**3.2. Encapsulation of TiO<sub>2</sub> around the Edge of an Open End.** In this model, the energy and the force distributions for a TiO<sub>2</sub> molecule encapsulated into a single-walled carbon nanotube by entering the tube around the edge of an open

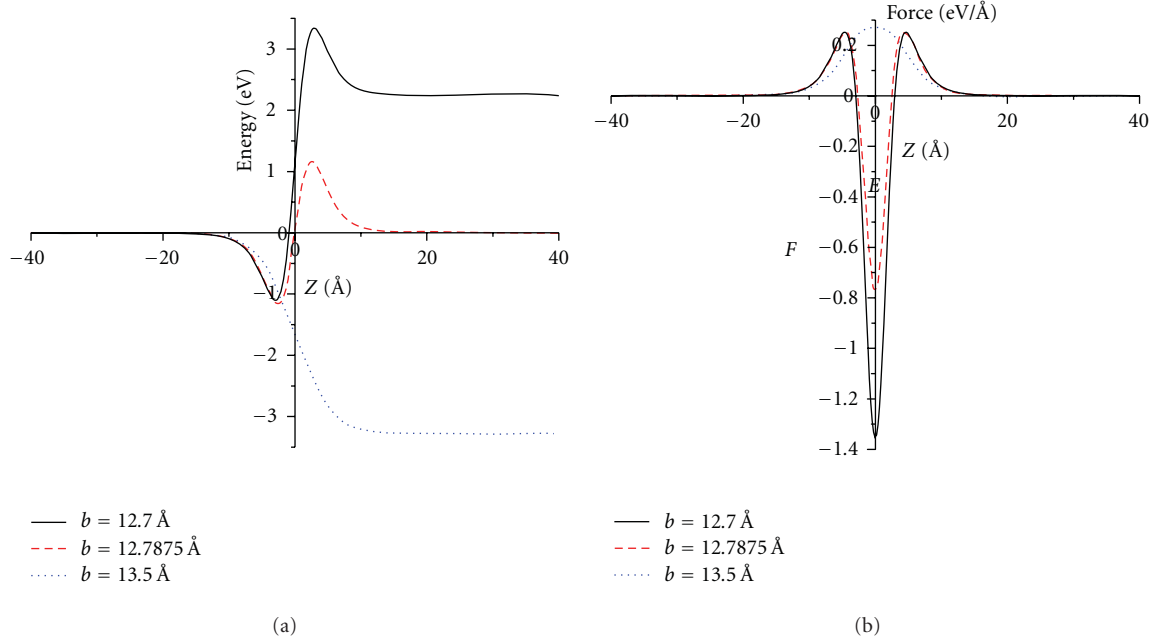


FIGURE 2: (a) Potential energy and (b) force distributions for  $\text{TiO}_2$  with radius  $a = 10 \text{ \AA}$  encapsulated into a carbon nanotube head-on at the tube open end.

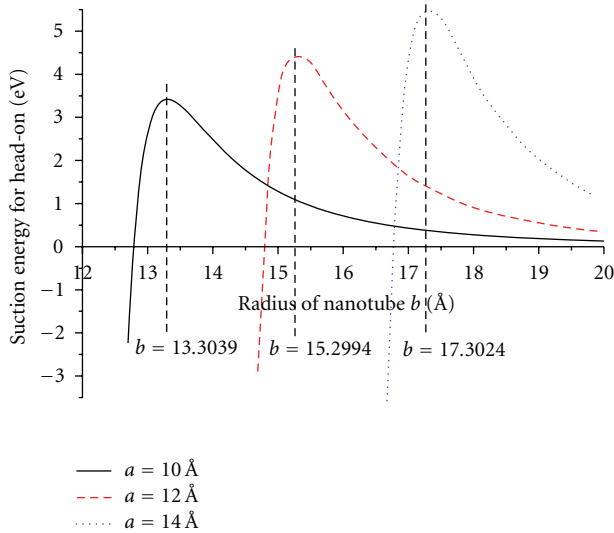


FIGURE 3: Suction energy for head-on configuration with three different nanoparticle radii  $a = 10, 12, 14 \text{ \AA}$ .

end are investigated. A schematic of this system is shown in Figure 4.

Again, with reference to a rectangular Cartesian coordinate system  $(x, y, z)$  with origin located at the tube end, a typical point on the surface of the tube has the coordinates  $(b \cos \theta, b \sin \theta, z)$  where  $b$  is the radius of the semi-infinite tube. Similarly, with reference to the same rectangular Cartesian coordinate system  $(x, y, z)$ , the centre of the  $\text{TiO}_2$  molecule has coordinates  $(x, 0, Z)$  where  $Z$  is the distance in the  $z$ -direction which can be either positive or negative and  $x$  is the distance of the  $\text{TiO}_2$  molecule in the  $x$ -direction. Thus

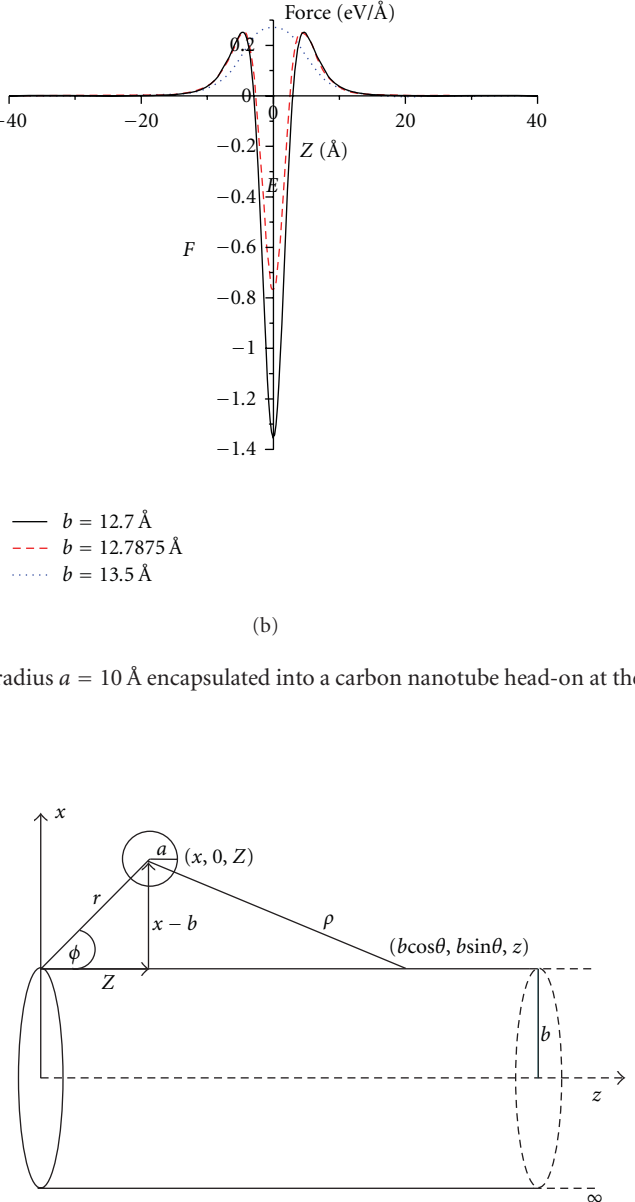


FIGURE 4:  $\text{TiO}_2$  encapsulated into a carbon nanotube around the edge of the tube open end.

the distance  $\rho$  between the centre of the  $\text{TiO}_2$  molecule and a typical point on the tube is given by

$$\begin{aligned} \rho^2 &= (b \cos \theta - x)^2 + b^2 \sin^2 \theta + (z - Z)^2 \\ &= (b - x)^2 + 4bx \sin^2 \left( \frac{\theta}{2} \right) + (z - Z)^2. \end{aligned} \quad (13)$$

Using the Lennard-Jones potential function and the continuous approximation, the total potential energy can be written as (7) where  $\rho$  is given by (13). Furthermore, there is another

form of the integral which needs to be evaluated, where we define as

$$H_n = \int_{-\pi}^{\pi} \int_0^{\infty} \frac{1}{(\rho^2 - a^2)^n} dz d\theta. \quad (14)$$

We note that in the case of (14),  $\rho$  is a function of two variables which are  $Z$  and  $x$ . Further, an analytical expression for (14) consists of three parts in terms of the standard hypergeometric function, which are presented in the work of Baowan et al. [16].

In Figure 5(a), we illustrate graphically an example of the potential energy versus the distances  $x$  and  $Z$  for encapsulating the  $\text{TiO}_2$  molecule with radius  $a = 10 \text{ \AA}$  into carbon nanotubes with radii  $b = 12.7$  and  $13.5 \text{ \AA}$ . Firstly, we consider the potential energy level, it is obvious that the potential energy is higher than in the former case so that in this case the  $\text{TiO}_2$  molecule has less likely chance to encapsulate in the carbon nanotube.

In the case of  $b = 12.7 \text{ \AA}$  as shown in Figure 5(a), the suction energy is zero when  $x = x_0 = 25.2267 \text{ \AA}$  and we obtain  $\Delta x_0 = b - x_0 = 2.5267 \text{ \AA}$ . The maximum suction energy,  $0.39501 \text{ eV}$ , occurs at  $x = 25.7284 \text{ \AA}$  which gives  $\Delta x_{\max} = 3.0284 \text{ \AA}$ , and the  $\text{TiO}_2$  molecule will not be sucked into the carbon nanotube if the distance  $x$  is greater than  $45.2398 \text{ \AA}$ . We note that the distance  $x$  has to be greater than  $a + b$  for the  $\text{TiO}_2$  molecule to be located above outside the tube.

Similarly for  $b = 13.5 \text{ \AA}$  as shown in Figure 5(b), the suction energy is zero when  $x = x_0 = 26.0270 \text{ \AA}$ . Moreover, we obtain  $\Delta x_0 = 2.5270 \text{ \AA}$  which is the distance in the  $x$  direction between the surface of the  $\text{TiO}_2$  molecule and the tube wall. The maximum suction energy,  $0.40058 \text{ eV}$ , occurs at  $x = 26.5288 \text{ \AA}$  which gives  $\Delta x_{\max} = 3.0288 \text{ \AA}$ . If the distance  $x$  is greater than  $46.1589 \text{ \AA}$ , the  $\text{TiO}_2$  molecule will not be sucked into the carbon nanotube since the global minimum energy is located farther along the tube in the positive  $z$ -direction.

Next, we consider only the positive  $z$ -direction where the  $\text{TiO}_2$  molecule is located above the tube. In this case, the  $\text{TiO}_2$  will not be encapsulated into the tube if its position is far away from the tube open end. The reason is that the energy at this point is lower than the energy barrier near the tube end. However, a nanopeapod can be formed if we give an initial energy to the  $\text{TiO}_2$  molecule to be greater than the energy barrier. Moreover, if the  $\text{TiO}_2$  molecule is initiated at rest closer to the tube open end, it has a higher probability of being encapsulated around the tube edge.

**3.3. Encapsulation of  $\text{TiO}_2$  at a Defect Opening on the Tube Wall.** In this model, we investigate the potential energy for a  $\text{TiO}_2$  molecule encapsulated into a carbon nanotube at a defect opening on the tube wall, where the centre of  $\text{TiO}_2$  is located midway along the tube length. Since the Lennard-Jones potential is only effective at short range, the carbon nanotube is assumed to be infinite in length. The total potential energy of this case is calculated by subtracting the total energy of the  $\text{TiO}_2$  interacting with the defect pad from

the total potential energy of the  $\text{TiO}_2$  interacting with the infinite nanotube, as shown in Figure 6.

Again, with reference to a rectangular Cartesian coordinate system  $(x, y, z)$  with origin located at the centre of the tube, a typical point on the surface of the tube has the coordinates  $(b \cos \theta, b \sin \theta, z)$  where  $b$  is the radius of the infinite tube. Similarly, with reference to the same rectangular Cartesian coordinate system  $(x, y, z)$ , the centre of the  $\text{TiO}_2$  molecule has coordinates  $(x, 0, Z)$  where  $Z$  is the distance in the  $z$ -direction which can be either positive or negative and  $x$  is the distance of the  $\text{TiO}_2$  molecule in the  $x$ -direction. Thus the distance  $\rho$  between the centre of the  $\text{TiO}_2$  and a typical point on the tube is given by

$$\begin{aligned} \rho^2 &= (b \cos \theta - x)^2 + b^2 \sin^2 \theta + (z - Z)^2 \\ &= (b - x)^2 + 4bx \sin^2 \left( \frac{\theta}{2} \right) + (z - Z)^2. \end{aligned} \quad (15)$$

On letting

$$\begin{aligned} \Phi^*(\rho) &= \frac{1}{\rho} \left[ \frac{A}{2} \left( \frac{1}{(\rho + a)^4} - \frac{1}{(\rho - a)^4} \right) \right. \\ &\quad \left. - \frac{B}{5} \left( \frac{1}{(\rho + a)^{10}} - \frac{1}{(\rho - a)^{10}} \right) \right], \end{aligned} \quad (16)$$

the total potential energy of the  $\text{TiO}_2$  interacting with the infinite nanotube is given by

$$U_{\text{tube}} = \pi ab \eta_1 \eta_2 \int_{-\pi}^{\pi} \int_{-\infty}^{\infty} \Phi^*(\rho) dz d\theta. \quad (17)$$

The defect pad is assumed to be in the region where  $Z \in (-L, L)$  and  $\theta \in (-\theta_0, \theta_0)$  so that the total energy of the  $\text{TiO}_2$  interacting with the defect pad is given by

$$U_{\text{pad}} = \pi ab \eta_1 \eta_2 \int_{-\theta_0}^{\theta_0} \int_{-L}^L \Phi^*(\rho) dz d\theta. \quad (18)$$

The defect pad is arbitrarily chosen as a square with the length  $L$ , which is determined from the summation of the radius  $a$  of the  $\text{TiO}_2$  and the equilibrium interspacing between the  $\text{TiO}_2$  and the nanotube which is  $3.304 \text{ \AA}$  [17]. Utilising the arc length formula  $S = r\theta$  where  $S$  is the arc length,  $r$  is the radius of the circle, and  $\theta$  is the angle in radians made by the arc at the centre of the circle, the limit of the integration,  $\theta_0$ , is adopted to be settled from  $L = b\theta_0$ . Note that there is only a minor effect on the energy profile when we vary  $\theta_0$ , and the overall properties of the system remain the same when  $L$  is greater than the critical value  $13.304 \text{ \AA}$ .

Thus the total potential energy for the  $\text{TiO}_2$  encapsulated in the carbon nanotube at the defect opening on the tube wall is obtained by

$$\begin{aligned} U &= \pi ab \eta_1 \eta_2 \left( \int_{-\pi}^{\pi} \int_{-\infty}^{\infty} \Phi^*(\rho) dz d\theta \right. \\ &\quad \left. - \int_{-\theta_0}^{\theta_0} \int_{-L}^L \Phi^*(\rho) dz d\theta \right). \end{aligned} \quad (19)$$

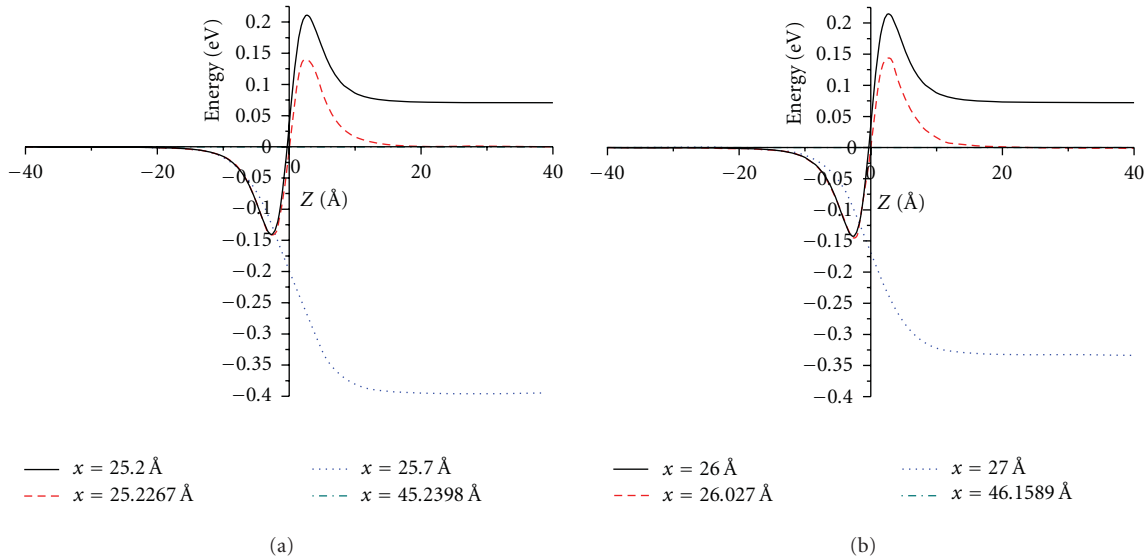


FIGURE 5: Potential energy for  $\text{TiO}_2$  with radius  $a = 10 \text{ \AA}$  encapsulated into carbon nanotubes with radius (a)  $b = 12.7 \text{ \AA}$  and (b)  $b = 13.5 \text{ \AA}$  around the edge of the tube open end where the distance  $x$  is fixed.

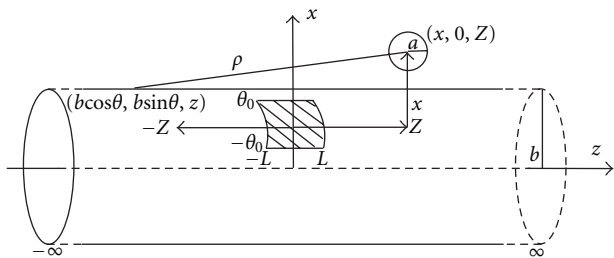


FIGURE 6:  $\text{TiO}_2$  encapsulated into a carbon nanotube at defect opening on the tube wall.

By using precisely the same analytical method as shown in the previous section, we separately determine the energy for the tube and that for the pad, and numerically calculate the total potential energy for the system.

We examine the relation between the potential energy and the distance  $Z$  for the different values of  $x$  which are the interspacing between the  $\text{TiO}_2$  molecule and the carbon nanotube surface. The behaviours of all cases are similar. Two examples of the potential energy versus the distances  $x$  and  $Z$  for encapsulating the  $\text{TiO}_2$  molecule with radius  $a = 10 \text{ \AA}$  into a carbon nanotube with radii  $b = 12.7$  and  $13.5 \text{ \AA}$  are shown in Figure 7. We consider the interaction energy at both edges of the defect pad because the point force singularity is affected from the edges and we get an approximate value at  $0.2 \text{ eV}$ . We observe that there are two potential energy peaks near the edges of the defect pad when  $x \leq 25.7288$  and  $x \leq 26.5288 \text{ \AA}$  for  $b = 12.7$  and  $13.5 \text{ \AA}$ , respectively. Therefore, an initial energy is required for the  $\text{TiO}_2$  molecule to be encapsulated into the carbon nanotube if the  $\text{TiO}_2$  molecule is located outside the region of the defect pad. However, the  $\text{TiO}_2$  is spontaneously sucked through the defect pad when its position is directly above the defect pad.

Furthermore, the  $\text{TiO}_2$  molecule will not be sucked through the defect pad to form a nanopapod if the value of  $x$  is greater than  $25.7288$  and  $26.5288 \text{ \AA}$  for  $b = 12.7$  and  $13.5 \text{ \AA}$ , respectively, because the position of the global minimum energy is located farther from the defect pad along the carbon nanotube in the  $z$ -direction.

## 4. Conclusions

In this paper, we investigate a nanopapod which is a well-known self-assembled hybrid carbon nanostructure comprising a  $\text{TiO}_2$  molecule and a carbon nanotube. We consider three encapsulation site scenarios for the  $\text{TiO}_2$  molecule entering the carbon nanotube which are (i) head-on at the tube open end, (ii) around the edge of the tube open end, and (iii) through a defect opening on the tube wall. The  $\text{TiO}_2$  is assumed to be initially at rest prior to enter into the two specific carbon nanotubes which are  $12.7 \text{ \AA}$  and  $13.5 \text{ \AA}$  in radius in a vacuum environment. We utilise the classical Lennard-Jones potential function and the continuous approximation to determine the potential energy which may be expressed in terms of the hypergeometric function. Because of the complicated analytical expressions, we use the algebraic computer package MAPLE to perform numerical evaluations.

In Figure 8, we compare the potential energy and encapsulation energy for the three encapsulation mechanisms. It is found that the  $\text{TiO}_2$  molecule is most likely to enter the carbon nanotube head-on at the tube open end. The reason is that the overall attractive force arises from the entire tube, and this mechanism avoids the point force singularity acting at the edge of the tube. Encapsulation at a defect pad is the second most likely mechanism to form the nanopapod. There is an effect from the edges of the defect pad but the  $\text{TiO}_2$  molecule is sucked into the tube if

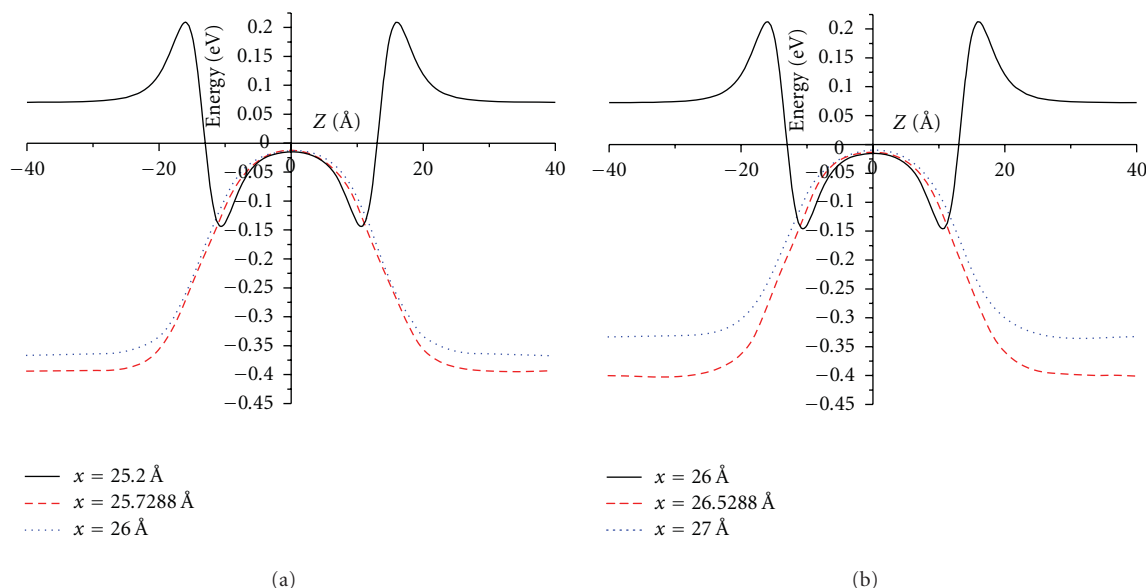


FIGURE 7: Potential energy for  $\text{TiO}_2$  with radius  $a = 10 \text{ \AA}$  encapsulated into a carbon nanotube with radius (a)  $b = 12.7 \text{ \AA}$  and (b)  $b = 13.5 \text{ \AA}$  at defect opening on the tube wall where the distance  $x$  is fixed.

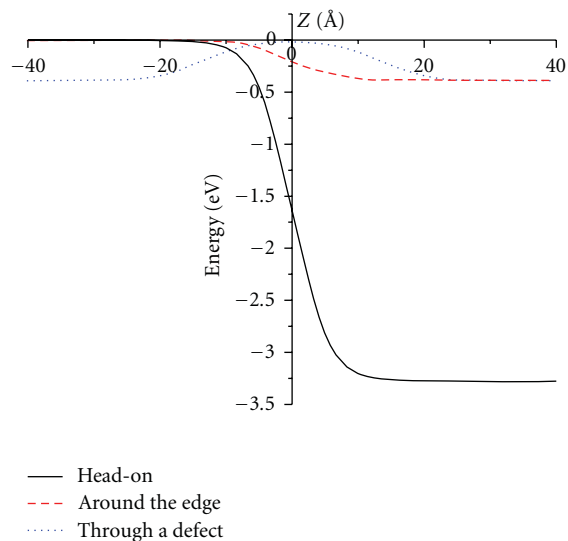


FIGURE 8: Potential energy for  $\text{TiO}_2$  with radius  $a = 10 \text{ \AA}$  encapsulated into a carbon nanotube with radius  $b = 13.5 \text{ \AA}$  and  $x = 26.4 \text{ \AA}$  for the three encapsulation mechanisms.

its location is directly above the defect pad. The least feasible mechanism to encapsulate the  $\text{TiO}_2$  molecule into the tube is entering around the edge of the tube open end because the  $\text{TiO}_2$  molecule must overcome the strong repulsive forces at the tube extremities and change its direction of motion as moving into the tube. Although these results might be as expected, this theoretical study is a first step in understanding the complex system for the encapsulation of drug molecules into a nanocapsule.

In comparison to other methods used to study nanoscience and nanotechnology, such as first principle calculations, molecular dynamics, or Monte Carlo simulations,

our applied mathematical modelling approach are not been widely used in this field. However, mathematical modelling can generate important insights into complex processes and reveal optimal parameters or situations that might be otherwise almost impossible through experimentation.

## Acknowledgment

This paper is funded by the Centre of Excellence in Mathematics, Thailand, and this financial support is gratefully acknowledged.

## References

- [1] S. Iijima and T. Ichihashi, "Single-shell carbon nanotubes of 1-nm diameter," *Nature*, vol. 363, no. 6430, pp. 603–605, 1993.
- [2] D. S. Bethune, C. H. Kiang, M. S. De Vries et al., "Cobalt-catalysed growth of carbon nanotubes with single-atomic-layer walls," *Nature*, vol. 363, no. 6430, pp. 605–607, 1993.
- [3] M. M. Calbi, M. W. Cole, S. M. Gatica, M. J. Bojan, and G. Stan, "Colloquium: condensed phases of gases inside nanotube bundles," *Reviews of Modern Physics*, vol. 73, no. 4, pp. 857–865, 2001.
- [4] A. N. Khlobystov, D. A. Britz, A. Ardavan, and G. A. D. Briggs, "Observation of ordered phases of fullerenes in carbon nanotubes," *Physical Review Letters*, vol. 92, no. 24, Article ID 245507, 3 pages, 2004.
- [5] B. W. Smith, M. Monthieux, and D. E. Luzzi, "Encapsulated  $\text{C}_{60}$  in carbon nanotubes," *Nature*, vol. 396, no. 6709, pp. 323–324, 1998.
- [6] S. Okada, S. Saito, and A. Oshiyama, "Energetics and electronic structures of encapsulated  $\text{C}_{60}$  in a carbon nanotube," *Physical Review Letters*, vol. 86, no. 17, pp. 3835–3838, 2001.
- [7] A. V. Emeline, A. V. Frolov, V. K. Ryabchuk, and N. Serpone, "Spectral dependencies of the quantum yield of photochemical processes on the surface of nano/micro-particulates of

wide-band-gap metal oxides. IV. Theoretical modeling of the activity and selectivity of semiconductor photocatalysts with inclusion of a subsurface electric field in the space charge region," *Journal of Physical Chemistry B*, vol. 107, no. 29, pp. 7109–7119, 2003.

- [8] N. Serpone, *The KirkOthmer Encyclopedia of Chemical Technology*, John Wiley & Sons, New York, NY, USA, 2000.
- [9] J. C. Ireland, P. Klostermann, E. W. Rice, and R. Clark, "Inactivation of escherichia coli by titanium dioxide photocatalytic reaction," *Applied and Environmental Microbiology*, vol. 59, pp. 1668–1670, 1993.
- [10] M. Cho, H. Chung, W. Choi, and J. Yoon, "Different inactivation behaviors of MS-2 phage and Escherichia coli in TiO<sub>2</sub> photocatalytic disinfection," *Applied and Environmental Microbiology*, vol. 71, no. 1, pp. 270–275, 2005.
- [11] B. J. Cox, N. Thamwattana, and J. M. Hill, "Mechanics of atoms and fullerenes in single-walled carbon nanotubes. II. Oscillatory behaviour," *Proceedings of the Royal Society A*, vol. 463, no. 2078, pp. 477–494, 2007.
- [12] B. J. Cox, T. A. Hilder, D. Baowan, N. Thamwattana, and J. M. Hill, "Continuum modelling of gigahertz nano-oscillators," *International Journal of Nanotechnology*, vol. 5, no. 2-3, pp. 195–217, 2008.
- [13] T. A. Hilder and J. M. Hill, "Oscillating carbon nanotubes along carbon nanotubes," *Physical Review B*, vol. 75, no. 12, Article ID 125415, 2007.
- [14] D. Baowan, N. Thamwattana, and J. M. Hill, "Suction energy and offset configuration for double-walled carbon nanotubes," *Communications in Nonlinear Science and Numerical Simulation*, vol. 13, no. 7, pp. 1431–1447, 2008.
- [15] D. Baowan and J. M. Hill, "Suction energy and oscillatory behavior for carbon nanocones," *Journal of Computational and Theoretical Nanoscience*, vol. 5, pp. 302–310, 2008.
- [16] D. Baowan, N. Thamwattana, and J. M. Hill, "Encapsulation of C<sub>60</sub> fullerenes into single-walled carbon nanotubes: fundamental mechanical principles and conventional applied mathematical modeling," *Physical Review B*, vol. 76, no. 15, Article ID 155411, 8 pages, 2007.
- [17] D. Baowan, W. Triampo, and D. Triampo, "Encapsulation of TiO<sub>2</sub> nanoparticles into single-walled carbon nanotubes," *New Journal of Physics*, vol. 11, Article ID 093011, 2009.
- [18] J. E. Lennard-Jones, "Cohesion," *Proceedings of the Physical Society*, vol. 43, no. 5, pp. 461–482, 1931.
- [19] A. Fahmi, C. Minot, B. Silvi, and M. Causa, "Encapsulation of TiO<sub>2</sub> nanoparticles into single walled carbon nanotubes," *Physical Review Letters*, vol. 47, pp. 11717–11724, 1993.
- [20] S. L. Mayo, B. D. Olafson, and W. A. Goddard III, "DREIDING: a generic force field for molecular simulations," *Journal of Physical Chemistry*, vol. 94, no. 26, pp. 8897–8909, 1990.
- [21] L. A. Girifalco, M. Hodak, and R. S. Lee, "Carbon nanotubes, buckyballs, ropes, and a universal graphitic potential," *Physical Review B*, vol. 62, no. 19, pp. 13104–13110, 2000.